Title
Biomaterials Design for Control of Cell Behavior by Femtosecond Laser Processing

Author
Jeon, Hojeong

Publication Date
2011

Peer reviewed|Thesis/dissertation

Biomaterials Design for Control of Cell Behavior by Femtosecond Laser Processing

By

Hojeong Jeon

A dissertation submitted in partial satisfaction of the
requirements for the degree of
Doctor of Philosophy
in
Engineering – Mechanical Engineering
in the
Graduate Division
of the
University of California, Berkeley

Committee in charge:

Professor Costas P. Grigoropoulos, Chair
Professor Kevin E. Healy
Professor Ralph Greif
Professor Samuel Mao

Spring 2011

Biomaterials Design for Control of Cell Behavior by Femtosecond Laser Processing

By

Hojeong Jeon

Abstract

Biomaterials Design for Control of Cell Behavior by Femtosecond Laser Processing

by

Hojeong Jeon

Doctor of Philosophy in Mechanical Engineering

University of California, Berkeley

Professor Costas P. Grigoropoulos, Chair

The last decade has seen exciting and unprecedented work at the interface between biology and materials science, particularly in the form of exquisite control of cell attachment, shape, traction, motility, and differentiation. Recent progress in developing techniques for microfabrication of biomaterials helps recapitulate many extracellular matrix (ECM) cues, making them progressively more useful for applications in biology and tissue engineering. This dissertation presents a study of femtosecond laser assisted micro- and nano-fabrication applicable for the biomaterials design aiming at achieving deliberate control of the cell behavior. Cell mechanics connected to cell alignment and migration, from speculation of cell response to the biomaterials surface to control of the response by topographic and chemical patterns, was studied.

Cell migration is an essential cellular process for a variety of physiological and pathological phenomena. Migration of leukocytes mediates phagocytic and immune responses. Migration of fibroblasts, vascular endothelial cells, and osteoblasts contributes to wound healing and tissue regeneration, and tumor cell migration is essential to metastasis. The cell migration process can be initiated by mechanical and chemical cues from the extracellular microenvironment. Factors affecting cell migration can be both soluble and insoluble macromolecules that comprise the ECM or mediate extracellular communication.

We apply femtosecond laser induced two-photon polymerization and multiphoton laser ablation lithography to fabricate precisely defined two-dimensional patterned surface in nanometer to micrometer length scale and three-dimensional filamentous materials to be used in studies addressing fundamental issues concerning control of cell adhesion and migration. We studied microscale topographical patterned surface for cell alignment and migration. Anisotropic micronscale ridge/groove patterned surfaces are powerful cues to control cell shape and to enhance or obstruct cell migration. However, they have limited ability to independently control the size and the distribution of the cell adhesive domains and the ligand density. Thus, we applied chemically and topographically patterned surfaces in the nanoscale to control cell adhesion and guide directional cell migration to overcome constraints of microscale patterns. During cell migration, contractile force is needed to move the cell body forward. We also studied the contractile force exerted by an individual locomoting cell using fiber scaffolds.

To Hyunjung, Emily, Jayden, and my parents

ACKNOWLEDGEMENTS

Throughout the five years of my graduate student days, there have been many people each of whom I am extremely grateful to. First of all, I would like to express my heartfelt gratitude to my research advisor, Professor Costas P. Grigoropoulos in the department of mechanical engineering at University of California, Berkeley. His academic advice and encouragement have helped me keep studying whenever my research was going well or not. I would like to give my warmhearted acknowledgement to his personal concern and encouragement for me and my family as well as his financial and educational supports. Professor Kevin E. Healy advised me as well after becoming a Ph.D. candidate. I could have experiences in the field of bioengineering through discussion with him and his group members. I would also like to extend my thanks to Professor David J. Hwang at State University of New York, Stony Brook for his guiding and teaching me from personal life to scientific study, and to Professor Hirofumi Hidai who started two-photon polymerization process in our group and helped me apply the technique to biomaterials, which is the starting of this dissertation. I cannot overestimate his efforts when he was working with me as a visiting scholar.

It has been my great pleasure to work together with former and current members of Laser Thermal Lab. I would like to thank Dr. Seunghwan Ko, Dr. Moosung Kim, Dr. Ming-tsang Lee, Dr. Matthew Rogers, Dr. Nipun Misra, Dr. Nico Hotz, Dr. Heng Pan, Dr. Sang-gil Ryu, Jungbin In, Travis Owens, Jan Duesing, Daeho Lee, Sanghoon Ahn, Kyunghoon Kim, Eunpa Kim, Jae Hyuck Yoo, Alex Sherry, and Hyojin Choi. I would also extend my gratitude to members of Professor Healy's group including Dr. Ray Schmidt, Dr. Jeremy E. Barton, and Dr. Rohini Gupta.

Finally, I am extremely grateful to my wife, Hyunjung Kim, for her great patient , encouragement, and love. She has been the most supportive friend of mine though she is also Ph.D. student. My harmonious family including two kids, Emily and Jayden, is my strength to finish my Ph.D. My parents also always give me unconditional support and encouragement and pray for my family. I would like to dedicate this dissertation to my family and God.

TABLE OF CONTENTS

LIST OF FIGURES

LIST OF TABLES

Chapter 1

Introduction

In vitro studies of cell biology have shown that cells can sense their extracellular environment that can regulate cellular functions, such as cell signaling [1], morphology [2, 3], migration [4], proliferation [5], and differentiation [6]. It is believed that physical aspects of cellular environment are sensed by cells and the physical signals are transduced into biochemical responses, which is called cellular mechanotransduction [1]. One proposed mechanism for the transduction is through mechanical forces transmitted via the direct link of the cytoskeleton to the nucleus [7] and in particular to nuclear matrix proteins such as NMP1 and 2 [8]. As such, the mechanotransduction effect involves the continuous physical linkage between cytoskeletal elements and the extracellular matrix (ECM)-integrin complex [9]. Recent progress in developing techniques for microfabrication of biomaterials helps recapitulate many ECM cues, making them progressively more useful for applications in biology and tissue engineering [10].

In particular, topographically and chemically patterned surfaces are known to be powerful tools for influencing those cellular functions. Parallel patterning techniques such as photolithography, microcontact printing, and imprint lithography have received much attention due to the rapid and relative ease of replicating patterns [11-13]. Unfortunately, such techniques require master patterns, which are most often generated by expensive direct write laser patterning mask writers designed for the microelectronics industry [14]. Less elaborate and more readily accessible direct write approaches such as Electron Beam Lithography (EBL), Atomic Force Microscopy based Dip Pen Nanolithography (DPN), or Near-Field Scanning Optical Microscopy (NSOM) techniques allow the generation of arbitrary nanoscale patterns, but process times are limited by the processing environment and the dose time necessary to generate each feature [14-16]. While such techniques are sufficient for small experimental programs, the costs involved in generating the hundreds of large area samples with differing geometries needed for ambitious biological and sensor programs is often prohibitive. For this class of applications there is a demonstrated need for a rapid direct write topographical and chemical patterning technology with low marginal cost. One potential

method to achieve this speed is to extend conventional laser microfabrication technology, by exploiting multiphoton ablation, to reduce feature sizes below the optical diffraction limit.

The laser ablation patterning is useful for generating two-dimensional (2D) patterned surfaces. However, it is difficult to fabricate patterns of high aspect ratio at micrometer order lateral dimensions or three-dimensional (3D) structures by laser ablation processing. Traditional photolithography and soft-lithography techniques require multiple process steps with a number of masks, in order to fabricate variable height patterns on the same wafer. Stereo-lithography [17] and fused-deposition modeling (FDM) [18] techniques can fabricate different height patterns and 3D scaffolds easily, but these methods require multiple steps of laser exposure and liquid deposition, respectively. Fabrication of three-dimensional structures at high spatial resolution up to ~100 nm has been demonstrated via two-photon polymerization induced by tightly focusing and/or scanning an ultrafast laser beam [19-21]. However, use of high numerical aperture (NA) objective lens not only limits the pattern height due to tight working distance but also allows only a very limited patterned area due to small field of view. As a result, high aspect ratio three-dimensional structures are fabricated by elaborately piling up multiple layers through complex relative position control of the laser focus.

This thesis deals with systematic studies on rapid fabrication of microstructures including 2D micropatterning and 3D fiber scaffolds by two-photon polymerization (2PP) process and sub-diffraction nanoscale topographic and chemical patterning by two-photon laser ablation lithography. The fabrication techniques offer a new opportunity for biomaterials design and cell mechanobiology. In particular, cell mechanics regarding to cell alignment and migration, from speculation of cell response to the biomaterials surface to control of the response by topographic and chemical patterns, is discussed in the following chapters.

Chapter 2: This chapter provides an introduction to biomechanics of cell migration with a basic mechanism and briefly reviews how to regulate cell migration and bioengineered tools for control of cells by applying the chemical and mechanical factors.

Chapter 3: This chapter reviews laser-induced microfabrication of transparent materials. We describe the nonlinear interactions that govern how materials respond to high intensity laser pulses, such as multiphoton absorption, nonlinear index of refraction and self-focusing phenomena that are important for the laser-induced fabrication of biomaterials described in Chapter 4-7.

Chapter 4: We demonstrate a method for fabricating high aspect ratio patterns of varying height by using two-photon polymerization process to study contact guidance of cells. In this chapter, morphological cell response to microscale topographically patterned surface is described. Cell morphology represents an evidence of sensing of external stimuli and is beginning of a range of cellular events, such as proliferation, differentiation, cytoskeletal organization, migration, and cell fate determination.

Chapter 5: This chapter demonstrates cell morphology and motility on micronscale anisotropic cross patterns and parallel line patterns having different aspect ratios (1:2, 1:4,

and 1:∞), grid size (12-, 16-, and 24-μm distance neighboring longer side ridges), and height of ridges (3- and 10-μm). The movement characteristics were analyzed quantitatively with respect to cell migration speed, migration angle, persistence time (P) and motility coefficient (μ).

Chapter 6: The early chapters discuss the cell response to microscale topographical patterns. Those micropatterns are effective on cell alignment and enhancing directional migration on the surface of biomaterials. In this chapter, nanoscale patterns of topographically and chemically modified surface are fabricated by multiphoton laser ablation lithography to achieve feature sizes below the optical diffraction limit. Ultrafast laser ablation of polymer thin film and quartz glass is described. We demonstrate cell repellent nanopatterned surface and guided cell migration on the topographical and chemical patterns.

Chapter 7: Contractile forces must be generated by a locomoting cell. The force is needed to move the cell body forward. The cell contractility is examined microscopically in order to measure contractile forces generated by individual cells on self-standing fiber scaffolds that were fabricated via femtosecond laser-induced two-photon polymerization.

Chapter 8: This thesis shows advantages of laser based fabrication techniques for the biomaterials design and addresses mechanical cell responses to the biomaterial interface. In this chapter, the key results discussed in this thesis are reviewed and ideas for further experiments, especially control of stem cell fate, are suggested.

Chapter 2

Biomechanics of cell migration

The objective of the research described in this thesis is to design biomaterials to control cell behavior, in particular cell adhesion and migration. In this chapter, we review some of the basic biomechanics of cell migration as well as previous studies to regulate cell migration. In addition, we briefly review some examples of the patterning techniques for control of cell behaviors.

2.1. Introduction to cell migration

Cell migration is an essential cellular process for a variety of physiological and pathological phenomena. Migration of leukocytes mediates phagocytic and immune responses. Migration of fibroblasts, vascular endothelial cells, and osteoblasts contributes to wound healing and tissue regeneration, and tumor cell migration is essential to metastasis [22]. In some cases, migration can lead to implant failure of percutaneous devices and dental implants due to epithelial down-growth on the implant surface [23]. As migration and other cell responses, including adhesion and proliferation are dependent on cell-materials interactions, numerous reports have examined the influence of both surface chemistry and topography on cell behavior [24, 25].

The migration of cells has been described as a multistep process. For cells to move forward, actin polymerization at the leading edge pushes the plasma membrane forward and forms new regions of actin cortex. New points of anchorage are formed between the actin filaments and the surface where the cell is migrating. Contraction at the rear of the cell then draws the body of the cell forward. Old anchorage points are released at the back as the cell crawls forward. This multistep process is repeated for cell migration [26].

2.2. Regulation of cell migration

The cell migration process can be initiated by mechanical and chemical cues from the extracellular microenvironment. The factors to affect cell migration can be both soluble and insoluble macromolecules that comprise the extracellular matrix (ECM) or mediate extracellular communication. For example, bacterial gene expression is regulated by small molecules produced in their surrounding medium, and the bacteria can use the attractant chemicals to associate and form a quorum [27]. This mechanism is called chemotaxis. Normal tissue cells must adhere to a solid surface and form anchorages. Therefore, the cells are directly affected by the surface of the ECM as well as the fluidic medium. The tissue cells can feel and respond to the stiffness of their substrate of ECM [28]. Cell migration can be affected by a gradient of the density of ECM proteins (haptotaxis), the stiffness gradient (durotaxis), directional mechanical forces (mechanotaxis), and topographical patterns (contact guidance) [29].

2.2.1. The effect of chemical density

Chemotaxis is a directed cell migration controlled by a concentration gradient of a chemoattractant in solution [29, 30], while a uniform concentration of chemoattractant can only regulate cell motility without a favorable direction, hence comprising the so-called chemokinesis mechanism. Many types of cells are modulated by chemotaxis: bacterials quorum sensing, embryogenesis, inflammatory responses, and wound healing. In the presence of a spatial gradient of a chemoattractant, intracellular sensory systems impose a bias on cells random walk behavior in a manner that yields net migration in a preferred direction, i.e. higher concentration of the chemoattractant. For example, microfluidic channels have been used to generate the concentration gradient of a chemoattractant because of advantages of the low Reynolds number flow in the microchannels [31]. Jeon *et al.* generated a linear gradient of L-aspartate using the microfluidic channels and analyzed data of chemotactic motility of individual *E. coli* strain RP437 in response to various concentration gradient of L-aspartate. They showed that the RP437 cells make the most vigorous response at 0.22 mM mm^{-1} gradient [30]. For another example, human neutrophils exhibit strong directional migration toward increasing concentration of interleukin-8 when they are placed within linear concentration gradient of the chemoattractant in a microfluidic channel [32].

Figure 2.1. Schematic diagram of cell polarization by chemotaxis: gradient concentration of chemoattractant in solution.

Haptotaxis is the other example of directional migration controlled by surface density and distribution of ECM proteins [29]. When cells adhere to substrates, primary sites are focal adhesions (FAs) that link the ECM to cytoskeletons via membrane-bound receptors [33]. The FAs are known to be capable of providing strong cell adhesion to the ECM and are regions of signal transduction regulating cell growth [34]. The adhesion forces have a significant influence on motility, as Dimilla *et al.* reported that initial cell-substratum attachment strength is a central variable governing cell migration speed and maximal speed can be obtained by cells moving on surfaces offering intermediate attachment strength [35]. The gradient adhesion force due to the gradient of surface density of ECM proteins can regulate directional cell migration and specifically from the area of low-density to high-density of the ECM. Carter *et al.* showed the highly directional cell migration forward increasing metal deposition on a surface of cellulose acetate [36].

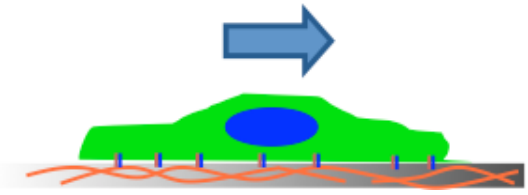

Figure 2.2. Schematic diagram of cell polarization by haptotxis: gradient of ECM.

2.2.2. The effect of surface rigidity

Normal eukaryote cells are typically viable when they adhere to a solid surface and form anchorages. The solid tissues exhibit a range of stiffness from soft to rigid: ~1 kPa for brain, ~10 kPa for muscle, and ~100 kPa for collagenous bone [37]. Cells can sense the elasticity of their substrate as well as the surface density of ECM proteins and transduce the information into nucleus via FAs and intracellular cytoskeletons [29]. The FAs on soft substrates are diffuse and dynamic, while FAs on rigid substrates are more stable because cells exert less tension on softer surface and consequentially crawl faster [28]. As a result of sensing substrate stiffness, cells tend to migrate to a stiffer substrate owing to the stronger traction force between the cells and the substrate, which is called durotaxis [38]. For example, Lo *et al.* showed that NIH3T3 fibroblasts on flexible polyacrylamide sheets coated with type I collagen can be guided by manipulating the substrate stiffness [38].

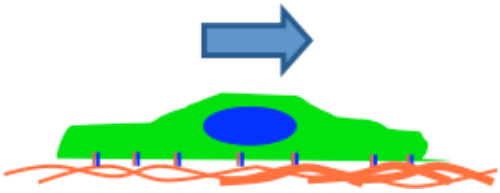

Figure 2.3. Schematic diagram of cell polarization by durotaxis: gradient of solid stiffness.

2.2.3. The effect of surface topography

Cells can also sense surface topography of a substrate with dimensions from a few nanometers to hundreds of micrometers [2, 6]. It is not precisely known how cells sense and react to topography, although it is believed that filopodia are sensing organelles [25]. Ridge/groove patterns have been used to examine cell sensing of topography, and microgrooved surfaces with various groove and ridge dimensions have been studied [2-4, 39-41]. Previous studies have suggested that the topographical surfaces have a profound effect on controlling cells, such as orientation and movement (contact guidance). It is well known that cell alignment and motility become more effective when cells reside in deeper grooves and narrower ridges [2, 3]. In the later chapters (chapters 4-6), the contact guidance will be dealt with in more detail.

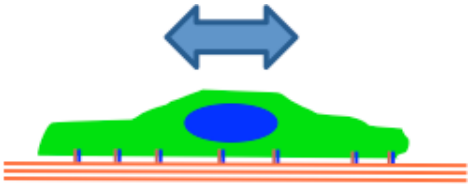

Figure 2.4. Schematic diagram of guided cell migration by surface topographic guidance.

2.2.4. The effect of mechanical forces

In nature tissues, mechanical forces, such as mechanical strain and shear stress, are important factors for regulating cell behavior. Mechanical strain in a vascular wall is anisotropic and mainly in its circumferential direction, and *in-vitro* experiment showed that cell alignment and global gene expression changed by the cyclic uniaxial strain [42]. In a cardiovascular system, shear stress induced by blood flow acts on the surface of endothelial cells and regulates cell migration. It is believed that the shear stress can enhance cell migration by extending the leading edge of cells and releasing adhesions at the rear [29].

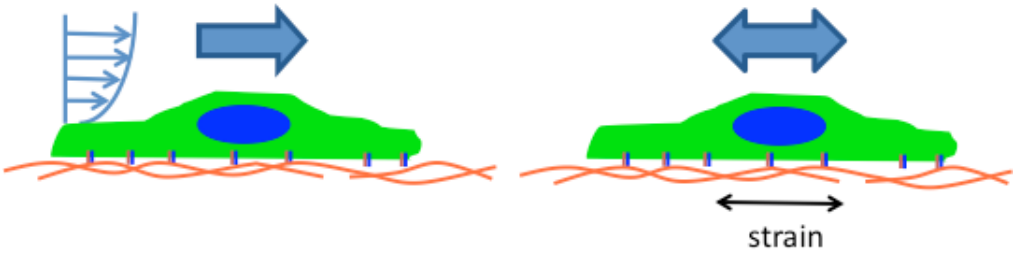

Figure 2.5. Schematic diagram of guided cell migration by fluid shear stress and uniaxial mechanical strain.

2.3. Bioengineered tools for control of cells

Elucidating adhesion and signaling in cellular interactions has driven scientists and engineers to develop techniques for the patterning of surfaces to control the distribution of biomolecules and topographic cues at the length scale of both cells and ECM proteins. Mirofabrication or micropatterning techniques enable researchers to design biochemical and biomechanical substrates, with micrometer length scale, which offers the potential to control cell-surface, cell-cell, and cell-medium interactions [43]. Most microfabrication techniques are based on photolithography (patterning of photo resister by illumination of UV light), soft lithography (replicating from a microfabricated master mold), and microfluidic patterning (delivering fluids to selected areas) [43]. The microscale patterned surfaces are powerful for controlling cell behavior, but they are limited in their ability to independently control the size and the distribution of the cell adhesive domains and the ligand density [44]. Therefore, there is increasing demand for developing new techniques for nanometer length scale patterning. Four nanopatterning techniques are currently in heavy use: dip-pen lithography, electron beam lithography, micro- and nanocontact printing, and electrospinning [45].

2.3.1. Dip-pen lithography

Dip-pen lithography (DPN) or scanning probe lithography techniques employ basically high resolution scanning probe imaging techniques in order to modify surface topography or chemistry [46]. A molecular ink can be directly transferred onto a substrate by an atomic force microscope (AFM) tip to generate chemical patterning in nanometer length scale. These techniques offer high-resolution patterning depending on the size of the AFM tip and can be performed under ambient conditions. However, it is still challenging to generate a large size pattern arrays using these techniques .

2.3.2. Electron beam lithography

Electron beam lithography (EBL) is the other type of direct write patterning. Development of scanning electron microscopes has enabled high-resolution direct patterning using the electron beam. The EBL technique was first developed to fabricate photomasks for photolithography and electronic features. This technique allows high-resolution micro- to nanoscale patterning of chemistry and topography with relatively high throughput compared to other direct-writing techniques. But the substrate materials should be conductive, stable in ultra-high vacuum. The processing cost is also high. Thus, the substrates generated by EBL techniques are normally used as master molds for soft lithography [6].

2.3.3. Micro- and nano-contact printing

The micro- and nano-contact printing is a convenient and widely used soft lithography technique. In this process, a molecular ink is transferred onto a substrate using micro- and nanostructured elastomer stamps [47]. This technique is rapid and relatively easy for pattern replication, but requires master patterns that are fabricated by other fabrication techniques, such as photolithography, DPN, EBL, Focused Ion beam lithography (FBL), and laser lithography. In nanometer scale, stamping methods have a limitation due to deformation of the molds, such as elastomer polydimethylsiloxane (PDMS).

2.3.4. Electrospinning

The electrospinning technique can generate nanoscale fibrous structures mimicing extracellular matrices of biological cells. High surface area to volume ratio of the fibrous matrices composed by electrospun nanofibers creates a similar environment to native ECM. The scaffolds made with nanofibers are beneficial with respect to the diffusion and delivery of biochemical molecules due to the mesh-like structures consisting of nano- or micro- size pores. Thus, this technique has received considerable attention. Recently, researchers have tried to generate aligned nanofibers to address cell response to directed organization. Although electrospinning permits fabrication of aligned fibers, the low porosity limits cell infiltration and does not create real 3D tissues.

Four widely used fabrication techniques for biological materials have been reviewed. Certainly, there are also many other tools for biological experiments, and researchers continually strive to develop new methods. In this thesis, the aforementioned techniques are not used nor evaluated. The focus is on laser-induced fabrication techniques that are also useful for biomaterials design. In particular, femtosecond laser processing will be described in the next chapters.

Chapter 3

Microfabrication of transparent materials by ultrafast laser

Cell migration described in the previous chapter can be controlled by patterned surfaces that can offer micro- to nanoscale topography and chemical contrast. Before delving into our experimental results, in this chapter, we discuss how a femtosecond laser can be used to structure and modify biomaterials, and particularly transparent materials. We therefore recall the basic principles that govern the interaction of femtosecond laser pulses with transparent materials. When highly intense ultra-short laser pulses are focused into transparent dielectrics, only the localized region within the focal volume absorbs laser energy via nonlinear absorption. The femtosecond laser microfabrication has unique advantages due to the nonlinear absorption and involved nonlinear effects.

3.1. Ultrafast-laser interactions with transparent materials

A femtosecond laser pulse has extremely high peak power and intensity due to ultra-short pulse width. When highly intense ultra-short laser pulses are focused into transparent materials, only the localized region within the focal volume absorbs the laser energy by nonlinear absorption processes such as multiphoton initiated avalanche ionization (Figure 3.1(A)) [48]. In contrast to material modification by nanosecond or longer laser pulses, there is no heat exchange during femtosecond laser pulse irradiation, which results in minimizing thermal stress and collateral damage. The nonlinear optical characteristics and minimized heat and shock effects are particularly beneficial to fabricating stable high-resolution 2D and 3D features.

3.1.1. Multiphoton absorption

For a case of single photon absorption, the laser can deposit its energy into a material by creating an electron-hole plasma. However, for wide-band-gap materials, such as dielectrics, the cross section of the linear absorption is relatively small, while nonlinear processes including multiphoton ionization, tunnel ionization, and avalanche ionization become dominant by creating free carriers in the materials under irradiation of intense femtosecond laser pulses [48].

For the wide-band-gap materials, absorbed energy by single photon absorption of the femtosecond laser pulses with wavelength near the visible is not sufficient to excite an electron from the valence band to the conduction band. Simultaneous absorption of

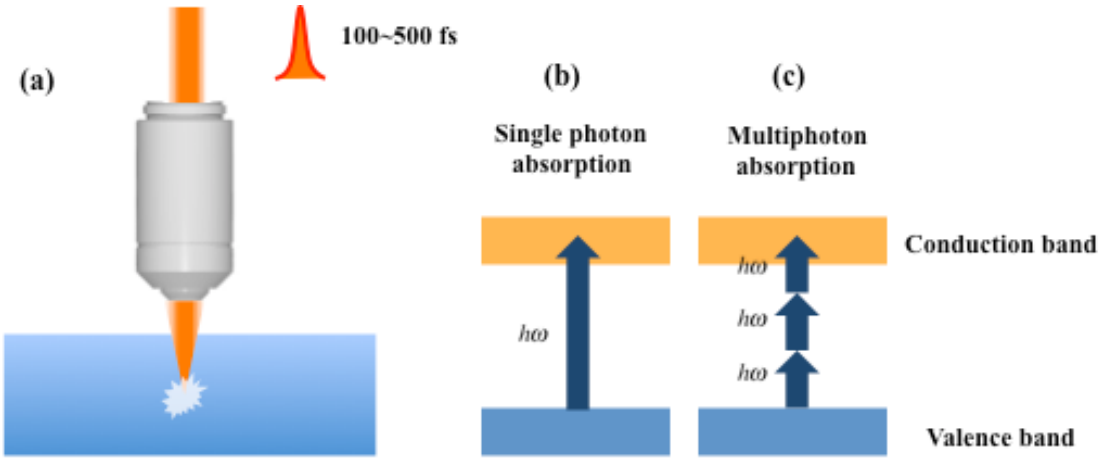

Figure 3.1. Femtosecond laser processing with transparent material. (A) Schematic of the laser irradiation into the dielectric material. (B) Diagram of electron excitation by the single photon absorption. (C) Diagram of electron excitation by the multiphoton absorption.

multiple photons must be involved to excite valence band electrons, which depends on laser intensity. Thus, the laser absorption occurs only within a focal volume, where the intensity exceeds the multiphoton absorption thresholds. The absorbed intensity (I_m) by the multiphoton absorption can be expressed as follows:

$$I_m \propto \sigma^{(n)} I^n \tag{3.1}$$

where $\sigma^{(n)}$ is the cross section of n-photon absorption, the probability of simultaneous absorption of n photons, and I is the laser intensity. For example, two-photon microscopy requires absorption of two photons of half the photon energy of the single photon normally required (Figure 3.1(B) and (C)).

$$2(\hbar\omega) > E_{bg} \tag{3.2}$$

where E_{bg} is the band-gap energy and $\hbar\omega$ is the single photon energy.

The tunneling ionization comes into play during femtosecond laser interaction with dielectrics when the laser pulse width is extremely short (e.g. < 10 fs). Under this condition, the laser pulse can produce a strong periodic band-bending, resulting in tunneling of valence electrons directly to the conduction band in a time shorter than the laser pulse period. The crossover between multiphoton and tunneling ionization can be determined by Keldysh parameter as follows [49]:

$$\gamma_{Ke} = \frac{\omega(2m^* E_{bg})^{1/2}}{eE} \tag{3.3}$$

where m^* is the effective mass, e is the charge of an electron, E is the intensity of the laser pulse, and ω is the frequency of the laser pulse. When the Keldysh parameter is larger than ~1.5 (γ_{Ke}>1.5), the photoionization is a multiphoton process, when it is smaller than ~1.5 (γ_{Ke}<1.5), the photoionization is a tunneling process. In the intermediate regime (γ_{Ke}~1.5), both of the multiphoton and tunneling processes coexist.

The avalanche ionization involves free-carrier absorption followed by impact ionization. This process requires seed electrons to be already present in the conduction band of the material, which can be provided by photo-ionization, thermally excited carriers, or easily ionized impurity. Electrons in the high energy state can linearly absorb more photons sequentially, ionizing electrons from the valence band. Once the photon energy by the sequential absorption of *n* photons exceeds the band gap energy ($n(\hbar\omega) > E_{bg}$), they impact more valence-band electrons by collisional ionization. As long as the laser field is present and intense enough, the conduction-band population grows by the avalanche process. The electron density, N, in the conduction band can be described by the following rate equation [50].

$$\frac{dN}{dt} = \eta N = \alpha I N \tag{3.4}$$

where η is the avalanche ionization rate, α is the avalanche ionization coefficient, and the avalanche rate depends on the laser intensity ($\eta = \alpha I$).

3.1.2. Nonlinear propagation

The system of Maxwell's equations constitute the basis for the theory of electromagnetic fields and waves as well as their interactions with materials.

$$\nabla \times \vec{E} = -\mu \frac{\partial \vec{H}}{\partial t}, \tag{3.5}$$

$$\nabla \times \vec{H} = J + \frac{\partial \vec{D}}{\partial t}, \tag{3.6}$$

$$\nabla \cdot \vec{D} = \rho, \tag{3.7}$$

$$\nabla \cdot \vec{B} = 0, \tag{3.8}$$

and

$$\vec{D} = \varepsilon_0 \vec{E} + \vec{P}, \tag{3.9}$$

$$\vec{H} = \frac{1}{\mu_0} \vec{B} - \vec{M}, \tag{3.10}$$

where ε_0 and μ_0 are the electric permittivity and magnetic permeability, respectively, in vacuum. Recalling vector identity and reducing equations (3.5~10), we can get a wave equation by

$$\nabla \times \nabla \times \vec{E} + \frac{1}{c^2}\frac{\partial^2 \vec{E}}{\partial t^2} = -\frac{1}{\varepsilon_0 c^2}\frac{\partial^2 \vec{P}}{\partial t^2}. \tag{3.11}$$

In the linear regime when the electric field strength is small, the polarization is linearly related to the electric field by

$$\vec{P}(t) = \chi^{(1)}\varepsilon_0 \vec{E}(t), \tag{3.12}$$

where ε is electric permittivity of the material, and $\chi^{(1)}$ is the electric susceptibility. Using equation 3.12, the equation 3.11 can be simplified,

$$\nabla \times \nabla \times \vec{E} + \frac{n_0^2}{c^2}\frac{\partial^2 \vec{E}}{\partial t^2} = 0, \tag{3.13}$$

where n_0 is the index of refraction, defined as

$$n_0 = \sqrt{1 + \chi^{(1)}}. \tag{3.14}$$

However, at high field strength, the relations between $\vec{P}$ and $\vec{E}$ described above are no longer valid. The nonlinear dependence of the polarization on the applied electric field can be described by

$$\vec{P} = \varepsilon_0\left[\chi^{(1)}\vec{E} + \chi^{(2)}\vec{E}\vec{E} + \chi^{(3)}\vec{E}\vec{E}\vec{E} + \cdots\right] \tag{3.15}$$

3.1.2.1. Nonlinear index of refraction

When the high intensity laser pulses propagate through a material, the linear approximation of the polarization and the electric field is not valid, thus, resulting index of refraction (real part) can be derived as [51]

$$n = \sqrt{1 + \chi^{(1)} + \frac{3}{4}\chi^{(3)}E^2}, \tag{3.16}$$

where $\chi^{(1)}$ and $\chi^{(3)}$ are the linear and nonlinear susceptibility, respectively. This equation can be described as more convenient form,

$$n = n_0 + n_2 I \tag{3.17}$$

where I is the laser intensity defined as $I = \varepsilon_0 c n_0 E^2 / 2$, and n_2 is the nonlinear part of the refractive index defined as $n_2 = 3\chi^{(3)} / (4\varepsilon_0 c n_0)^2$. This nonlinear refractive index gives rise to nonlinear effects, such as self-focusing, when an intense femtosecond laser propagates through transparent materials.

3.1.2.2. Self-focusing

For the interaction between intense femtosecond laser pulses and dielectric materials, the index of refraction is dependent on the laser intensity as described in the previous section. Thus, the spatial variation of laser intensity, especially the Gaussian profile, of the femtosecond laser can create spatial refractive index variation, larger toward the center line of propagation (Figure 3.2(A)). The variation in the index of refraction acts as a positive lens and focuses the laser beam (Figure 3.2(B)). Catastrophic collapse of the laser beam to a singularity is predicted when the peak intensity of the femtosecond laser pulse exceeds a critical power for self-focusing, $P_{cr} = 3.77\lambda^2/(8\pi n_0 n_2)$, where λ is the laser wavelength, and is typically on the other of a few MW. In real materials, other mechanisms such as defocusing due to nonlinear ionization halt the beam collapse by balancing with self-focusing.

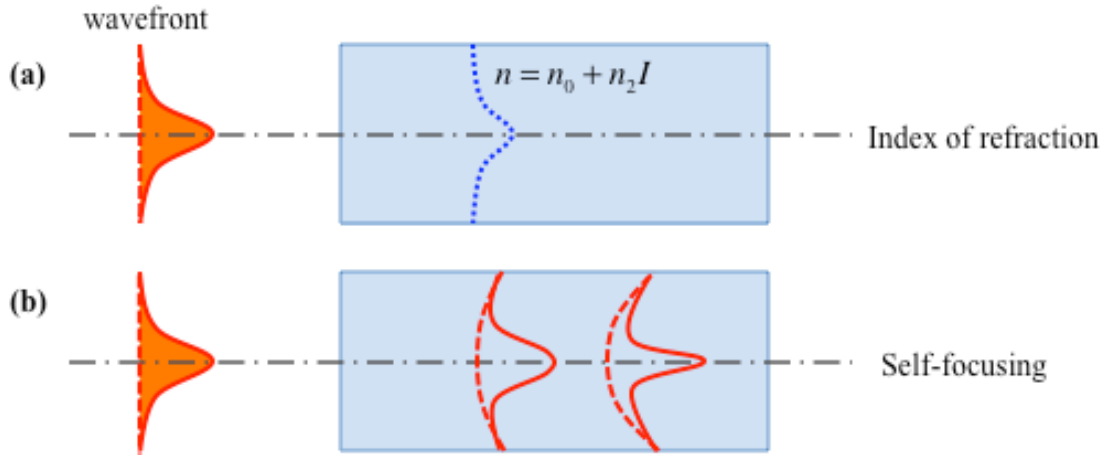

Figure 3.2. Schematic showing the spatial variation of (A) the index of refraction (dotted line), the beam profile (solid line) and phase fronts (dashed line) for (B) self-focusing.

3.1.3. Optical breakdown in dielectric materials

The femtosecond laser-induced damage in dielectric materials is known to be a nonlinear process. The damage in pure wide-band-gap materials is associated with rapid buildup of conduction electrons as described in the previous section 3.1.1. The mechanism of the optical breakdown can be explained by understanding the relative roles of various ionization and relaxation channels, particularly near the damage threshold. Once a dense electron-hole plasma has been generated in a bulk of dielectric materials by femtosecond laser irradiation, several mechanisms can be anticipated: melting or vaporization of the solid, following strong phonon emission as well as generation and accumulation of intrinsic defects.

The majority of many experimental and theoretical studies for determining the damage mechanisms has focused on damage thresholds depending on laser-pulse duration. It is well understood that thermal diffusion is dominant for pulse durations of 10 ps or longer laser pulses, and the material damage depends on laser-pulse duration according to a $\sqrt{t_{pulse}}$ scaling. However, for femtosecond lasers, the pulse duration is

much shorter than the characteristic time of thermal diffusion, and the damage threshold deviates from the square-root scaling [50, 52].

3.2. Two-photon polymerization

Due to the nonlinear process of the femtosecond laser interactions with transparent materials, much attention has been paid to microfabrication of transparent materials by the femtosecond laser pulses. Direct laser writing by two-photon polymerization (2PP) is an example of the laser-induced fabrication application, and has become known as a powerful tool for rapid and flexible fabrication of three-dimensional (3D) structures. Compared with conventional stereo lithography, the 2PP process can be confined to cure the photocurable resins only near the laser focal volume [53], hence enabling fabrication of arbitrary 3D structures. Nearly simultaneous absorption of two photons within the focal volume induces chemical reactions between photoinitiator molecules and monomers (Figure 3.3).

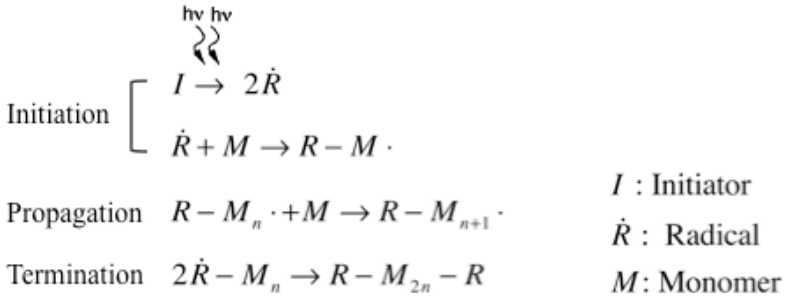

Figure 3.3. Photochemical reaction of two-photon polymerization [54].

A logarithmic dependence of voxel size on exposure time results from the exponential decay of the monomer concentration during, generating spatial resolution approaching 100 nm [55]. Two-photon polymerization techniques typically use scanning of the laser beam to create structures by continuously "stitching" the tiny voxels cured within the focal zone. Due to the unique advantages, 2PP microfabrication has recently been used to fabricate biomedical devices, such as microneedles, microfluidic devices, cell culture scaffolds [56]. The 2PP technique was used for the fabrication of topographical patterns and fibrous scaffolds in this thesis that will be discussed in chapter 4,5, and 7.

3.3. Direct write surface patterning

In conventional photolithographic procedures, photoresists are typically exposed to UV light through a photomask that defines regions to be removed or remained using a

chemical developing agent. The spatial resolution obtained is frequently limited by the chemical development step, the quality of the photomask employed, and by diffraction of light from the mask. However, multiphoton lithography provides high-resolution material processing requiring neither photomasks nor chemical developers [57, 58]. Intense femtosecond laser pulses can induce damage in transparent dielectrics by nonlinear absorption processes such as multiphoton initiated avalanche ionization [48]. In contrast to material modification by nanosecond or longer laser pulses, there is limited heat exchange during femtosecond laser pulse irradiation, which results in minimizing thermal stress and collateral damage. Therefore, the femtosecond laser induced ablation process is stable and reproducible [52, 59]. In addition, due to the nonlinear optical characteristics and Gaussian beam profile of the femtosecond laser, structures smaller than the processing beam spot size can be fabricated by precisely adjusting the pulse energy close to the ablation threshold [60, 61]. Since the laser interaction with dielectric materials is strongly nonlinear, a femtosecond laser focused via far-field optics can achieve ablative features with subwavelength resolution on inorganic (i.e. quartz) and polymer substrates [57, 60, 62]. This fabrication technique was used for nanoscale topographical and chemical patterned surfaces that will be discussed in chapter 6.

3.4. 3D fluidic microchannels

Nonlinear absorption phenomena can be adapted to fabricate glass based three-dimensional fluidic microchannels. With high-pulse-energy femtosecond laser beam, fabrication of straight and bent channels in glass by drilling process was reported by Hwang *et al.* [63]. The drilling was initiated from the rear surface of the glass to preserve a consistent absorption profile and followed by scanning of the femtosecond laser beam toward the front surface. For the low-repetition-rate (< 100 kHz), high-pulse-energy femtosecond laser pulses, a single pulse is responsible for material modification (i.e. damage) because both thermal and mechanical relaxation is concluded between pulses. However, for high-repetition-rate (> 1 MHz), low-pulse-energy femtosecond laser pulses, the pulse-to-pulse cumulative effect plays an important role for the material modification in terms of thermal diffusion. The heat accumulation effect of the high-repetition-rate femtosecond laser pulses can be used to modify material property (i.e. mechanical and optical) within dielectric materials, such as optical waveguide and microfluidic channels [64].

Chapter 4

Cell alignment on microscale topographical patterned surfaces

In this chapter, we demonstrate a method for fabricating high aspect ratio (~10) patterns of varying height by using two-photon polymerization process in order to study contact guidance of cells. Ridge patterns of various heights and widths were fabricated through single laser scanning steps by low numerical aperture optics, hence at much higher processing throughput. Fibroblast cells were seeded on parallel line patterns of different height and orthogonal mesh patterns. Cells experienced different strength of contact guidance depending on the ridge height. Our results demonstrate that a height threshold of nearly 1 μm influences cell alignment on both parallel line and orthogonal mesh patterns. This fabrication technique may find wide application in the design of single cell traps for controlling cell behavior in microdevices and investigating signal transduction as influenced by surface topology [65].

4.1. Introduction

Patterned surfaces are often utilized for cell studies such as observing individual cell behavior on cell-trapping well arrays [66-70] or various other controlled surface topographies [2-4, 25, 39, 71-73]. Such a pattern can either effectively trap a single cell [66, 69, 70] or control detailed cell shape [67, 68]. Most of the related reports use wells with limited depth settings on a single substrate, even though wells of varying depth can further extend the substrate function in conjunction with simultaneous cell sorting. In addition, the study of cell behavior on topographically patterned surfaces is also very important for elucidating the detailed cell-surface interaction, especially in the context of of implanted materials. Many groups have been studying the influence of patterned

surfaces on cell morphology and motility [2-4, 25, 39, 71-74], since the exact mechanisms and different response of cells to various substrates have yet to be elucidated [25, 75]. Despite abundant studies performed in this field, comprehensive reports based on patterns of various heights on a single sample configuration are rare [4], mainly due to lack of appropriate fabrication techniques. These micro-pattern fabrication techniques have been based on micromachining [4, 72], laser ablation [71, 73], photolithography [3, 39, 67, 68, 70], and electron beam lithography. It is difficult to fabricate patterns of high aspect ratio at micrometer order lateral dimensions by micromachining and laser ablation. Traditional photolithography and soft-lithography techniques require multiple process steps with a number of masks, in order to fabricate variable height patterns on the same wafer. Stereo-lithography [17] and fused-deposition modeling (FDM) [18] techniques can fabricate different height patterns and 3D scaffolds easily, but these methods require multiple steps of laser exposure and liquid deposition, respectively. Fabrication of three-dimensional structures at high spatial resolution up to ~100 nm has been demonstrated via two-photon polymerization induced by tightly focusing and/or scanning an ultrafast laser beam [19-21]. However, use of high numerical aperture (NA) objective lens not only limits the pattern height due to tight working distance but also allows only a very limited patterned area due to small field of view. As a result, high aspect ratio three-dimensional structures are fabricated by elaborately piling up multiple layers through complex relative position control of the laser focus. Recently, we have performed a systematic study on rapid fabrication of high aspect ratio microstructures by focusing an ultrafast laser beam through low NA objective lenses [76, 77].

In this study, we demonstrated rapid fabrication of high aspect ratio patterns by two-photon polymerization (2PP). In a striking difference from previous 2PP techniques, patterns of various heights and widths were fabricated through single scanning steps, thereby at much higher processing throughput and simpler laser processing parameters by utilizing unique nonlinear self-focusing characteristics of ultrafast laser radiation [76, 78-82]. Use of low NA objective lenses facilitated processing of much larger areas than in previous 2PP studies [19-21]. Patterns of multiple heights were easily fabricated onto single sample configuration by simply changing laser parameters such as laser beam power and scanning speed. In order to demonstrate control of the cell behavior via the fabricated patterns, two types of ridge and groove structures were fabricated; one consisting of aligned parallel ridges of different heights, and the other comprising orthogonally combined mesh patterns of different heights. Mouse fibroblast cells (NIH-3T3) were used, as in similar studies [4, 40, 83-85].

4.2. Arbitrary ridge/groove pattern fabrication by two-photon polymerization

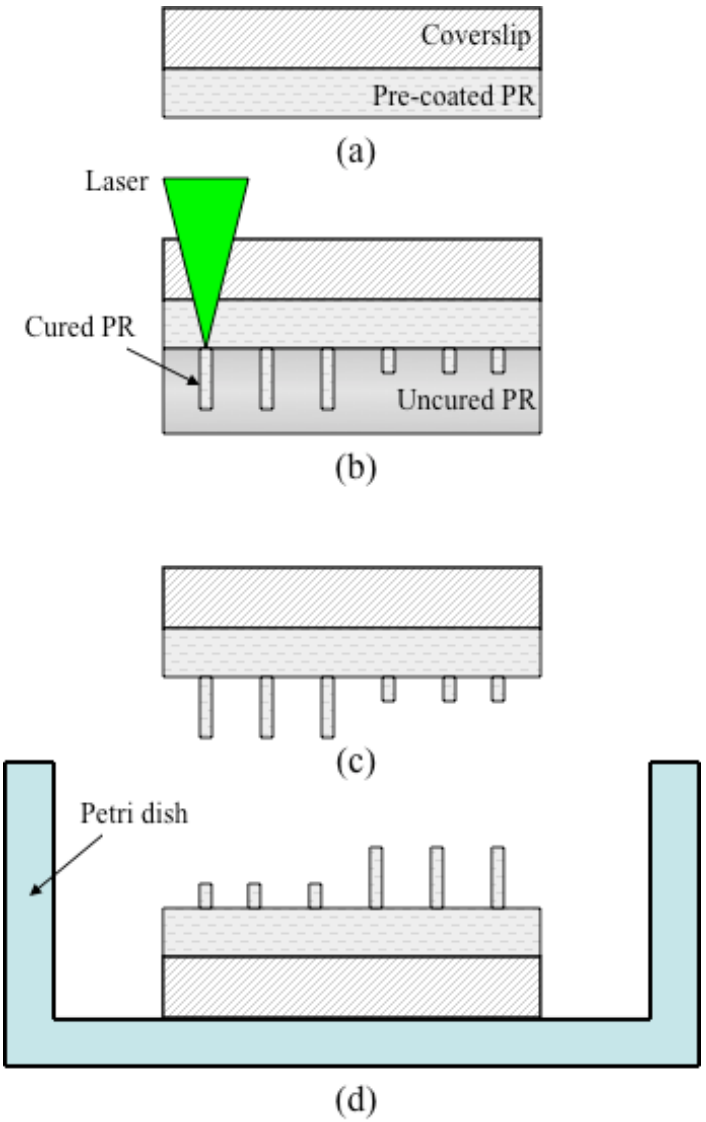

Figure 4.1. Illustration of fabrication procedure.

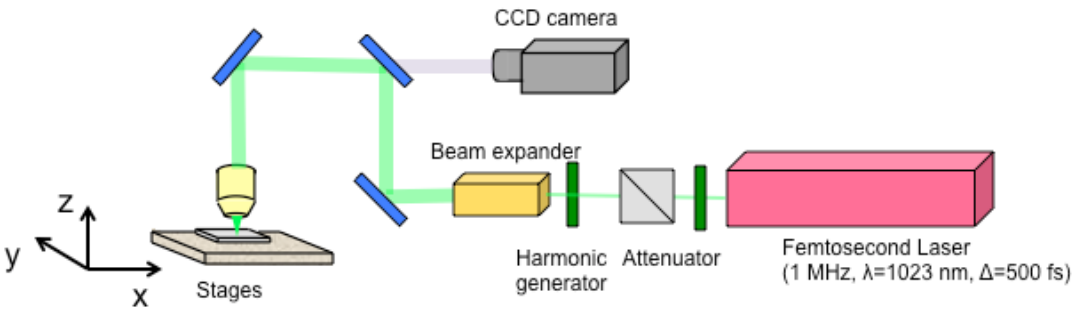

Figure 4.2. Schematic representation of the experimental setup used for 2PP photofabrication.

Patterns were fabricated by two-photon polymerization of a photo curable organic-inorganic polymer ORMOCER® (ORMOCOMP®, US-S4, Micro resist technology) as shown in Figure. 4.1. This polymer incorporates elements of inorganic oxidic glasses/ceramics (based on Si-O-Si bonds), polysiloxanes, and organic polymers. Consequently, it has properties of organic polymers combined with properties of glass-like materials [86]. Table 4.1 summarizes some properties of ORMOCER®. In addition, it is known that ORMOCER® is biologically non-toxic and compatible [19, 20, 87]. In order to remove unexpected effects from two different materials (glass/polymer), a glass cover slip was first coated with ORMOCER® and patterns were fabricated on the cured ORMOCER® layer. ORMOCER® resin was spin-coated on the cover slip at 8000 RPM for 100s, and pre-baked at 80 °C for 2 min on a hot plate, followed by curing with UV lamp for 30 min and hard-baking at 140 °C for 1 hour (Figure. 4.1(a)). The second ORMOCER® resin layer was spin-coated at 6000 RPM on the precoated surface and pre-baked at the same conditions.

The second layer was selectively cured by high repetition rate femtosecond (FS) laser irradiation (Figure. 4.1(b)). A frequency-doubled (wavelength of ~523nm) FS laser beam (pulse width <500 fs, repetition rate of 1 MHz, wavelength of 1045 nm, and typical M^2 factor of 1.3; FCPA μJewel D-400, IMRA America, Inc.) was focused into the resin by two different objective lenses; 50X objective (NA=0.55) and 10X objective (NA=0.28) (M Plan APO, Mitutoyo). Throughout the process, the laser focus was adjusted at the precoated/uncured ORMOCER® layer interface by careful tilting adjustment of the sample stage. The power of the laser beam emitted from the objective lens was measured by a power meter and controlled to the desired power level by an attenuator, including a half wave plate and a polarizing beam splitter (PBS). The sample was placed on a motorized X-Y stage that was controlled by a PC. A PC-controlled mechanical shutter was inserted in the laser beam path to illuminate the laser beam in a programmed and synchronized manner with the sample motion (Figure. 4.2).
After the laser exposure step, the samples were post-baked at 110 °C for 10 min on a hot

Table 4.1. Typical properties of ORMOCER®

Uncured resin	Viscosity 25°C	6–10 Pa·s
	Specific gravity	1.15 g/cm^3
	Refractive index	1.497
	Optical loss	0.05 dB/cm @ 633 nm 0.3 dB/cm @ 1310 nm 1.5 dB/cm @ 1559 nm
	Filtration	0.45 μm
Cured material	Thermal behavior	Duromeric
	Refractive index (@ 588 nm)	1.520
	Thermal expansion coefficient (20–100°C)	100–130 ppm/K
	Water absorption	<0.5%
	rms Roughness	2–4 nm

plate and developed with ORMODEV (Micro resist technology) for 30 min to remove uncured ORMOCER® resin (Figure. 4.1(c)), followed by rinsing with isopropanol (IPA) and deionized water three times. For cell experiments, the patterned samples were dipped in 70% ethanol to sterilize, and cured with UV lamp illumination for 30 min without hard-baking (Figure. 4.1(d)). For SEM imaging to measure critical dimensions of the fabricated patterns, the patterned samples were placed on a hot plate at 140 °C for 1 hour for hard baking before gold sputtering.

4.3. Experimental methods

4.3.1. Characterization of patterned surface

SEM, AFM, and ATR-FTIR spectra were used for physical and chemical characterization of patterned surfaces, respectively. In order to measure detailed shapes of the fabricated patterns, the glass substrate was broken normal to the patterns and sputtered with gold for SEM inspection (FE-SEM, Field Emission Scanning Electron Microscope), LEO 1550, Carl Zeiss). Non-contact mode of AFM (XE-NSOM, Park Systems) was used to image shallow patterns after cell culturing. In order to understand the surface chemistry of FS laser-induced cured patterns, compared to UV lamp cured surfaces, ATR-FITR spectra were recorded by a micro ATR-FTIR spectrometer system composed of an FTIR spectrometer (FT/IR-4100, JASCO Corp., Tokyo, Japan), a MCT detector, an IR microscope (IRT-1000, JASCO Corp., Tokyo, Japan), and a ZnSe prism. A total of 64 scans were integrated for each spectrum at 4 cm^{-1} wavenumber resolution and ~80×80 μm spatial resolution over the range of 600-5000 cm^{-1}. For ATR-FTIR measurement, a sample with dense ridge was fabricated under the conditions as follows: laser power of 2.5 mW, scanning speed of 1 mm/s and the pitch of each ridge was 5 μm.

4.3.2. Cell culture and fluorescence imaging

Cell growth and viability studies were performed using NIH 3T3 (Mouse fibroblast cells). The cells were grown in Dulbecco's Modified Eagle Medium (DMEM, Gibco Invitrogen), 10% fetal bovine serum (FBS, Gibco Invitrogen) and 100 units/ml penicillin (Gibco Invitrogen). The cells were plated on the patterned substrate in sterile polystyrene Petri dish and stored in a cell culture incubator maintained at 37 °C temperature in 5% CO_2 environment.

After NIH-3T3 cells had been cultured on a patterned substrate for one day, the cells were fixed with 3.7% formaldehyde (Fisher Scientific) for at least 10 min and permeabilized with 0.1% TritonX-100 (Fisher Scientific) for 5 min. Actin cytoskeleton was stained with 300 nM Alexa fluor 488 phalloidin (Invitrogen) for 20 min, and subsequently the nucleus was stained with 300 nM DAPI (Invitrogen) for 4 min.

The morphology of patterned cells was examined under an upright fluorescent microscope (AxioImager M1, Zeiss) with Plan Neofluar 10X objective lens (Zeiss). In order to observe sliced images of cells over patterns, a 510 Meta UV/VIS confocal microscope (Zeiss) with a W Plan Apochromat 63X N.A. = 1.0 dipping objective lens (Zeiss) was used.

4.3.3. Statistical analysis

The experiments were conducted independently three times for each sample/pattern; one sample/pattern was used for cell culturing three times or more. About 25 cells were randomly drawn from each experimental condition and used to conduct statistical analysis. Detailed numbers of cells are represented in the figure captions. The aspect ratio (Length/Width) was defined as the length of the cells stretched along parallel ridges or the higher ridges on mesh pattern over the width of the cells. The cell shape aspect ratio was obtained by the imaging software, AxiVision LE v 4.7.1.0., and the statistical analysis was carried out using software SPSS R15.0. Statistical significances were calculated by One-way ANOVA Bonferroni test with an error probability, $p < 0.05$.

4.4. Characterization of patterned surface

SEM images of typical fabricated patterns depict aligned ridges of various heights in Figure. 4.3(a) and orthogonally meshed patterns of two different heights in Figure. 4.3(b). Figure 4.4 shows the cross sectional view of a typical ridge feature fabricated with laser power of 2 mW and scanning speed of 1.0 mm/s, having FWHM (full width at half maximum) height and width of 18.3 μm and 1.8 μm, respectively. The crossing orthogonal patterns were intentionally fabricated in order to improve the mechanical strength of the drawn structures during breakage for cross-sectional view inspection. The ridge pattern height and width obtained by two different objective lenses are plotted as

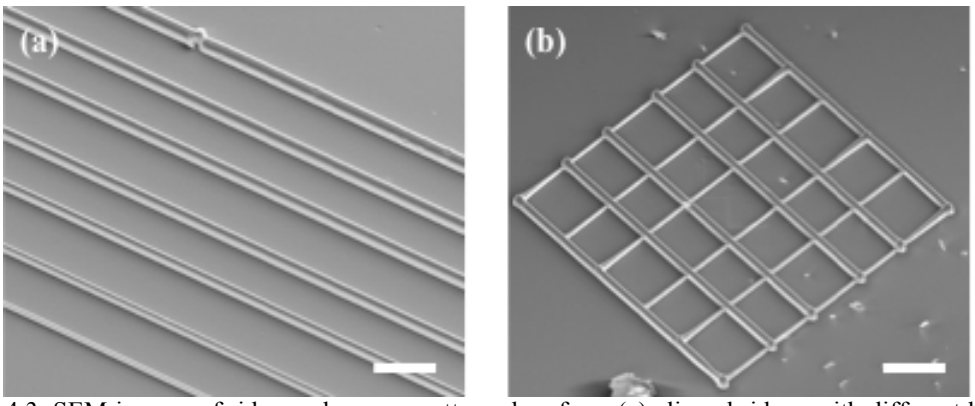

Figure 4.3. SEM images of ridge and groove patterned surface: (a) aligned ridges with different height, (b) orthogonally patterned mesh with different height. Scale bar = 20 μm.

functions of laser power and laser scanning speed in Figure. 4.5. Upon 50X objective lens illumination, the width of the pattern was in the range of ~0.8-3.4 μm, and the height up to ~20 μm, allowing maximum aspect ratio (height/width) of about 10. By utilizing the 10X objective lens, the height and width were ~10-16 μm and ~2.5-17 μm, respectively, allowing maximum aspect ratio (height/width) of about 4.

2PP has been shown to have potential for the fabrication of arbitrary three-dimensional structures [19-21, 87, 88]. In the present study, the effect of surface topography on fibroblast cell alignment was assessed by constructing on a single substrate line and mesh patterns of various heights by single-step femtosecond laser based 2PP. The pattern height and width were easily controlled by the laser power and scanning speed. 2PP based on relatively low NA objective lens readily enabled fabrication of high aspect ratio patterns (up to about 10), assisted by nonlinear self-focusing effect, as reported elsewhere in detail [76, 80, 81, 89].

On the other hand, the capability of producing high aspect ratio features via the current 2PP process may not be particularly favorable for defining low aspect ratio features. The lowest height produced by controlling laser power and scanning speed was about 0.8 μm. One way to overcome this issue is by using higher NA objective lens [20, 21, 88] and alternating with low NA objective lens. However, switching between different lenses requires a more elaborate control system in terms of laser focus adjustment and matching field of view. In this study, a simpler approach to obtain low aspect ratio features is presented by using a single objective lens, based on exploiting the nonlinear propagation characteristics of the ultra-short laser beam, i.e. the extended focal region due to the nonlinear self-focusing effect. A simple shifting of the laser focus along the beam propagation direction with respect to the interface between cured/uncured

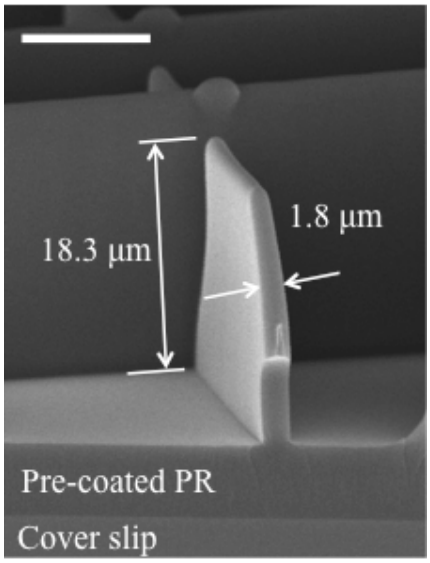

Figure 4.4. SEM image of a ridge. Laser power of 2 mW and scanning speed of 1.0 mm/s. Scale bar = 10 μm.

ORMOCER® layers was implemented [90]. The ridge height decreased upon shifting the laser focus into the precoated/cured ORMOCER® layer, hence limiting the penetration of the extended laser focal zone into the uncured ORMOCER® layer. Figure 4.6 shows the variation of the ridge height as a function of the position of the laser focal plane by the

50X objective lens, demonstrating precise control of the ridge height, even for low aspect ratio features, in addition to the rapid fabrication of high aspect ratio structures. Line patterns of 4-μm height were fabricated with laser power of 0.7 mW and scanning speed of 0.5 mm/s. The objective lens was shifted 1 μm upward into the precoated/cured ORMOCER® layer. The corresponding displacement of the actual focal point in the polymer is predicted to be ~1.5 μm, considering that the refractive index of glass and cured ORMOCER® is 1.52. The actual value deduced from the experiments was 1.42, consistent with our prediction.

For cell study, parallel line and orthogonal mesh patterns were fabricated by shifting the objective lens and changing the scanning speed. Parallel ridge patterns of ~1.5, ~0.8, and ~0.5-μm height were fabricated (Figure. 4.8). Orthogonal mesh patterns were constructed with ridge heights of ~8 and ~4 μm (Figure. 4.11). Other mesh patterns were also fabricated with height of ~5 μm, ~5.5 μm and ~6 μm (Figure. 4.12). The demonstrated single step ridge fabrication exemplifies the simplicity and speed of the current process.

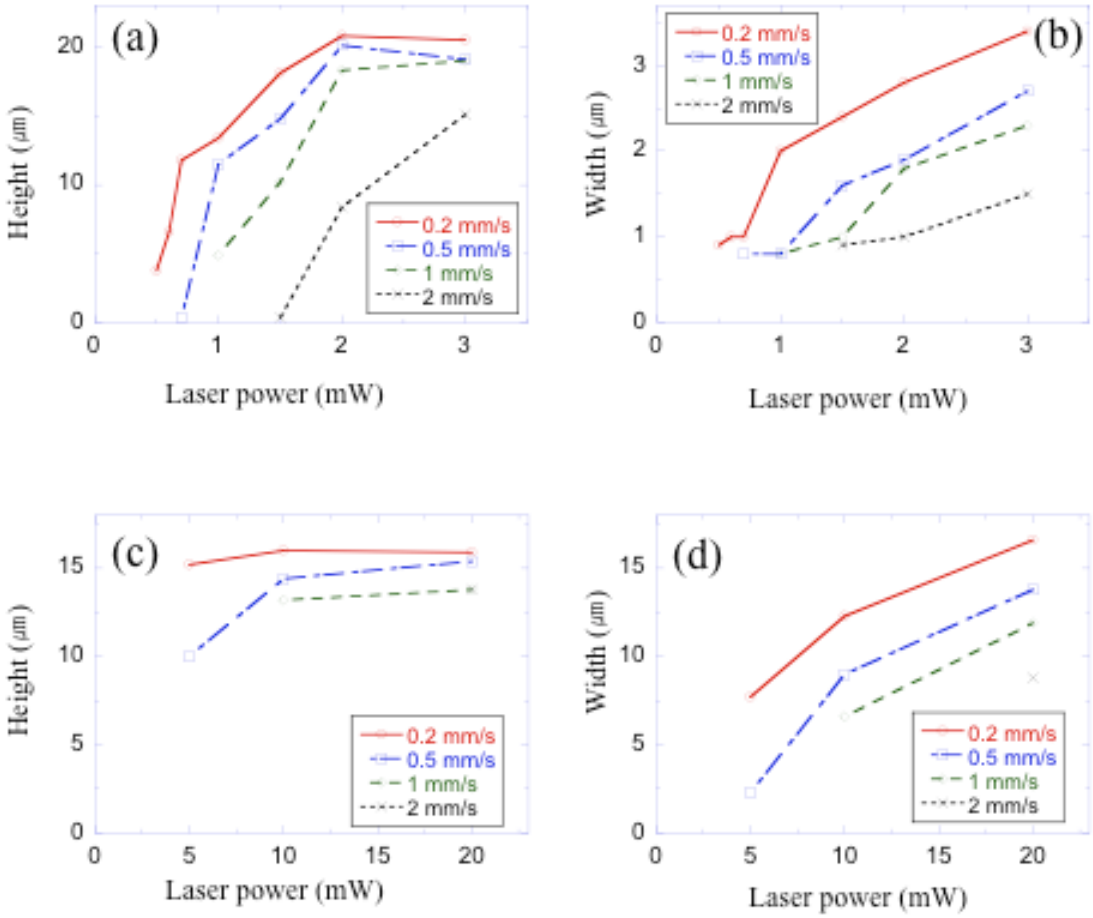

Figure 4.5. Influence of the laser power and scanning speed on the height and the width of the cured wall. The height and the width of the ridges cured by 50x (a, b) and 10x (c, d) objective lenses, respectively.

In Figure 4.7, the ATR-FTIR spectra measured from the ridge patterned area are compared with the spectra from UV cured precoated film. Important peaks are assigned to the corresponding vibrational modes; the broad peak at ~3440 cm^{-1} corresponds to the stretching mode of the O-H bonds, the bands at ~2962 cm^{-1} and ~2927 cm^{-1} to the stretching mode of C-H band, and the band at ~1725cm^{-1} to the stretching mode of C=O. The polar chemical groups increase the polarity of the surface, resulting in enhanced hydrophilicity. This wettability may facilitate the adhesion of cell to the substrate [73, 89]. The absence of significant difference in the measured spectra implies that the 2PP process by the ultrafast laser beam does not alter the biocompatible characteristics of the ORMOCER®, and that cell behavior based on the current laser fabrication method is mainly affected by surface topography rather than chemistry.

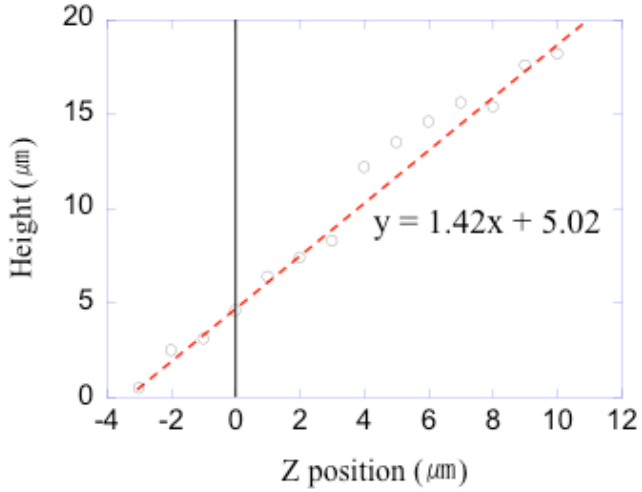

Figure 4.6. Influence of the position of laser focal plane on the height of the cured ridge. The vertical line at 0 μm means the interface of uncured and cured polymer resin. The height and the width of the ridges cured with 50X.

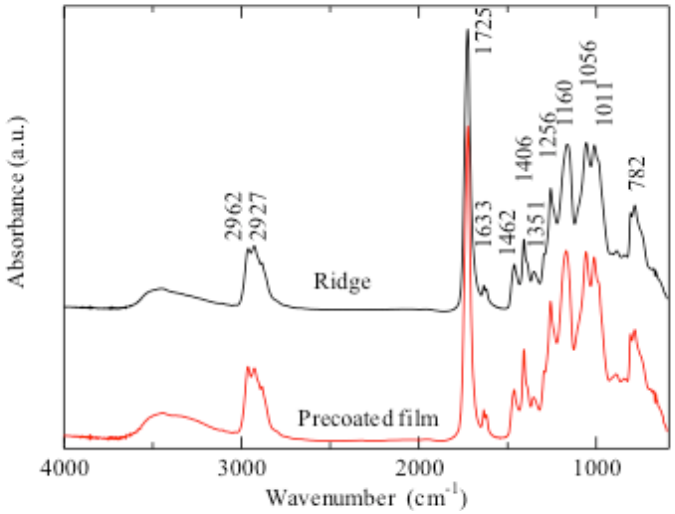

Figure 4.7. Micro ATR-FTIR spectra of ridges (femtosecond laser cured) and the bottom of grooves (precoated film, UV lamp cured).

4.5. Cell morphology and alignment

4.5.1. Cell behavior on parallel ridge patterns

The behavior of fibroblast cells (NIH-3T3) on the parallel ridge patterns was investigated and depicted in both phase contrast (Figure. 4.8(a)) and fluorescent images (Figure. 4.8(b)). In order to mark the accurate position of the cells relative to the patterned ridges, the phase contrast and fluorescent images were overlapped by image processing (Figure. 4.8(c)). Patterned regions of three different heights are observed in the figures; the highest feature region ((A), ~1.5 μm), the intermediate height pattern region ((B), ~0.8 μm), the lowest height pattern region ((C), ~0.5 μm), and the flat surface region (marked as (D)). The pitch between adjacent line patterns was maintained constant at ~20 μm. In region (A), most cells were located within the grooves formed by two neighboring ridges. All cells attained high length/width ratio, and their nuclei deformed to elliptical shapes. The cells in region (B) were aligned along the ridges, but the aspect ratio of elongated cells was smaller than in region (A). On the other hand, in region (C), most cells freely adjusted themselves over the ridges, and the elongation was clearly reduced. On the flat surface region (D), cells virtually showed no directionality and a typical flattened morphology. More detailed interaction between the cells and patterned ridge (800- and 200-nm high ridges) was shown in Figure 4.9. The AFM images obtain after cell fixation and drying. Figure 4.10 shows the cell aspect ratio dependence on the ridge height. The aspect ratio of cells increases linearly as the ridge height increases between ~0.8- and ~1.5-μm height ridges. The cells on these patterns tend to settle on the groove surface between ridges. They align along the parallel ridges they encounter and elongate by reducing their breadth to fit the area of groove. However, there is also no significant difference in the attained cell morphology on the ~0.5-μm high patterns compared to the flat surface. There is also no significant difference between the cells on ~2.2- and ~5-μm parallel ridge patterns, and the maximum mean value of the aspect ratio is ~8. It is noted that there are lower and upper bound thresholds that cells can sense and respond to.

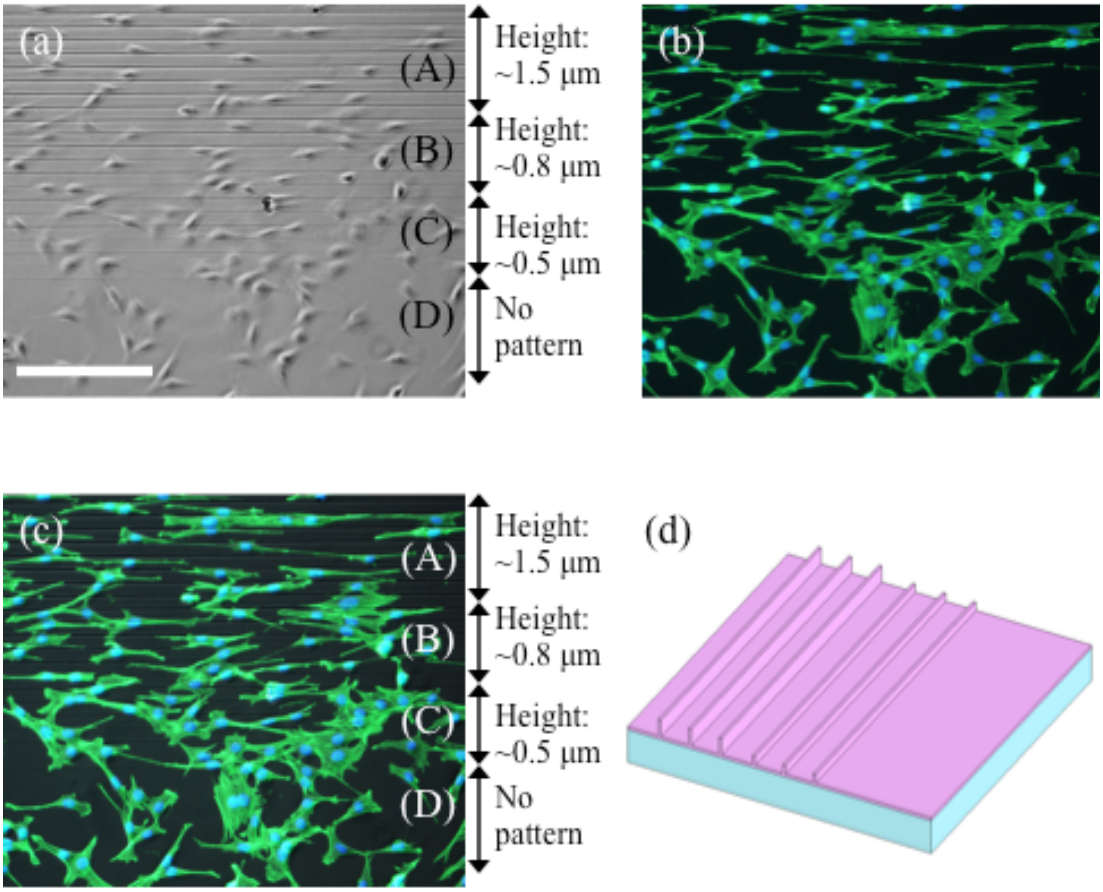

Figure 4.8. (a) Phase contrast, (b) fluorescent and (c) combined images are shown of cell nuclei (DAPI: blue) and actin cytoskeletal networks (Alexa Fluor 488 phalloidin: green). NIH-3T3s cultured for 24 hours are shown in various height line patterns. (d) Illustration of patterned surface of aligned ridges with different height. Scale bar = 100 μm.

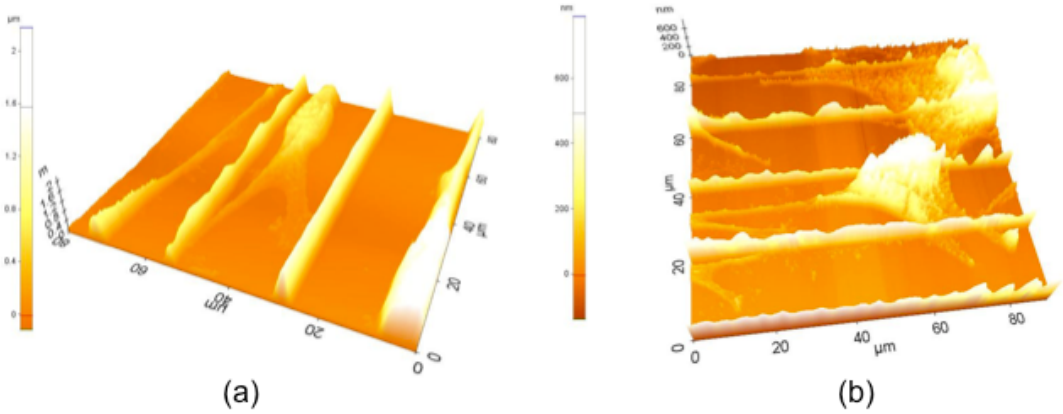

Figure 4.9. AFM images of cells between (a) 800-nm high ridge and (b) 200-nm high ridge patterns.

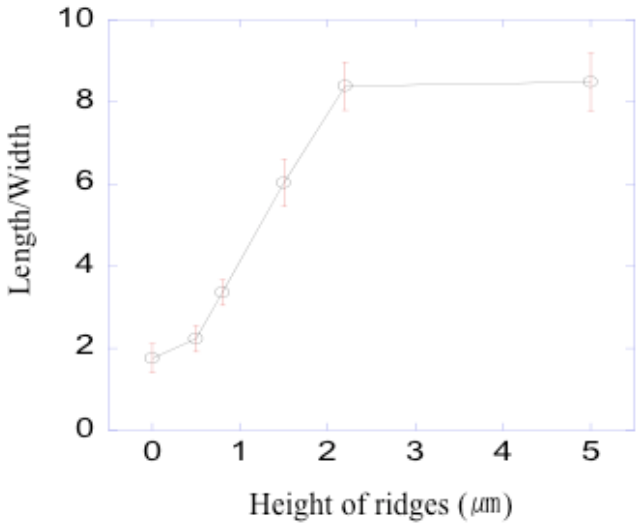

Figure 4.10. The aspect ratio of the elongated cells on different height parallel ridge patterns (mean±standard error, $F(5, 137) = 35.3$, $p < 0.05$). The numbers of cells for each data point are 23 (control), 24 (0.5 μm), 23 (0.8 μm), 25 (1.5 μm), 24 (2.2 μm), 24 (5 μm), respectively.

4.5.2. Cell behavior on orthogonal mesh patterns

Orthogonal mesh patterns consisting of horizontal and vertical lines of different heights were also used to observe cell alignment. Figure 4.11 shows cells on orthogonal mesh patterns composed of two different heights (~8 μm and ~4 μm) with a pitch of ~20 μm. The partial orthogonal mesh patterns define four different regions, as marked in the figure; (A) no patterns, (B) vertically parallel lines of ~8-μm height, (C) horizontally parallel lines of ~4-μm height, and (D) orthogonally meshed lines. Cells showed the already observed typical behavior (as in Figure. 4.8) in regions (A), (B), and (C). In region (D) they aligned along the higher ridges and attained smaller aspect ratio compared with those in the regions (B) and (C). The ~4-μm and ~8-μm ridges are high enough to affect cell alignment and elongation. However, when coupled in mesh patterns, the cells aligned along the higher ridges (Figure. 4.11). Occasionally, some cells stuck on the bottom of grooves between ridges, but most bridged across ridges of ~4-μm height and extended in length. In order to observe the three-dimensional shape on the mesh patterns, cells were observed using a confocal microscope. Figure 4.12 shows confocal slice images taken at the bottom of the grooves (Figure. 4.12(a)), at 2 μm (Figure. 4.12(b)), and 4 μm (Figure. 4.11(c)) away from the bottom surface. The cell rested on ridges (Figure. 4.12(c)) and appeared hanging across the neighboring horizontal ridges (Figure. 4.12(b)). Only cell edges attached to the groove bottom (Figure. 4.12(a)).

In order to measure the threshold height of patterns affecting cell alignment, cells were cultured on mesh patterns of smaller height difference between the orthogonally crossed ridges (Figure. 4.13), and mesh patterns consisting of same height ridges (images not shown). Figure 4.13(a) shows cultured cells on mesh patterns with vertical lines of ~5-μm height and horizontal lines of ~5.5-μm height. While cell alignment was distinct on the

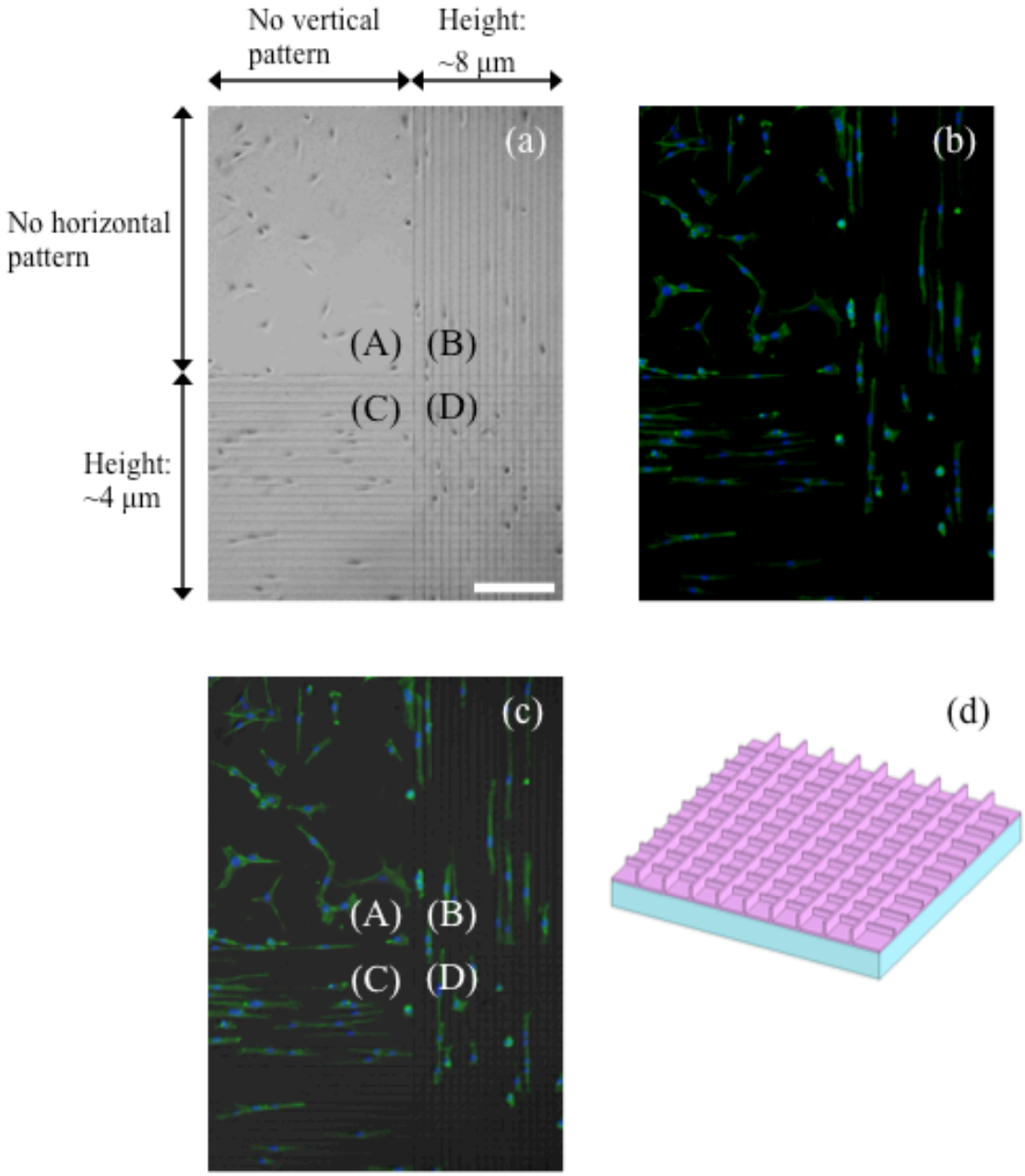

Figure 4.11. (a) Phase contrast, (b) fluorescent and (c) combined images are shown of cell nuclei (DAPI: blue) and actin cytoskeletal networks (Alexa Fluor 488 phalloidin: green). NIH-3T3s cultured for 24 hours are shown in various height line patterns. (d) Illustration of patterned surface of aligned ridges with different height. Scale bar = 200 μm.

parallel line patterns, no clear alignment trend could be observed on the mesh patterns. Figure 4.13(b) shows cultured cells on mesh patterns having vertical lines of ~5-μm height and horizontal lines of ~6-μm height. The cell aspect ratio dependence on the height difference between the crossed horizontal and vertical ridge patterns was also extracted from these micrographs (Figure. 4.14). No significant difference could be distinguished between the cells on 0- and 0.5-μm height gap mesh patterns. In the case of height difference near ~1 μm, aligned and elongated cells were inspected. The threshold height to affect cell alignment is similar to that on parallel line patterns in Figure 4.8, although the maximum mean aspect ratio is about 4 (on 4-μm height difference), which is smaller than that of cells on parallel patterns of similar height (5-μm).

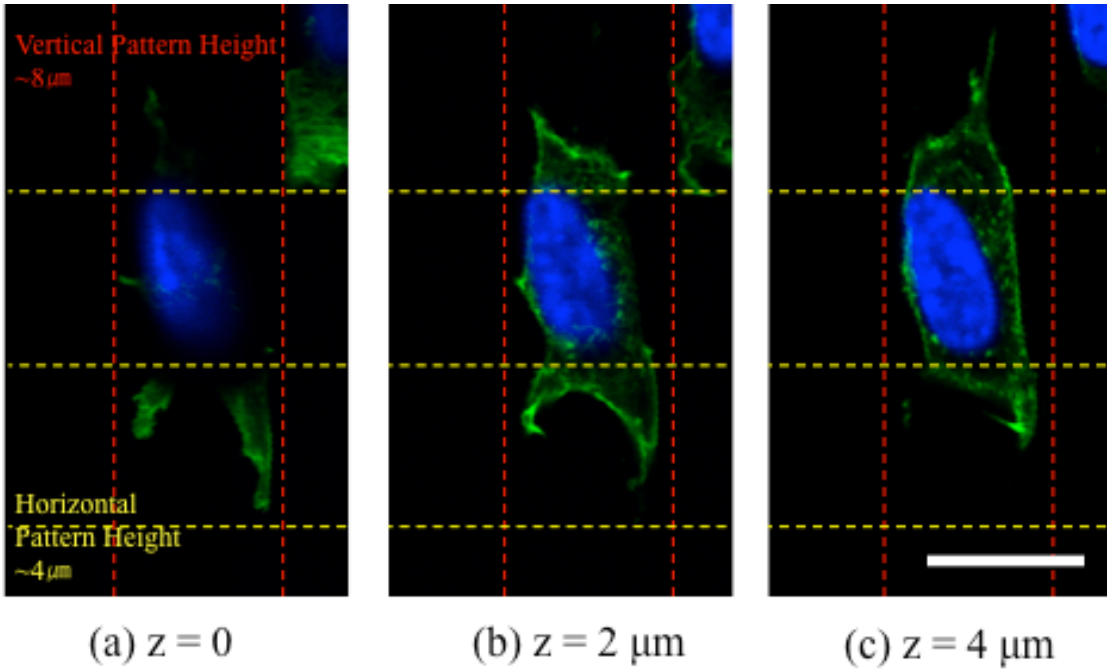

Figure 4.12. Fluorescent confocal slice images are shown of cell nuclei (DAPI: blue) and actin cytoskeletal networks (Alexa Fluor 488 phalloidin: green) at z=0 (a, at the bottom of grooves), at z = 2 μm apart from bottom (b) and z = 4 μm apart from bottom (c). NIH-3T3s cultured for 24 hours are shown in different height mesh patterns. Red and yellow dashed line is the place where ridges with the height of ~8 μm and ~4 μm. Scale bar = 20 μm.

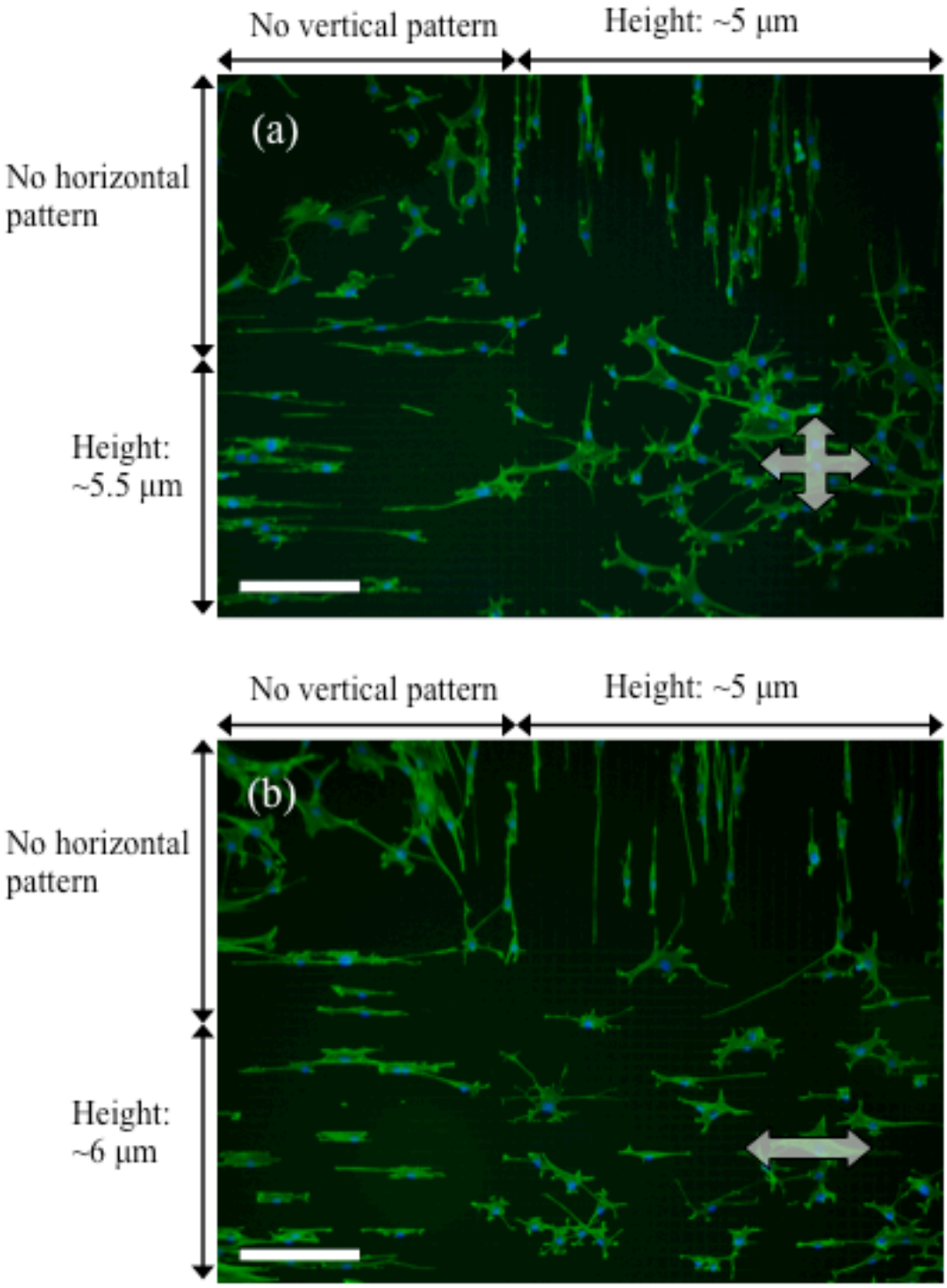

Figure 4.13. Fluorescence images of cell alignment on the orthogonally patterned mesh surface with small difference of height between horizontal and vertical ridges. Scale bar = 200 μm for both.

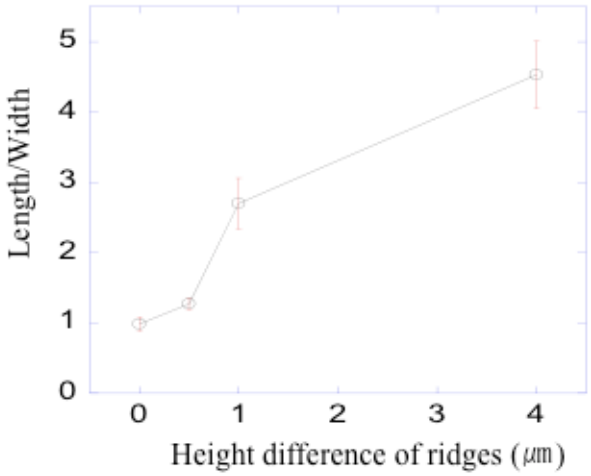

Figure 4.14. The aspect ratio of the elongated cells on different height gap orthogonal mesh patterns (mean±standard error, $F(3, 104) = 34.5$, $p < 0.05$). The numbers of cells for each data point are 37 (0), 25 (0.5 μm), 17 (1 μm), 29 (4 μm), respectively.

4.6. Conclusion

In this chapter, we proposed and demonstrated the fabrication of multi-height patterned surfaces by femtosecond laser induced two-photon polymerization. The ridge height is controlled by changing the laser beam power, scanning speed and focal position. High aspect ratio ridges (height / width ratio >10) are fabricated by only transversely scanning the laser focal zone. NIH-3T3 cells were cultured on patterned substrates. Various cell morphologies were observed depending on the height and type of patterns. The threshold obstacle height for cell alignment was found near ~1 μm. By combining ridges and grooves of different height it is expected to control cell morphology and therefore enhance our ability to design biomaterials for tissue engineering. This technique is also useful for producing arbitrary patterns incorporated in microdevices for trapping or controlling cells and studying the influence of surface topology.

Chapter 5

Cell migration on anisotropic mesh patterns

Although both micro and nanoscale surface topography have been known to be important in understanding cell-materials interactions, typically only simple patterns (e.g., parallel lines or aligned posts) have been used in studying cell morphology, migration, and behavior. This restriction has led to limited understanding of the multidirectional aspects of cell-surface responses. The present study was performed to investigate cell morphology and motility on micronscale anisotropic cross patterns and parallel line patterns having different aspect ratios (1:2, 1:4, and 1:∞), grid size (12-, 16-, and 24-μm distance neighboring longer side ridges), and height of ridges (3- and 10-μm). The movement characteristics were analyzed quantitatively with respect to cell migration speed, migration angle, persistence time (P) and motility coefficient (μ). A significant effect of the 1:4 grid aspect ratio cross patterns and parallel line patterns on cell alignment and directionality of migration was observed. Cell motility was also dependent on the patterned surface topography: the migration speed was significantly enhanced by the 1:2 and 1:4 cross patterns when the grid size was smaller than the size of individual cells (i.e., ~ 16 μm). In addition, the migration speed of cells on shorter patterns was greater than on higher ridges. Overall, cell morphology and motility was influenced by the aspect ratio of the cross pattern, the grid size, and the height of ridges [91].

5.1. Introduction

Cell responses to chemically patterned surfaces can be effectively categorized with respect to the patterning scale of specific chemistries, while cell response to topography is classified based on the pattern topography (isotropic or anisotropic) [25]. Chemically patterned surfaces on the micronscale have been exploited for some time to spatially define the position and shape of cells, and to study these perturbations on cell

function such as protein and gene expression, differentiation, and mechanotransduction [5, 92, 93]. Furthermore, nanoscale patterned surfaces have been used to regulate more collective cell function such as proliferation, differentiation and molecular arrangement [94, 95]. In contrast to chemical patterning, uniformly or randomly textured surfaces on the micron and nanoscale have been used to study cell adhesion, spreading, migration and phenotype [96, 97]. Anisotropic topographic patterns induce cell alignment and dictate the degree of migration along grooves and ridges [2-4, 73, 84, 98]. Kaiser et al. studied the effect of topography on cell shape, cell orientation, migration angle, and velocity, with 10 differently structured parallel line patterns and concluded that the reaction of the surface structure might be far more complex than generally assumed [4]. In spite of the importance of the topographic anisotropy, however, more often parallel straight line patterns have been exploited for understanding the interaction between cells and topographic surfaces. Recently, May et al. reported that a microfabricated grid-patterned topographically structured surface enables multidirectional cell stimulation [41]. They demonstrated that cells respond to multidirectional stimulation and exhibit intracellular signal transduction on grid patterns. However, they did not report on the cell response to varying anisotropy of topographical patterned surface. The multidirectional grid-patterned substrates were also reported that they can control directional migration of cells [99]. Inspired by these observations, we investigated how the topographic anisotropy can influence fibroblast behavior.

In this study, we demonstrate anisotropic cross patterns and parallel line patterns with ridges in a range 1- to 2-μm width can be fabricated by two-photon induced polymerization with a photosensitive organic-inorganic hybrid polymer. The patterns can exert contact guidance stimulation in multiple directions with different efficiency, depending on the grid aspect ratio. We examined the behavior of NIH3T3 fibroblasts cultured on the surfaces with three different aspect ratios of 1:2 grid, 1:4 grid, and parallel line patterns (1:∞). The morphology of the cells was characterized on different aspect ratio and grid patterns with respect to their orientation and elongation, based on fluorescent images acquired using an epifluorescent confocal microscopy. The motility of the cells was analyzed quantitatively with respect to migration angle and speed by long term monitoring of cell migration. General migration parameters, cell motility coefficient (μ) and persistent time (P), were calculated by using the persistent random walk model. Moreover, the cell migration enhancement due to cross pattern shape and size was studied.

5.2. Pattern fabrication by two-photon polymerization

The micron scale cross patterns and parallel line patterns were fabricated with photosensitive organic-inorganic hybrid polymer ORMOCER® US-S4 on glass substrates using the two-photon polymerization technique.

In order to prepare a precoated substrate, the photosensitive resin (PR) was coated on a glass cover slip by a spin coater at 8000 RPM for 100s, prebaked at 80 °C for 2 min

on a hot plate, cured with a UV lamp for 30 min, and hard baked at 140 °C for 1 hour (Figure. 5.1(a-b)). The PR was spin coated again at 6000 RPM on the precoated surface and prebaked with the same conditions (Figure. 5.1(c)). Femtosecond laser pulses (<500 fs, 1 MHz, 1045 nm, FCPA μJewel D-400, IMRA America, inc.) were frequency-doubled to the wavelength of ~523 nm and focused onto the interface between precoated surface and uncured PR through the glass cover slip using a M plan apo 50X N.A. = 0.55 microscope objective (Mitutoyo) (Figure. 5.1(d)) that is the same system with the one described in the previous chapter 4.2 (Figure 4.2).

The power of the laser beam emitted downstream of the objective lens was measured by a power meter and controlled by a half wave plate and a polarizing beam splitter. The exposure duration was controlled by a mechanical shutter. The sample was placed on a motorized X-Y stage. The desired micropattern was fabricated by a mechanical shutter and computer controlled stages. The laser power of 0.5 mW and scanning speed of the stages of 0.2 mm/s were set to fabricate ~3-μm height ridge patterns. The laser power of 1 mW and scanning speed of the stages of 0.5 mm/s were set to fabricate ~10-μm height ridge patterns, as detailed in the previous chapter.

After the laser irradiation, the samples were baked at 110 °C for 10 min, and uncured resin was removed by immersing in developer (ORMODEV, Micro resist technology) for 30 min. Thereafter, the samples were rinsed successively with isopropyl alcohol (IPA) and deionized (DI) water three times (Figure. 5.1(e)). Finally, samples were placed on a hot plate at 140 °C for 1 hour for hard baking and dipped in 70% ethanol for sterilization prior to use. Figure 5.2 illustrates critical features of the polymerized micro-patterns. Three different aspect ratio cross patterns (W:L = 1:1, 1:2 and 1:4) and a parallel stripe pattern (W:L = 1:∞) were designed and fabricated with

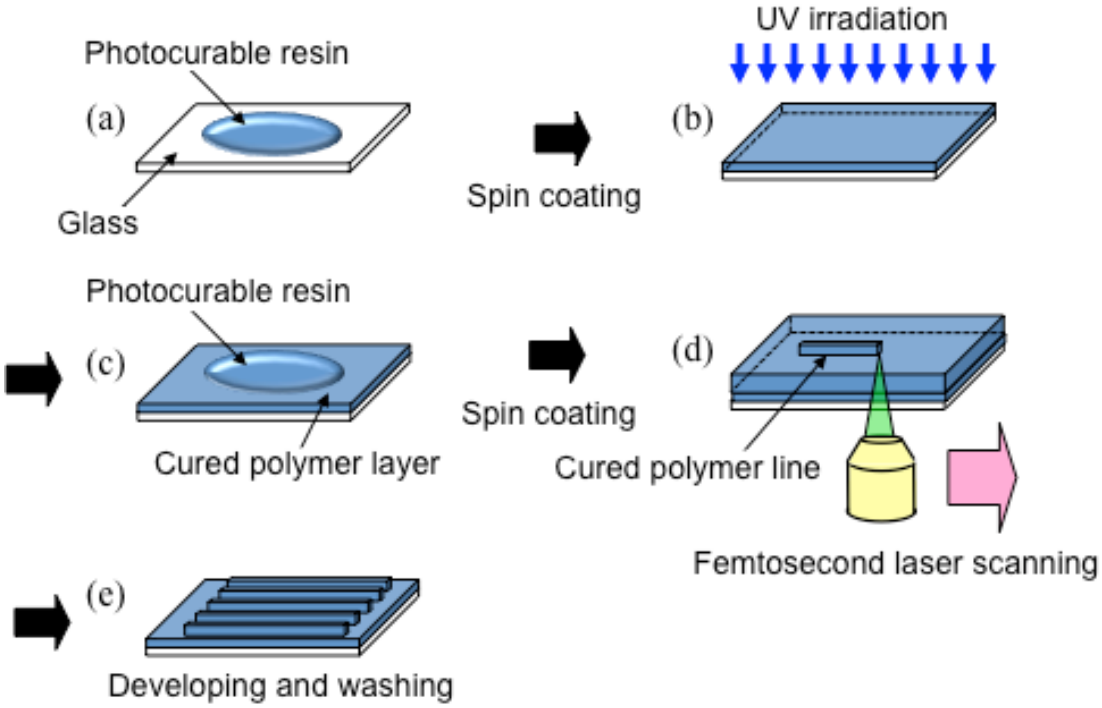

Figure 5.1. Illustration of fabrication procedure.

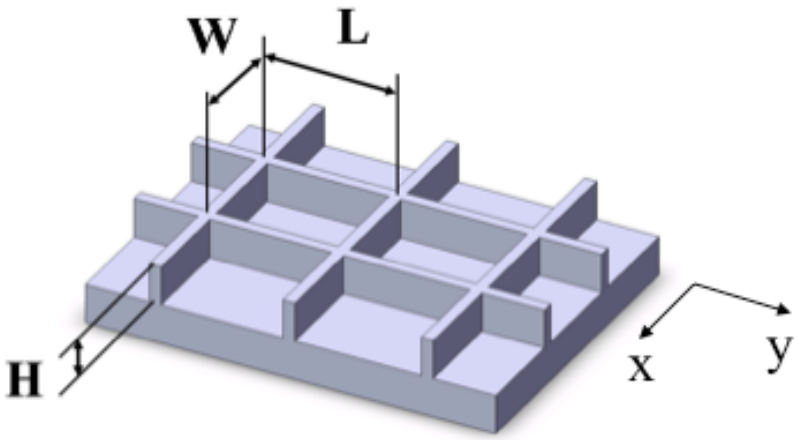

Figure 5.2. Schematic diagram of a part of fabricated cross patterns.

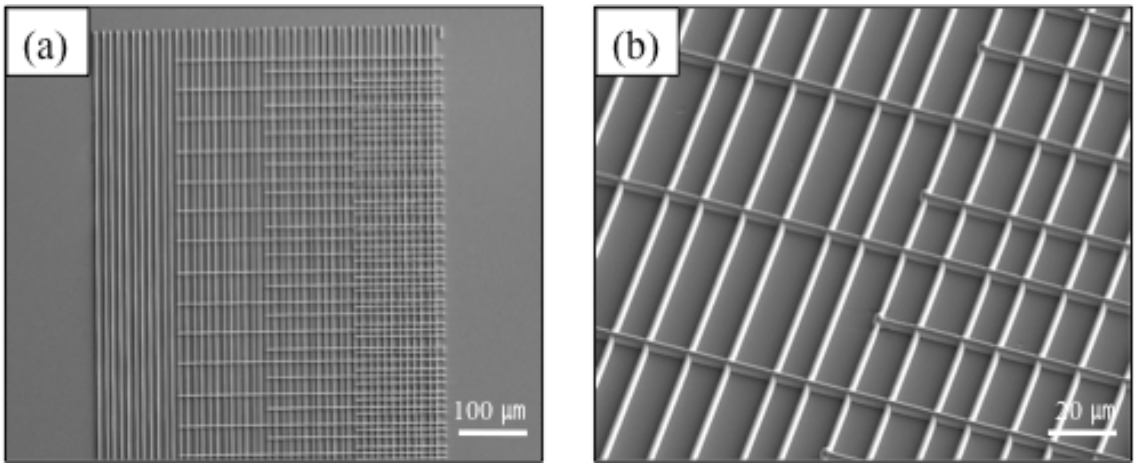

Figure 5.3. Scanning Electron Microscopy (SEM) images of a patterned surface: (a) top view of 12 × 12 μm^2 (1:1), 12 × 24 μm^2 (1:2), 12 × 48 μm^2 (1:4) cross patterns and a parallel stripe ridges 12 μm apart, (b) enlarged image of 12 × 24 μm^2 (1:2) and 12 × 48 μm^2 (1:4) cross patterns.

three different pitches between neighboring longer side ridges (W = 12 μm, 16 μm and 24 μm) and two different height of ridges (H = 3 μm and 10 μm). Figure 5.3 shows a SEM images of a test pattern which had 12-μm pitch (W) and 3-μm height (H) of ridges, and three different types of cross patterns (12 × 12, 12 × 24 and 12 × 48 μm^2) and one parallel stripe pattern. Typical width of the ridges was ~1-2 μm.

The cross patterns of 24 × 48 and 24 × 96 μm^2 were sufficiently large for a single NIH3T3 cell to fit inside of a rectangular grid area. The other patterns were smaller than an individual NIH3T3 cell, where the cross patterns of 12 × 48 and 16 × 32 μm^2 have similar grid area at almost half the cell size. The height of shorter side ridges and longer side ridges were designed to be the same; however, a slight (< 200 nm) difference in the height of the two crossing ridges is noticed at the intersection, since the first polymerized ridges affect the laser beam intensity profile or path during the writing process. It is assumed that this difference is not significant in this study because the height difference is present on every crossing position, and we are observing cell migration on the whole area of the patterns, even though the nanometer scale height difference can be effective on cells locally.

5.3. Experimental methods

5.3.1. Cell culture and imaging

NIH3T3 cells were maintained in Dulbecco's Modified Eagle Medium (Gibco Invitrogen), 10% fetal bovine serum (FBS) (Gibco Invitrogen) and 100 units/ml penicillin (Gibco Invitrogen) in 75-cm^2 culturing flask (Corning) at 37 °C and 5% CO_2 culture incubator. Before experimentation, confluent cells were detached from the flask by 0.05% Trypsin-EDTA (Gibco Invitrogen) and seeded onto the patterned substrate in sterile polystyrene well plates and placed in an incubator maintained at 37 °C and 5% CO_2. After one day, the cells were fixed with 3.7% formaldehyde (Fisher Scientific) for 10 min, and permeabilized with 0.1% TritonX-100 (Fisher Scientific) for 5 min. Actin cytoskeleton was stained with 165 nM Alexa Fluor® 488 phalloidin (Invitrogen) for 20 min, and subsequently nucleus was stained with 300 nM DAPI (Invitrogen) for 4 min. Samples were kept in PBS and turned over for the inspection by an upright fluorescent microscope (AxioImager M1, Zeiss) with Plan Neofluar 10X objective lens (Zeiss). A 510 Meta UV/VIS confocal microscope (Zeiss) with a W Plan Apochromat 63X dipping objective lens (Zeiss) was also used to visualize the morphology of fluorescent-stained cells on patterns in more detail.

For time-resolved image acquisition, cells were initially cultured on patterned substrata and maintained in CO_2-independent media (Gibco Invitrogen), 10% FBS, 100 units/ml penicillin, and 1% GlutaMAX (Gibco Invitrogen) at 37°C incubator. Five hours after cell seeding, monitoring of cell migration was started on a home-built inverted microscope with maintaining temperature at 37°C. Transmission images were taken every 5 minute with a digital CCD camera (Retiga 2000R cooled, Qimaging) for 400 min (~ 7 h).

5.3.2. Time-lapse microscopy and imaging analysis

Ten spread and migrating cells, isolated from each other, were randomly selected for statistical analysis in each independently repeated experiment; 80 data points for each case (images taken every 5 min for 400 min) and 800 data points in total for each independent experimental condition. From each image, identified cells were tracked and matched, and relative cell displacement (d_x and d_y) between the matched centers of nucleus of cells were measured for each time step. Trace line is plotted (by connecting the positions of single cells in time sequence during migration) in order to provide the time history of cell migration. The initial position of each cell is assigned to a common origin. Experiments were repeated 3-5 times independently for different patterns.

From the measured displacement and the applied inter-frame time (Δt= 5 min), migration vectors (V_x and V_y) and migration speed ($S_{migration}$) are calculated for each time step, and average values are calculated for the entire migration periods:

$$V_x = \frac{d_x}{\Delta t} \tag{5.1}$$

$$V_y = \frac{d_y}{\Delta t} \tag{5.2}$$

$$S_{migration} = \sqrt{V_x^2 + V_y^2}\ . \tag{5.3}$$

The average cell migration angle ($\theta_{migration}$) is also calculated in similar way using the displacement data:

$$\theta_{migration} = \arctan\left(\frac{|d_y|}{|d_x|}\right) \tag{5.4}$$

The $\theta_{migration}$ takes values between 0° and 90°. The 90° orientation corresponds to the *y*-direction which is the direction along the parallel line pattern (for 1:∞) and the longer side ridge of cross pattern (for 1:1, 1:2 and 1:4), while the 0° orientation corresponds to the *x*-direction that is normal to the parallel line pattern (Fig. 2) or the direction of shorter ridges for cross patterns. Accordingly, random cell migration on a flat surface should correspond to $\theta_{migration}$ = 45°. Conversely, specific directional stimulus on cells by topographical patterns forces the angle to attain values smaller or exceeding 45°.

5.3.3. Measurement of cell migration parameters

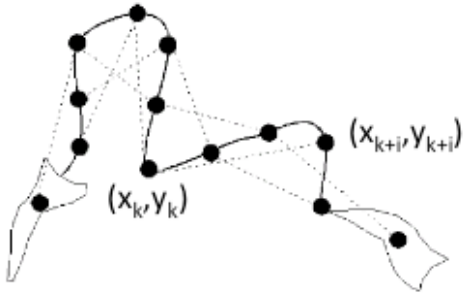

Figure 5.4. Schematic of the overlapping time interval sample. Each circle marks the recorded position of cell nucleus at a given time interval during cell migration. Only the case of three time intervals is shown in this example [102].

The persistence random walk model was also used for characterize the cell motility. The mean squared displacement, $< d^2 >$, *versus* time increment was calculated by using the overlapping time interval sample method and averaged all the squared displacement [100]:

$$< d^2 >= \frac{1}{N-i+1} \sum_{k=0}^{N-i+1} \left[\left\{ x((i+k)\Delta t) - x(k\Delta t) \right\}^2 + \left\{ y((i+k)\Delta t) - y(k\Delta t) \right\}^2 \right] \tag{5.5}$$

where N is the total number of time intervals over the entire cell migration track, and x and y are the coordinates of each position. Figure 5.4 shows the case of N=3. By fitting the following theoretical expression to the mean squared displacement data acquired from cell tracking, estimates of P and μ can be obtained [35, 100-102]:

$$\left\langle d^2(t) \right\rangle = 2 n_d \mu \left\{ t - P\left[1 - e^{-t/P} \right] \right\} \tag{5.6}$$

where n_d represents the number of dimensions tracked, which is set to 2, P is the persistent time which marks a length of time over which the cell moves along the substrate without experiencing drastic change in direction, and μ indicates a random migration coefficient, which is defined as [101]:

$$\mu = \frac{S^2 P}{n_d}, \tag{5.7}$$

where S is the speed of cell movement. The values of P and μ reported in the study are calculated from the experimental data for time up to $t_{max}/3$ (one third of the total duration of the migration path) since the true path of cell movement cannot be observed at longer times [35, 103]. In addition, the cells whose experimental displacement data do not match a theoretical curve were also excluded. Thus, seven to nine typical cells were chosen to calculate P and μ for each experimental condition.

Statistical analysis is performed to compare the average migration speed, migration angle, persistent time, and migration coefficient for each sample using software SPSS v15.0. Statistical significance was calculated by one-way ANOVA with Bonferroni post hoc test with an error probability considered only at $p < 0.05$.

5.4. Cell morphology on anisotropic patterns

NIH3T3 cells were observed to extend protrusions along the guiding ridges with 3 μm-height 24 h after seeding, while cells attached on a flat surface spread freely and were randomly oriented (Figure 5.5). On 1:1 cross patterns cell alignment was random and similar to the behavior on a flat surface, although the size of adhered cells was smaller than that of cells on a flat surface due to the confined geometry of the ridge patterns and more stretched protrusions following the ridges (Figure. 5.5 (a), (h), and (o) for 12 × 12, 16 × 16 and 24 × 24 μm^2, respectively). On 1:2 cross patterns cells neither oriented along longer ridges nor elongated like cells on parallel stripe patterns (Figure 5.5 (b), (i), and (p) for 12 × 24, 16 × 32 and 24 × 48 μm^2, respectively). The cells on 24 × 48 μm^2 pattern tended to be constrained in rectangular grid areas (Figure 5.5 (p)). However, in general, the morphologies of cells on both 1:1 and 1:2 patterns looked similar. In contrast, the elongation and orientation of the cells were clearly observed on 12 × 48 and 16 × 64 μm^2 patterns (Figure 5.5 (c) and (j)). The elongation and orientation were not observed on 24 × 96 μm^2 pattern, where the cells were held in rectangular grid areas (Figure 5.5 (q)). F-actin stress fibers were observed to form and extend along the ridges on all cross patterns except the 24 × 96 μm^2 pattern. This finding reveals that cells on grids of smaller area than single cells would be exposed to multidirectional stimulation while attaching and migrating. Finally, the cells on parallel line patterns show significant elongation and orientation for all different gaps (Figure. 5.5 (d), (k), and (r) for 12 × ∞, 16 × ∞ and 24 × ∞ μm^2, respectively).

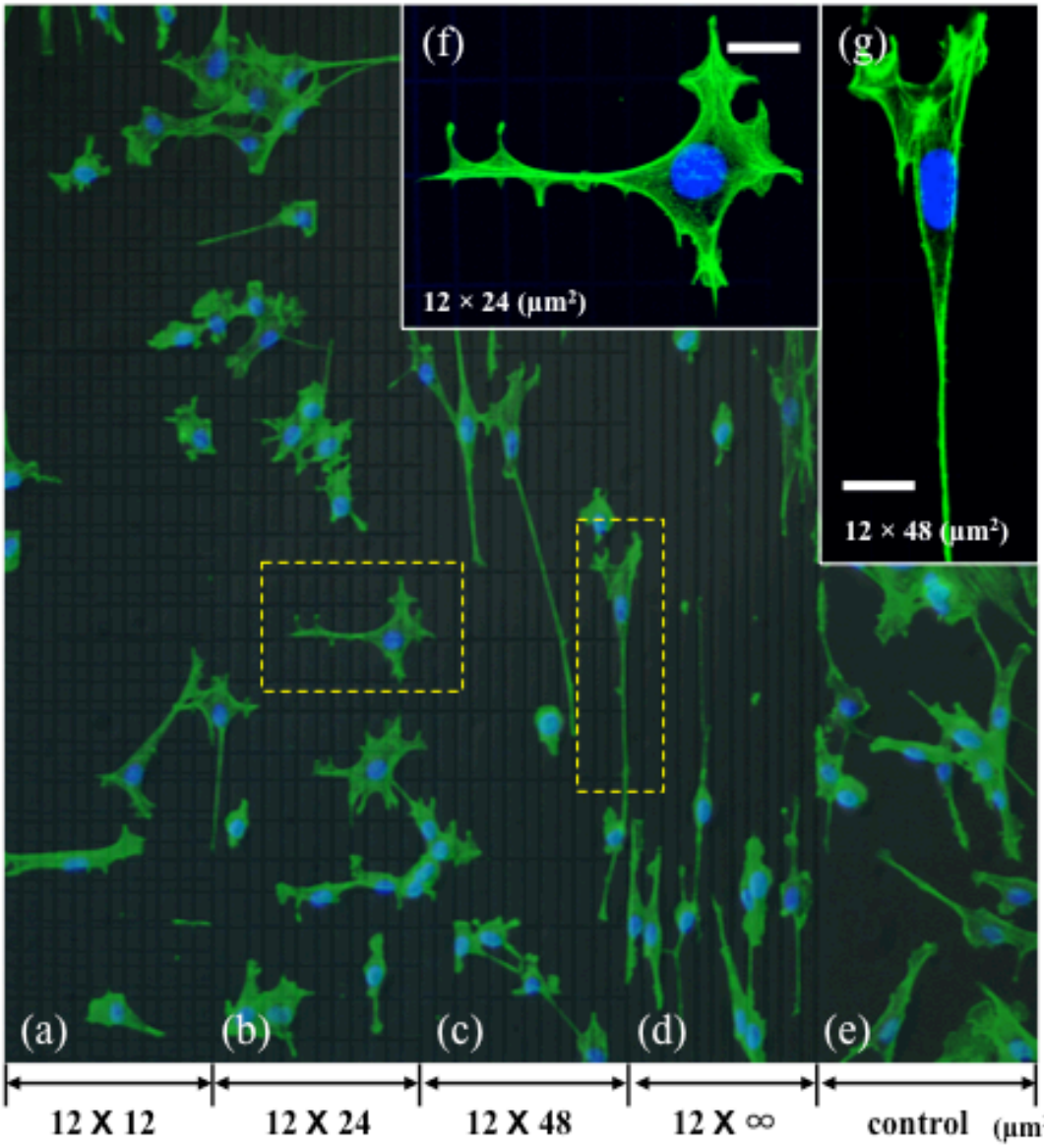

Figure 5.5. Fluorescence microscope images of cultured NIH3T3 cells 24 h after seeding on (a-e) 12-μm, (h-l) 16-μm and (o-s) 24-μm pitch of ridges with 3-μm height patterned surface. Insets in (a-e), (h-l), and (o-s) are magnified confocal microscope images of cells on patterns surrounded by dashed rectangular. (green : F-actin stained with Alexa Fluo 488, blue : nuclei stained with DAPI).

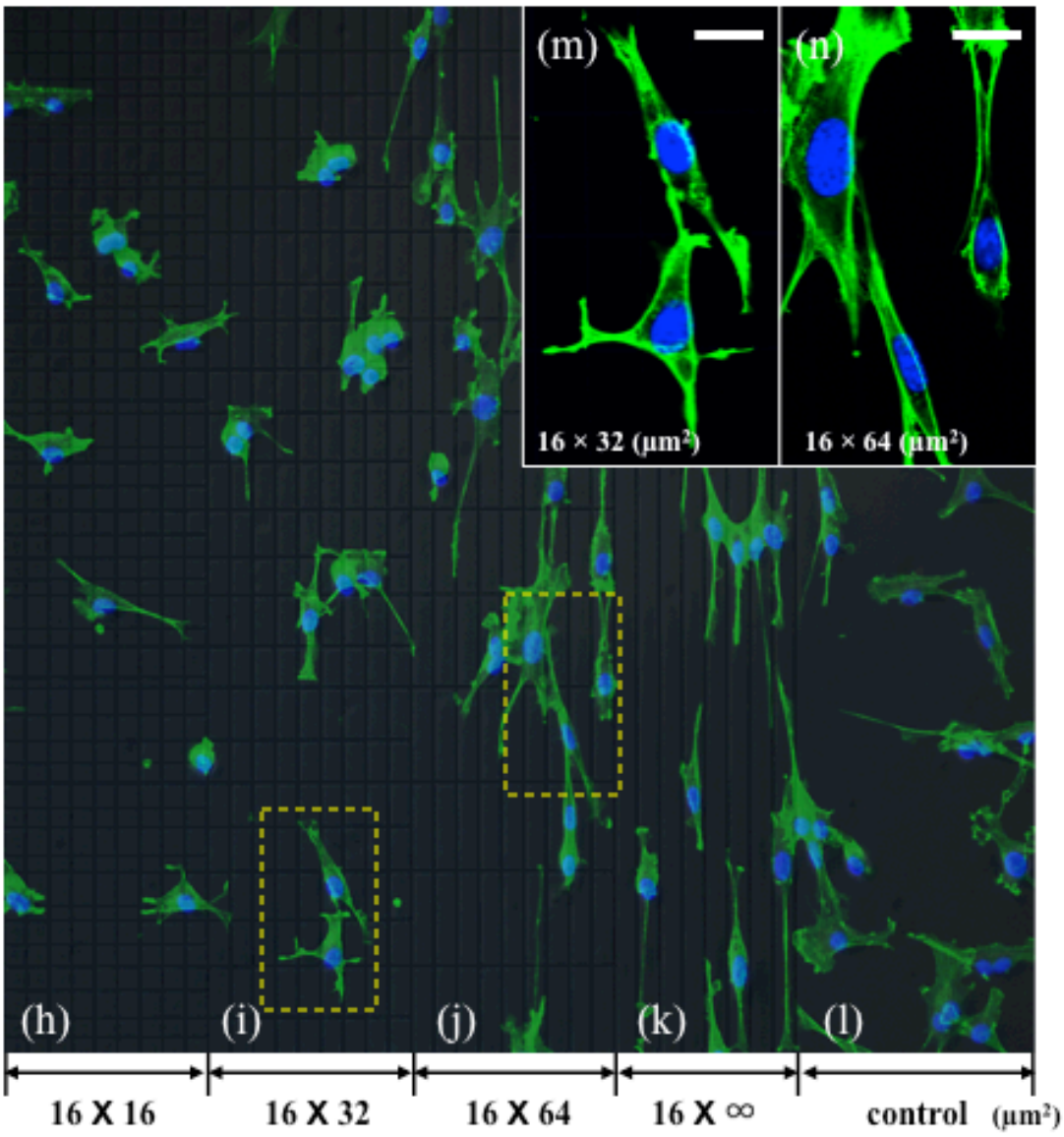

Figure 5.5. continued.

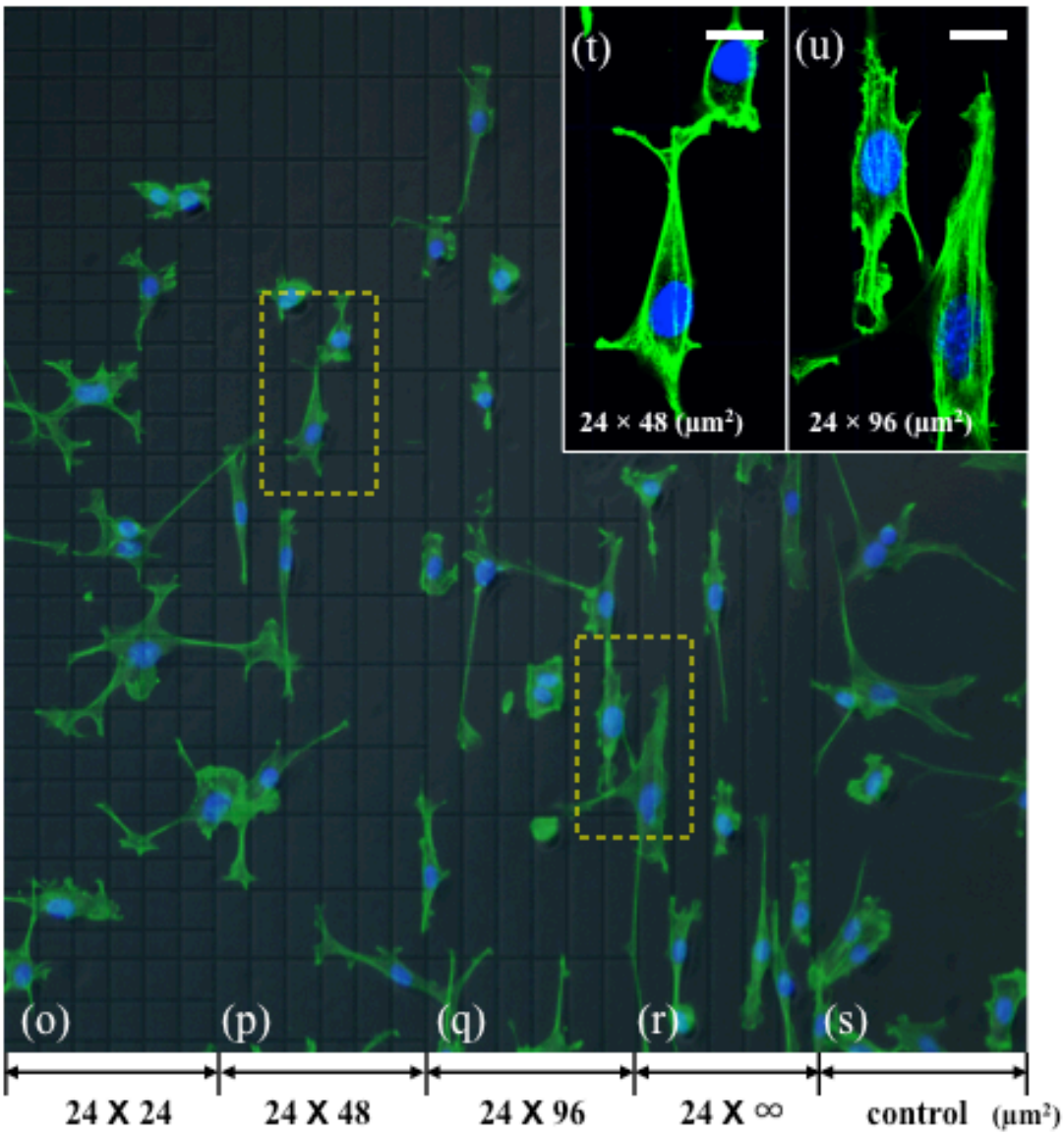

Figure 5.5. continued.

5.5. Cell migration on anisotropic patterns

5.5.1. Migration speed and directionality

We identified qualitatively the difference in cell movement depending on the aspect ratio of grid patterns by applying time-lapse microscopy and image analysis to track the paths of motile individual cells for ~ 7 hours. Continuous paths of 10 typical cells on each grid patterns are displayed in Figure. 5.6. In addition, the average migration velocity in the *x*-direction (V_x) and *y*-direction (V_y), the migration speed (S) and the migration angle (θ), as defined in section 5.3.2, are also shown in Table 5.1 for each experimental case. No specific directionality of cells was observed on a control flat surface (Figure. 5.6(e)), and for the 1:1 cross pattern (data not shown). The measured average migration angles of cells on 3 μm height ridge patterns were plotted for different aspect ratio patterns in Figure. 5.7(a). The directional migration on the 1:2 cross patterns, except for the 24×48 μm^2 pattern, was inconspicuous and rather similar to the migration on flat surface (Figures. 5.6(a-d) and Figure 5.7(a)). The approximately circular distributions in figures 5.6 (a-e) suggest no directional migration. The radius of these distributions represents the extent of migration. While the distributions of cells on 1:2 cross patterns and flat surface are similar, more frequent directional changes were observed on the patterns. On these surfaces, the velocity in the *y*-direction was about 1.3-1.6 times larger than that in the *x*-direction, and the migration angle was about 53°-62°, while the angle of the plane surface was 51.47° (Table 1).

The directionality was more prominent on the 1:4 cross patterns (Figures. 5.6 (f-i) and Figure. 5.7 (a)). The migration angle of the 1:4 cross patterns was 67°-74° (Table 5.1). The smaller the grid area, the higher the value of migration angle calculated for the 1:4 cross and parallel line patterns, in contrast to the 1:2 cross pattern. In addition, the migration angle of 10-μm height pattern was higher than that of the 3-μm height pattern for all aspect ratio cases (Figure. 5.7 (b)). On the parallel strip patterns, the directionality was apparently observed (Figures 5.6 (h-m)). The migration angle of the parallel pattern was 74°-83°, depending on the distance between neighboring ridges and their height. The data suggest that micropatterns can force cell migration specifically in the direction of the longer side of the grid. The directionality depends on the grid aspect ratio and area, as well as the ridge height.

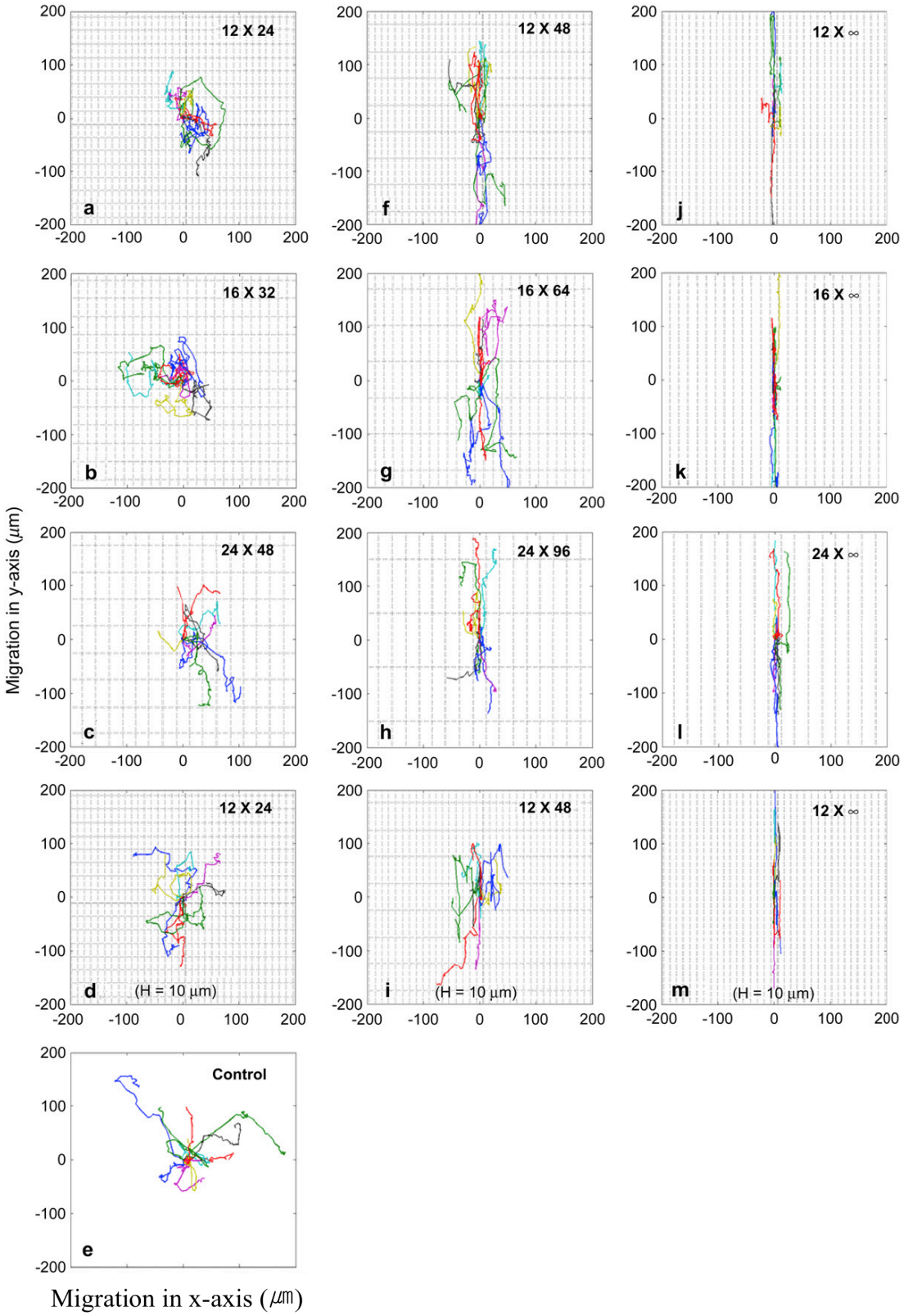

Figure 5.6. Typical cell paths over 7 h depending on various aspect ratio and height of ridge patterns. Data of (d), (i) and (m) were obtained from the patterns which is 10 μm high. The others were obtained from the patterns of 3-μm height.

Table 5.1. Mean velocity of cells migrating in the direction of shorter side ridges, and velocity of cells migrating in the direction of longer side ridges, migration speed, and migration angle on different surfaces ($p < 0.05$).

Pattern size (W × L)	Height (μm)	Migration velocity in x-axis (V_x) (μm/min)	Migration velocity in y-axis (V_y) (μm/min)	Migration speed (μm/min)	Migration angle (°)
12 × 24	3	0.38 ± 0.015	0.58 ± 0.025	0.78 ± 0.027	53.74 ± 1.06
12 × 48	3	0.28 ± 0.014	0.90 ± 0.045	1.01 ± 0.045	68.55 ± 0.93
12 × ∞	3	0.08 ± 0.005	0.56 ± 0.029	0.59 ± 0.029	78.86 ± 0.75
16 × 32	3	0.48 ± 0.021	0.65 ± 0.026	0.90 ± 0.030	54.68 ± 1.06
16 × 64	3	0.31 ± 0.015	0.87 ± 0.038	1.00 ± 0.039	67.49 ± 0.95
16 × ∞	3	0.12 ± 0.007	0.80 ± 0.036	0.84 ± 0.036	77.47 ± 0.77
24 × 48	3	0.26 ± 0.015	0.42 ± 0.024	0.55 ± 0.027	62.39 ± 1.09
24 × 96	3	0.20 ± 0.012	0.49 ± 0.020	0.58 ± 0.022	67.44 ± 1.00
24 × ∞	3	0.12 ± 0.007	0.48 ± 0.027	0.52 ± 0.028	74.29 ± 0.90
12 × 24	10	0.33 ± 0.016	0.46 ± 0.024	0.65 ± 0.026	60.27 ± 1.12
12 × 48	10	0.18 ± 0.013	0.76 ± 0.044	0.83 ± 0.046	74.53 ± 0.89
12 × ∞	10	0.04 ± 0.003	0.60 ± 0.032	0.61 ± 0.032	83.78 ± 0.61
control		0.38 ± 0.019	0.41 ± 0.033	0.63 ± 0.025	51.47 ± 1.15

Data represent mean ± standard error of mean values.

The migration speed is the fastest for the mid-sized cells and grid pattern aspect ratios, while the directionality is proportional to the grid aspect ratio of the patterns. The average migration speed of the cells on the 12 × 24, 12 × 48, 16 × 32, 16 × 64, 16 × ∞ μm^2 patterns with 3-μm height and 12 × 48 μm^2 pattern with 10-μm height was significantly higher than that of the other group including the plane surface (Table 5.1). The average migration speed depending on the pitch (W) and the aspect ratio of grid is shown in Figure. 5.8(a) for 3-μm ridge height. For all gaps (W), the speed of the cells on the 1:4 cross patterns was higher, and on the parallel patterns lower. The speed of the cells on the 12 × 48 and 16 × 64 μm^2 patterns was nearly the same (1.01 and 1.00 μm/min, respectively) and ~1.5 times higher than on the planar surface (0.63 μm/min). In contrast, on the 24 × 96 μm^2 pattern (0.58 μm/min) the speed was lower than on the control planar surface. In most cases, the speed of cells on patterns whose distance between neighboring longer side ridges was 16 μm was observed to be faster than on other patterned substrates. Especially, the speed of the cells on 16-μm pitch parallel pattern (0.84 μm/min) was also significantly higher than that on the planar surface, while the speed of the cells on the other parallel patterns is nearly the same or slower than on the planar surface. From these results, it is noted that both the size of the grid and the distance between neighboring ridges are significant for enhancing cell migration. Moreover, the ridge height is important for cell migration. The average migration speed of the cells on the 3-μm height patterns was generally faster than that on the 10-μm height patterns (Figure. 5.8(b)).

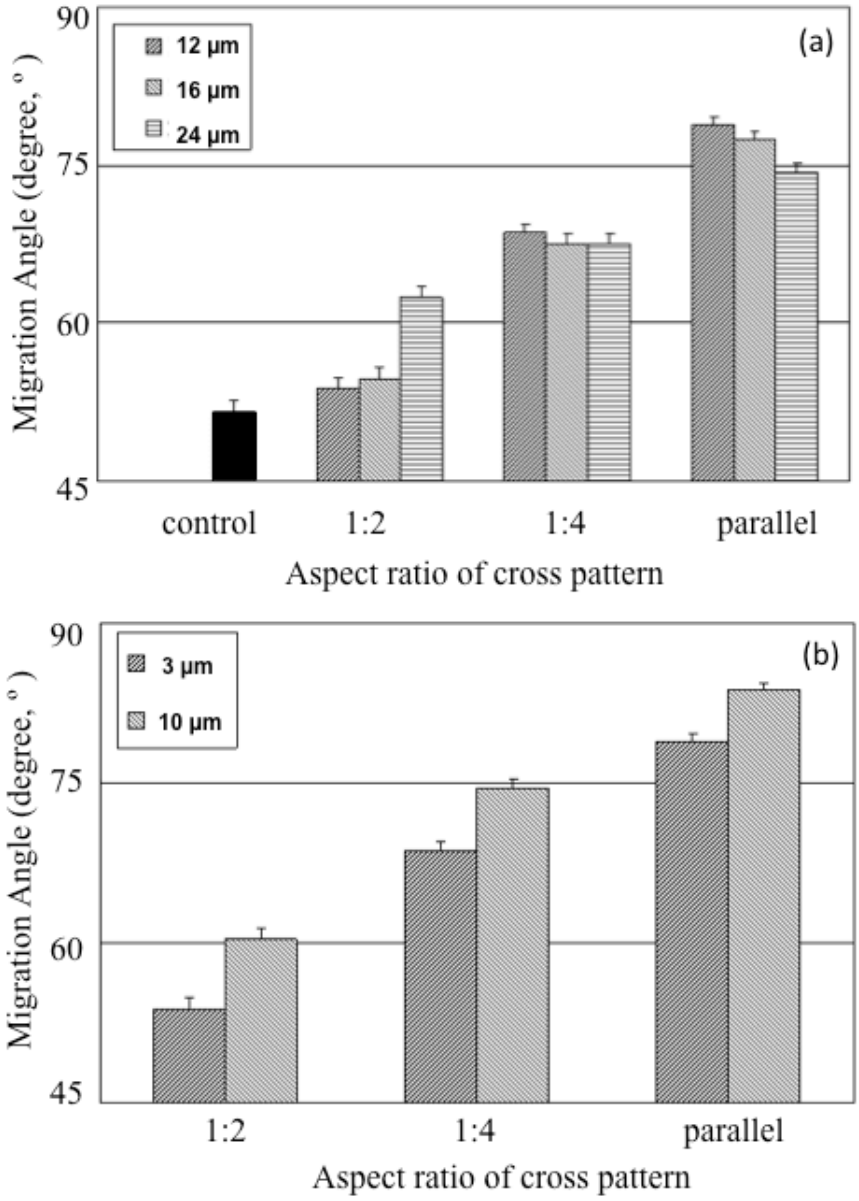

Figure 5.7. The average migration angle of the cells (a) on 3-μm height ridge pattern depending on the pitch (W) of ridges and the aspect ratio of grid and (b) on 12-μm pitch pattern depending on the aspect ratio of grid and the height (H) of ridge. (error bar = standard error of mean)

.

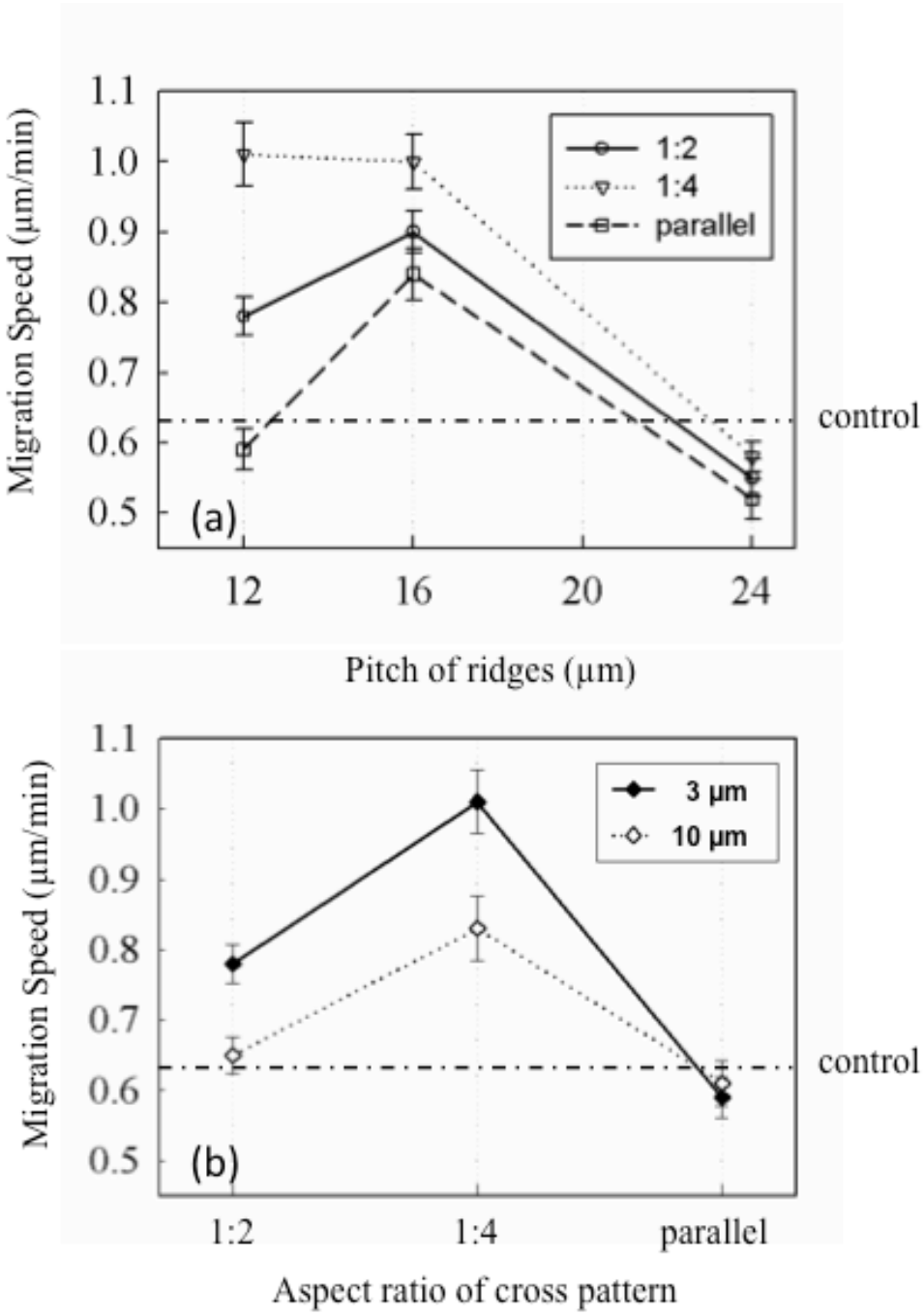

Figure 5.8. The average migration speed of the cells (a) on 3-μm height ridge pattern depending on the pitch (W) of ridges and the aspect ratio of grid and (b) on 12-μm pitch pattern depending on the aspect ratio of grid and the height (H) of ridge (error bar = standard error of mean)

.

5.5.2. Motility coefficient and persistent time

We also determined the motility coefficient (μ) and the persistent time (P) by modeling the cell migration path as a persistent random walk [35, 100, 102]. The motility coefficient does not bear the same meaning as the migration speed, since it quantifies a diffusional representation of the migrating cell distribution (eq. 5.7). Plots of mean squared displacement, $<d^2>$, were obtained by using overlapping time interval sample method with the experiment data as described in section 5.3.3. The plots for each substrate were shown in Figure 5.9. The values of P and μ reported in the study are calculated from the experimental data for time up to $t_{max}/3$ (one third of the total duration of the migration path) since the true path of cell movement cannot be observed at longer times as can be seen in Figure 5.9 (a),(c),(e) and (g)) [35, 103]. The parameters, μ and P, are plotted in Figure 5.10 for cells on surfaces with various aspect ratio and height. In contrast to the migration speed, the motility of cells on parallel line patterns was highest (Figure 5.10(a)). This is because the motility is also related to the persistent time that is significantly higher on the parallel line patterns (Figure 5.10(c)). Although the cell motility on 1:4 patterns was substantially higher than the control value, it fell below this reference for the 1:2 patterns. The cell motility was the greatest at intermediate spacing (W = 16 µm), exhibiting the same trend as the migration speed. The motility also depended on the ridge height and was higher on the 3-µm versus the 10-µm ridges (Figure 5.10(b)). The difference was more pronounced for the parallel line patterns.

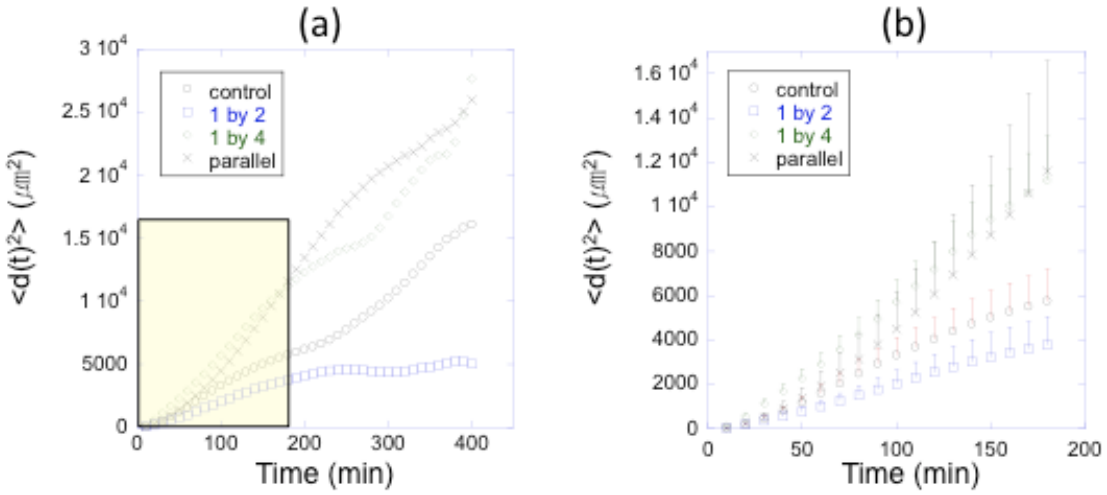

Figure 5.9. Plots of the mean-squared displacement as a function of time for (a-b) 12-, (c-d) 16- and (e-f) 24-µm spacing with 3-µm height patterns and (g-h) 12-µm spacing and 10-µm height pattern. Plots of (a,c,e,g) are the displacement data for time up to t_{max}. Plots of (b,d,f,h) are displacement data for time up to $t_{max}/3$ that were used for calculation of P and µ.

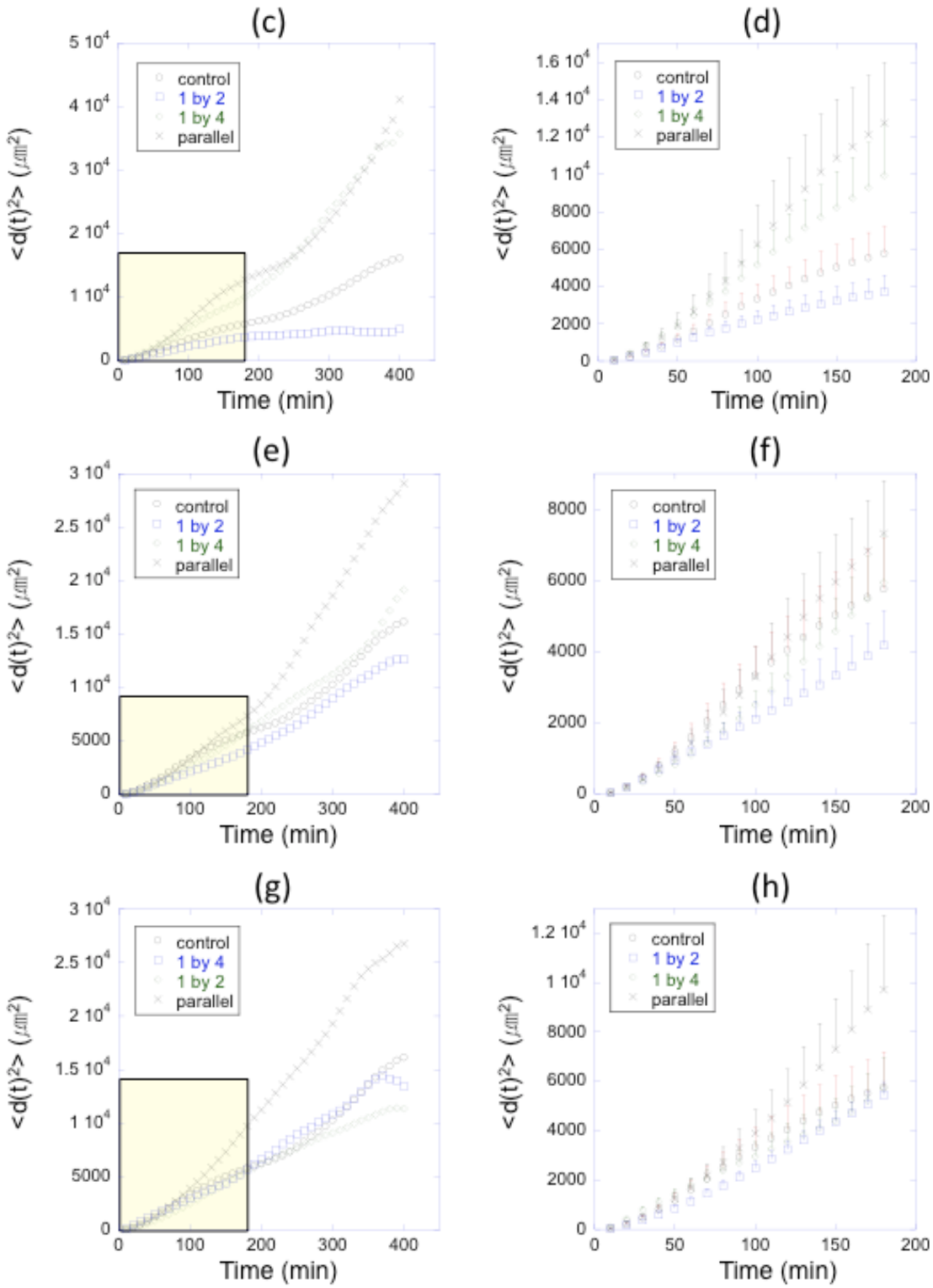

Figure 5.9. continued.

.

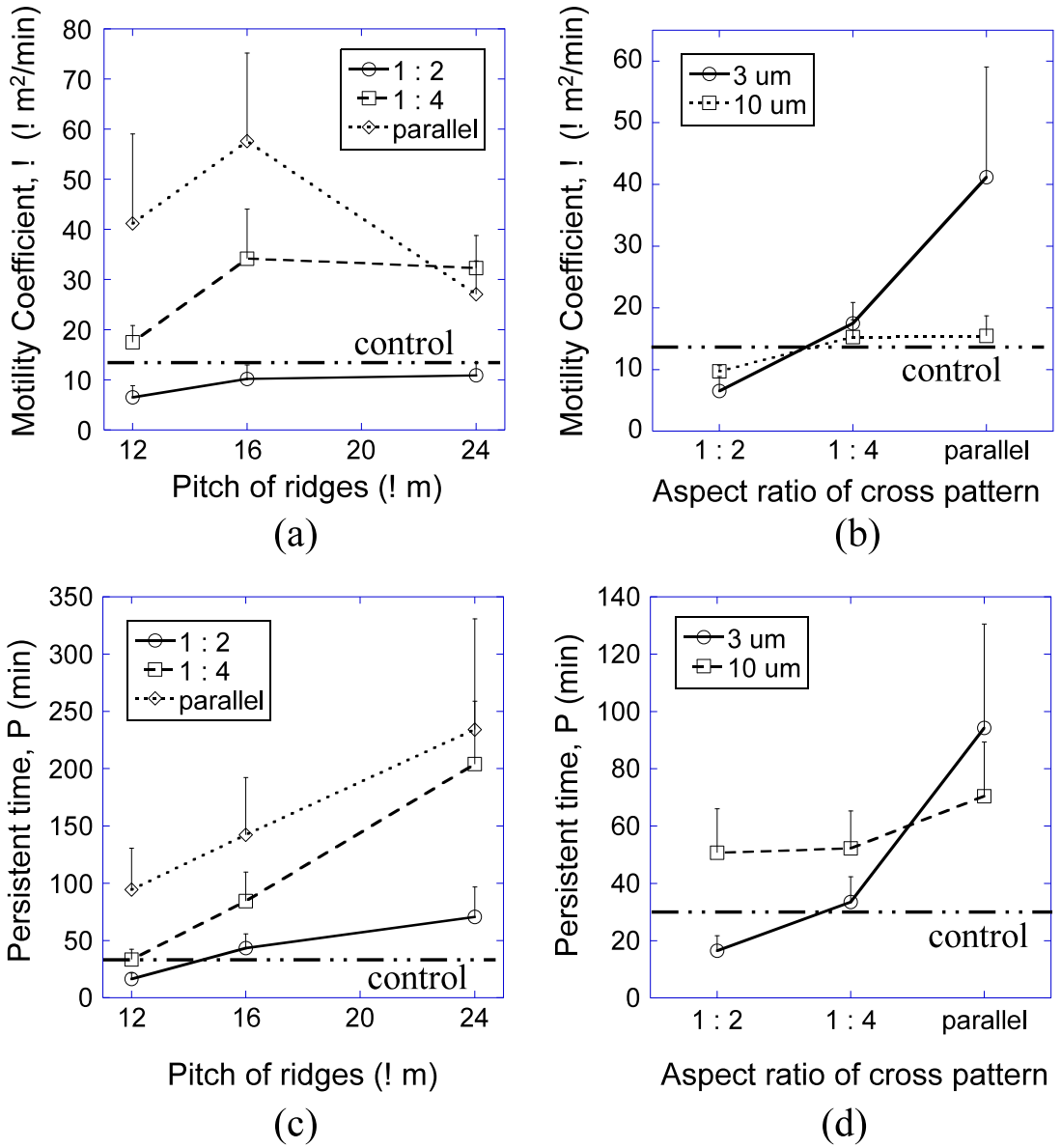

Figure 5.10. Motility coefficient (μ) and persistent time (P) for the movement of NIH3T3 cells on patterned surfaces with various aspect ratio of grid and height of ridges. (error bar = standard error of mean)

The persistent time was calculated to estimate the directional characteristic of cell movement (Figure 5.10(c)). As cell migrated without shifting direction, the persistent time increased. Accordingly, the persistent time displays a similar tendency with the migration angle as they both increased with increasing pattern aspect ratio (Figure 5.7 and Figure 5.10). The persistent time also increased as the distance (W) increased, while no apparent tendency was extracted for the migration angle. In addition, there was no significant difference of the persistent time between 1:2 patterns and the control plane surface. Longer persistent times for cross patterns and shorter times for parallel patterns were calculated (Figure 5.10(d)).

5.6. Topographical effect on cell motility

Mai et al. fabricated topographically structured surfaces to exert multi-directional stimulations in the form of contact guidance to single cells [41]. They reported that cells on rectangular grids were elongated and migrated specifically in the direction of the longer side of the grid. Our results provide enhanced evidence in support of their conclusion that cells can sense and compare contact guidance from multi directions, and then follow the dominant guidance. On the 1:2 cross patterned surface, cell alignment and directionality of migration along the longer side ridges were not evident. Cell alignment and migration directionality became more apparent on the 1:4 cross patterns and the parallel patterns. The ability of structures to align and direct cells weakened as the grid size of cross patterns and the distance across neighboring ridges comprising parallel patterns increased. Similar observations had been made by Li et al. who studied endothelial cell migration on 15-μm, 30-μm and 60-μm strip patterns, and reported that the cells on 15-μm strips were completely aligned in the direction of the strip [104].

The micron scale cross patterns in this study can enhance cell motility as well as orientation and directionality of cell migration. The cells on 12 × 48 and 16 × 64 patterns attained highest migration speed and stronger migration directionality. In addition, the cells on the patterns having 16-μm pitch between neighboring longer side ridges migrate faster compared to other patterns of the same grid aspect ratio. These results demonstrate that cell motility depends significantly on the pattern size. Li et al. reported that endothelial cells on 15-μm strip patterns migrated faster than cells on 30-μm and 60-μm strip patterns [104]. Corroborating their results is the present finding that only 16-μm pitch strip patterns can enhance the cell motility, while the migration speed of cells on 12- and 24-μm pitch strip patterns is lower than on the planar surface. The 16-μm pitch is very close to the diameter of suspended NIH3T3 cells which was calculated at 16.19 ± 2 μm. The patterns exhibit "contact enhancement" and "restriction" functionalities that can alter cell motility [102]. On 24-μm pitch strip patterns, cells tend to attach to one side of ridges while on 12-μm pitch strip patterns, they squeeze themselves to fit between the ridges, hence restricting migration. Therefore, the intermediate spacing of 16 μm works best for enhancing cell movement since both side ridges exert contact guidance without squeezing the cells.

The most interesting observation in this study is that the cross patterns can enhance the migration speed of the cells. The migration of cells has been described as a multistep process. For cells to move forward, actin polymerization at the leading edge pushes the plasma membrane forward and forms new regions of actin cortex. New points of anchorage are formed between the actin filaments and the surface where the cell is migrating. Contraction at the rear of the cell then draws the body of the cell forward. Old anchorage points are released at the back as the cell crawls forward. This multistep process is repeated [26]. The surface chemistry and topography have a significant influence on motility, as Dimilla *et al.* reported that initial cell-substratum attachment strength is a central variable governing cell migration speed and maximal speed can be obtained by cells moving on surfaces offering intermediate attachment strength [35]. This response had been interpreted via mathematical arguments by Palecek et al. who proposed a model integrating biophysical and biochemical interactions between integrins, the cytoskeleton, as well as matrix affected rear retraction and linkage dissociation mechanisms [105]. They showed that cell detachment is extremely rapid, dominated by integrin extracellular-matrix dissociation, at low adhesiveness. In contrast, detachment is much slower and dominated by integrin-cytoskeleton dissociation, at high adhesiveness. This behavior has implications on overall cell migration speed. In this study, the fibroblasts on smaller grid size cross patterns than individual cell size were able to bridge between ridges, or ridges and grooves, as the osteoblasts in Hamilton et al.'s study [96]. The ridges of small width, in the range of 1-2 μm reduce contact area on ridge side. The bridging-like shape of cells and respective small attaching area on ridges reduce adhesiveness of the cells to the ridge/groove surface, resulting in enhancing cell migration speed. This hypothesis is supported by the experimental result that cells on the 10-μm height patterns migrate more slowly than cells on the 3-μm height patterns, although the two different height patterns have the same aspect ratio and grid size. Cells may twist themselves more to extend their protrusions and suspend on the higher ridges since the 10-μm height exceeds the cell thickness. Consequently, the higher ridges may result in weakening the cell adhesion force. However, the higher ridges can enhance cell directionality via stronger contact guidance. In addition to this mechanism, the longer side ridges of the cross patterns play a role in contact guidance along the ridges and the shorter side ridges of the cross patterns affect the formation of anchorage points that presumably can enhance cell migration speed. However, the cell positioning varies depending on pattern size and height. Cells are placed between longer and shorter side ridges of cross patterns when seeded on larger size patterns, whereas they bridge over cross pattern ridges when seeded on smaller size patterns. When the space of the groove of cross patterns is large enough to accommodate cells, the ridges do not provide contact guidance anymore. In this case, the shorter side ridges act as barriers inhibiting cell migration. When the cross pattern groove space is too small, the contact guidance effect is reduced. Therefore, it is noted that the overall pattern configuration, such as height and width of ridge, aspect ratio of grid, and size of grid, is important for deciding the cell movement. We also confirmed that the cross patterns can be more effective in increasing cell migration speed than parallel line patterns.

5.7. Conclusion

In this chapter, we examined the effect of different aspect ratio and size of anisotropic cross patterns and parallel line patterns, fabricated by using two-photon induced polymerization, on cell morphology and motility. These topographical patterns influenced cell morphology and motility multidirectionally, providing contact guidance with continual stimulation. This may be of help for the long-term monitoring of cell behavior. We found that cells cultured on parallel line patterns and 1:4 cross patterns can be aligned and migrate along the parallel ridges or the longer side ridges. Such structures provide contact guidance for cell morphology and movement. In addition, the cell migration speed can be enhanced by the cross patterns, depending on the aspect ratio of grid, the grid size, and the ridge height since the shorter side ridges supply anchorage points. Our results demonstrate that topographical surfaces with various aspect ratios of grid patterns can be used to control cells by stimulating cell attachment and protrusion, resulting in cell alignment, direction of migration, and motility. These investigations suggest a useful means for understanding interaction of cells to the extracellular matrix which forms a meshwork of interlinked fibers and contributing to the design of implant surface engineered in order to enhance or inhibit cell movement.

Chapter 6

Directional cell migration on nanoscale patterned surface

Microscale topographical effect on cell behaviors, such as alignment and migration has been discussed in the previous chapters. Topographical cues on the micrometer length scale are a powerful tool to control cell shape. However, such studies have been limited by the inability to independently control the input into the cell via focal contacts. This limitation has prevented analysis of the effect of ligand type, density, and nanoscale distribution of focal assemblies in contolling cell fate. In this chapter, cell adhesive and migrational behaviors on nanoscale patterned surface are demonstrated by both of chemical and topographical cues.

6.1. Introduction to nanopatternings for cell control

Normal eukaryote cells adhere to surfaces and form anchorages of a variety of forms in different tissues of nanoscale, microscale, and local mesoscale patterns. In particular, the nanopatterning has received much attention since most of surfaces in or on the natural tissues are in nanometer length scale. Nanoscale modifications in topographical and chemical patterns elicit diverse cell behavior, ranging from changes in cell adhesion, orientation, motility, cytoskeletal organization, and gene expression [106]. Due to the advantages that can control spatial arrangement of biomolecules and independently regulate the input into the cell via the focal adhesions, surface patterning in nanometer length scale is critical for decoupling the effects of cell size, shape, focal adhesion clustering, and ligand input for cell fate and functions. Thus, not only the scale of patterns but also the type of patterns, e.g. nanograting, nanopost, nanopit and

nanoisland has different effects on cell behaviors. Even nanofeatures of different symmetry or with different disorder have a different effect on cell behavior [6].

Initial response of cells to the nanopatterns is changing their geometry. Many cell types cultured on nanograting topographical patterns are aligned and elongated following the direction of the grating axis and exhibit biased migration in the direction of the grating axis and increased migration speed [107]. It has been reported that topographical patterns of nanoposts and nanopits reduce cellular spreading and adhesion formation [107, 108]. The nanoscale topographical patterns also can potentially be utilized for gene expression and to direct differentiation. It was reported that fibronectin mRNA levels in human fibroblast were increased and the stability was also altered by nanoscale surface topography [109]. The enhanced stem cell differentiation into osteoblasts by the nanopits in the absence of chemical treatment was shown by Dalby et al [6]. By the nanoscale chemical patterning, arrays of cellular adhesion proteins can be constructed to directly control cell adhesion sites, i.e. focal adhesions, resulting in cell adhesion and geometry [110]. Recent advances in nanofabrication methods have led to creating superb resolution of the patterns, allowing more precise quantitative experimentation. Those nanofabrication techniques are briefly reviewed in chapter 2.3.

6.2. Laser ablation lithography

Nanoscale topographical and chemical patterns in this chapter are fabricated by nonlinear absorption and optical breakdown of dielectric materials with femtosecond laser pulses. Basic mechanisms and theories are discussed in chapter 3.1. The intense femtosecond laser pulses can induce damage in transparent dielectrics by nonlinear absorption processes such as multiphoton initiated avalanche ionization [48]. In contrast to material modification by nanosecond or longer laser pulses, there is no heat exchange during the femtosecond laser pulse irradiation. This results in minimizing thermal stress and collateral damage. Therefore, the femtosecond laser induced ablation process is stable and reproducible [52, 59]. In addition, due to nonlinear optical characteristics and the Gaussian beam profile of the femtosecond laser, structures smaller than the processing beam spot size can be fabricated by precisely adjusting the pulse energy close to the ablation threshold [60, 111]. Since the laser interaction with dielectric materials is strongly nonlinear, the femtosecond laser can realize ablative features of subwavelength resolution on quartz and polymers [57, 60, 62]. Therefore, multiphoton photolithography provides high-resolution material processing without requiring photomasks and chemical developers [57, 58].

6.2.1. Experimental setup

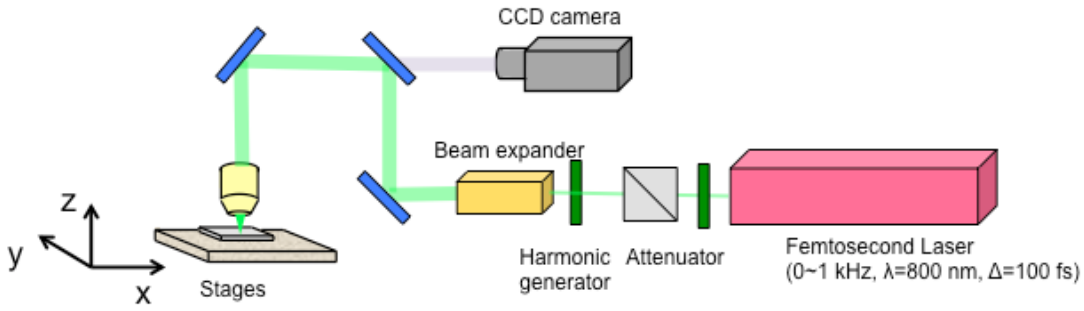

Figure 6.1. Schematic representation of the experimental setup used for laser ablation nanofabrication.

We used a Ti:Sapphire regeneration amplifier system (*Spitfire*, Spectra-physics). The *Spitfire* system amplifies individual laser pulses that are selected from a stream of pulses and produced by a separate, mode-locked Ti:sapphire femtosecond laser (*Tsunami*, Spectra-physics). Typically, an input pulse with an energy of only a few nanojoules can be amplified to about 1 millijoule. The *Spitfire* amplifier contains the optics and opto-mechanical devices for stretching, selecting, amplifying and compressing pulses from the seed laser. A controller (*SDGII*, Spectra-physics) provides the synchronization and control needed to select and capture individual pulses from the train of stretched seed pulses and direct them into the amplifier. The selected, stretched pulses then pass multiple times through the regenerative amplifier. Once the pulses are amplified, the controller provides the timing control to direct the amplified pulses into the compressor. The compressor shortens the amplified pulses close to their original duration using a second grating/mirror combination. The pulses are then emitted from the *Spitfire*. Triggering a single pulse and some specific repetition rate (up to 1 kHz) can be available by using the controller.

The ablation experiments were performed in ambient air with the amplified Ti:Al_2O_3 femtosecond laser of about 100 fs pulse length [at full width half maximum (FWHM)] and wavelength of ~400 nm that was obtained after being frequency-doubled from fundamental ~800 nm wavelength laser beam by a nonlinear crystal. The experimental apparatus is shown in Figure. 6.1. The fluence was adjusted with an attenuator including a half wave plate ($\lambda/2$) and a polarizing beam splitter (PBS). As the laser pulse energy required to ablate high- resolution features was extremely low, a neutral density (ND) filter was inserted into the beam path. To generate user-designed patterns, samples were loaded on a precise three-dimensional motorized stage with a synchronized laser firing system controlled by a programmable PC. The scanning stage (ANT130, Aerotech Inc.) is driven by its own driver (NDrive ML) and control software (A3200, Aerotech Inc.) controlled by PC. The driver has digital input and output ports that can generate TTL signal configured by the software. One way to synchronize the laser firing and scanning stage is to use the output signal from the driver to trigger the laser controller (*SDGII*) for directing the single pulse out of the amplifier (*Spitfire*). The other way is to fix the specific repetition rate of the laser pulses and to control the mechanical shutter by the output signal from the driver. For example, patterns with 1-μm spacing can be achievable with 1 mm/s scanning speed and 1 kHz laser pulses. The

sample was precisely aligned perpendicular to the incident laser beam by adjusting the tilting angle of the sample. To investigate the influence of beam spot size and film thickness, long working distance objective lenses with three different numerical aperture sizes were used: 10x Mitutoyo M Plan Apo (N.A.= 0.28), 50x Mitutoyo M Plan Apo (N.A.= 0.55) and 100x Nikon CFI 60 LU Plan Epi ELWD Infinity-Corrected (N.A.= 0.8). The pulse energy was measured by a pyroelectric energy meter (Molectron J5-09) placed between the attenuator and the ND filter. Before the ablation experiments, the output energy from each o bjective lens and energy at the above-mentioned position were measured separately to yield the attenuation ratios. These attenuation ratios were utilized to obtain the pulse energies in the course of the nanoablation experiment that were too low to measure via the energy meter. Using the computer-controlled system, single pulse ablation of bare quartz only and poly(ethylene glycol) (PEG) films of various thicknesses on quartz was performed. The ablation craters were examined by AFM (Nanoscope IIIa, Veeco) with high aspect ratio tips (Nanosensors, AR5-NCHR, Aspect ratio ≥ 5:1).

For the topographical patterns, fused silica (fused quartz) glass was used. The fused quartz glass is a wide band gap dielectric material, which has high thermal and chemical stability, low thermal conductivity and high transmission efficiency in optical detection. Square glass pieces with 8 mm by 8mm dimensions were prepared for the experiment by dicing a 0.5-mm thick 4-inch quartz glass wafer. The glass substrates were cleaned ultrasonically with Acetone before and after the ablation experiments.

For the chemical patterning, PEG brush layers were used and chemical compositions are shown in Figure. 6.2. Surface initiated atom transfer radical polymerization (SI-ATRP) was used to generate PEG brush layer that has been shown to eliminate non-specific protein adsorption, and offers a number of advantageous properties for biotechnological applications [112]. The PEG brush layers were synthesized by reacting a surface grafted with the SI-ATRP silane with solution containing PEG monomethacrylate monomer (PolySciences) in a deoxygenated environment. The SI-ATRP synthesis was carried out as described previously [112]. Briefly, 1.0 mmol copper(I) bromide, 2.0 mmol bipyridine, 0.3 mmol copper(II) bromide, and 25 mmol of the monomer poly(ethylene glycol) monomethyacrylate (side chain MW=200) were dissolved in 12 mL of methanol and 3mL of degassed water. The dark red solution was bubbled with nitrogen for 30 minutes and sonicated until all materials were dissolved, before being poured over the silanated samples. The reaction was

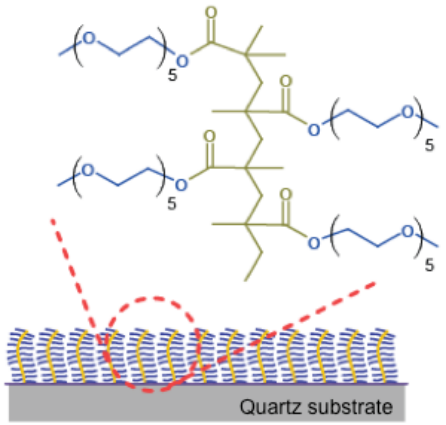

Figure 6.2. Schematic of poly(ethylene glycol) brush layers on quartz glass.

maintained for various times to yield the desired thicknesses, under nitrogen flow before the samples were removed, rinsed copiously with methanol and dried under a nitrogen stream.

6.2.2. Polymer thin film ablation

Subwavelength-sized ablated craters on the PEG film fabricated by single laser pulses at various energies via the 100x objective are shown in Figure 6.3. The film thickness is about 15 nm. For pulse energies of 4 and 4.5 nJ, the PEG film was only taken off from the quartz substrate with no damage to the substrate. In contrast, ablation progressed to the quartz substrate at the 5 nJ pulse energy. It can be noted that the ablation threshold of the quartz is higher than that of the PEG film. Therefore, ablated PEG pit arrays without incurring damage to the quartz substrate can be fabricated. In particular, the smallest ablated pit diameter was ~150 nm when the film was taken off clearly. For 10-nm thick film and the other objectives (50x and 10x), the smallest diameters of the ablated pits were ~250 nm and ~1000 nm, respectively. The smallest feature diameters are half or less of the $1/e^2$ laser spot size.

The $1/e^2$ laser spot radius (w_0) was calculated using the relation between Gaussian spatial beam profile and radial distribution of the laser fluence [113, 114].

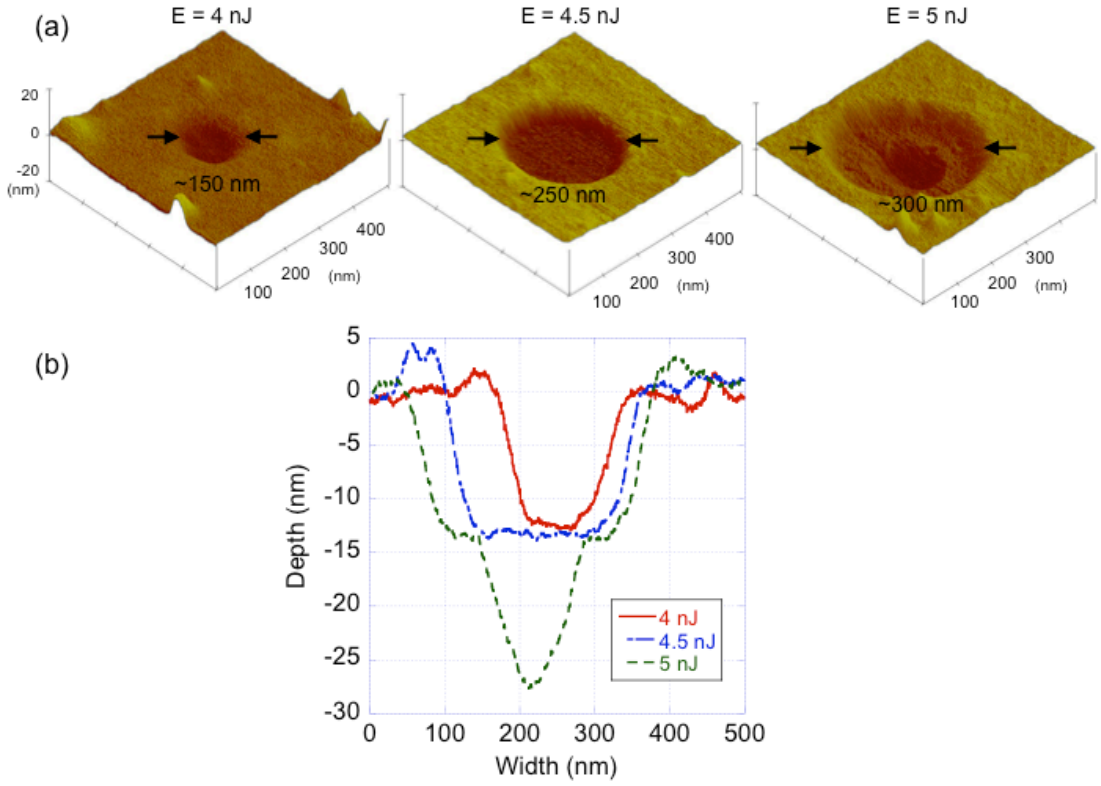

Figure 6.3. Single-shot laser ablated craters using an atomic force microscope. (a) Three-dimensional AFM images of craters with three different pulse energies. (b) Cross-section profiles of the ablated craters.

$$D^2 = 2w_0^2 \ln\left(\frac{\phi_0}{\phi_{th}}\right) \tag{6.1}$$

where D is a diameter of ablated features, w_0 is $1/e^2$ laser beam spot radius, and ϕ_0 is the average laser fluence that is defined as the pulse energy per unit irradiated area:

$$\phi_0 = \frac{E_{pulse}}{\pi w_0^2} \tag{6.2}$$

where E_{pulse} is a total pulse energy. The ablation threshold fluence ϕ_{th} was defined as the fluence for which the linear fit crosses D^2=0. This square diameter-regression technique provides a convenient method for determining the ablation threshold and the Gaussian laser beam spot diameter [114, 115]. It is particularly useful for thin film ablation study since the direct ablation depth measurement to determine ablation threshold [111] cannot be implemented when the ablation depth exceeds the film thickness. Figure 6.4 shows the linear relation between the squared ablated spot diameter and the logarithm of the average laser fluence for three films of different thickness and bare quartz. The ablation thresholds for PEG films are 0.62~0.67 J/cm^2 with 10x objective, 0.96~1.00 J/cm^2 with 50x objective, and 0.82~0.88 J/cm^2 with 100x objective. For the same objective lens, the film thickness does not obviously influence the ablation threshold. In thermal diffusion based ablation of photosensitive polymer, the ablation threshold fluence increases dramatically with decreasing film thickness [116]. In contrast, our experimental results suggest a nonthermal ablation process. Clean ablation contours were fabricated by the femtosecond laser as shown in Figure 6.3. The material damage is confined within a small region at the peak of the Gaussian laser beam distribution, where the intensity suffices to trigger multiphoton initiated avalanche ionization. Due to short pulse duration that should be below lattice coupling time (estimated of the order of 10 ps), the heat affected zone is minimized, resulting in no lateral damage. Furthermore, the ablation threshold fluence is independent of the film thickness. The ablation thresholds for quartz are 1.18 (10x), 1.45 (50x) and 1.48 (100x) J/cm^2, respectively, and about 1.5 times higher than the respective threshold of PEG film. Therefore, clear PEG ablated pit arrays can be fabricated without damaging the underlying quartz substrate.

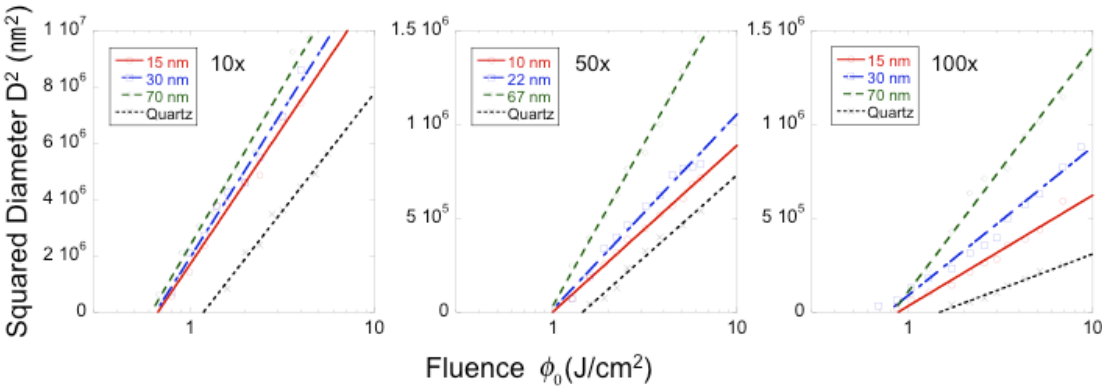

Figure 6.4. The squared diameters of the ablated craters on three different thickness films and a quartz as a function of the incident laser fluence for three different magnification objective lenses.

6.2.3. Fused quartz ablation

The cross-sectional profiles of the ablated craters on the glass fabricated by single laser pulses at various energies via the 50x and 100x objective are shown in Figure 6.5 and the corresponding top view of the features by 100x objective is shown in Figure 6.6. The ablation occurs by nonlinear ionization mechanism (multiphoton absorption, avalanche and tunneling) that is discussed in chapter 3. There is no trace of the molten materials around the periphery of the crater since the thermal process is minimized over the short pulse regime. Evidently, different aspect ratio features can be achieved, i.e. features with the same diameter but different depth, by different N.A. objective lenses. Due to the attributes and mechanisms of the femtosecond laser processing with dielectric materials, patterns with different dimension/aspect ratio nanopits can be achieved for the cell migration control.

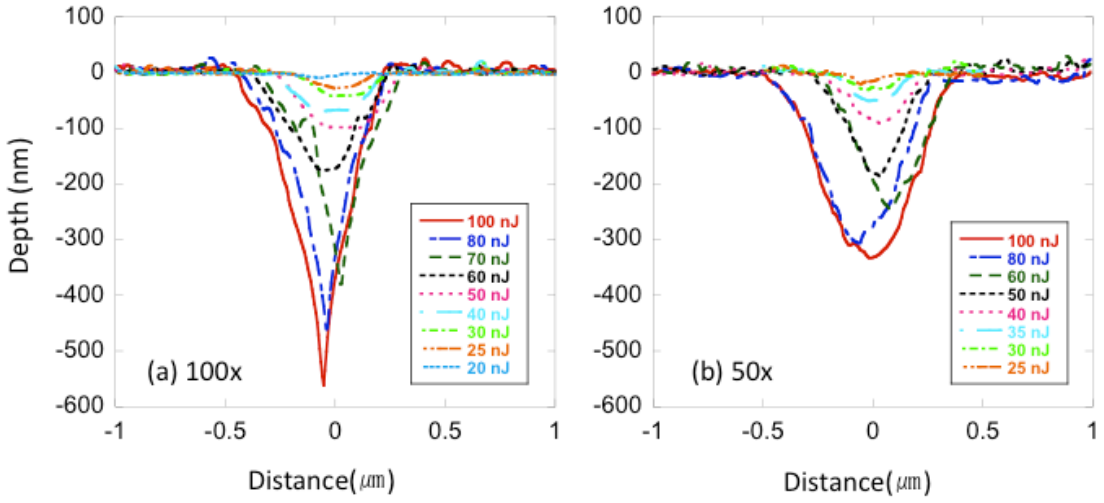

Figure 6.5. Cross-sectional profile at the center-line of the ablated craters by the 100x objective (a) and the 50x objective (b).

6.3. Cell migration on nanoscale patterns

Sub-micrometer scale ablated features were patterned to stimulate cells and guide their migration. In order for cells to sense at least two different regimes of the patterns, spacing gradient patterns were designed maintaining constant ratio of texture versus plane ((area of a crater (A_C))/(area of a unit patterned surface (A_P)) in Figure 6.18) or chemical density within 20 x 20 μm^2 area. The design concept and actual spacing dimensions of the patterned sample are shown in Figure 6.7 and 6.8, respectively.

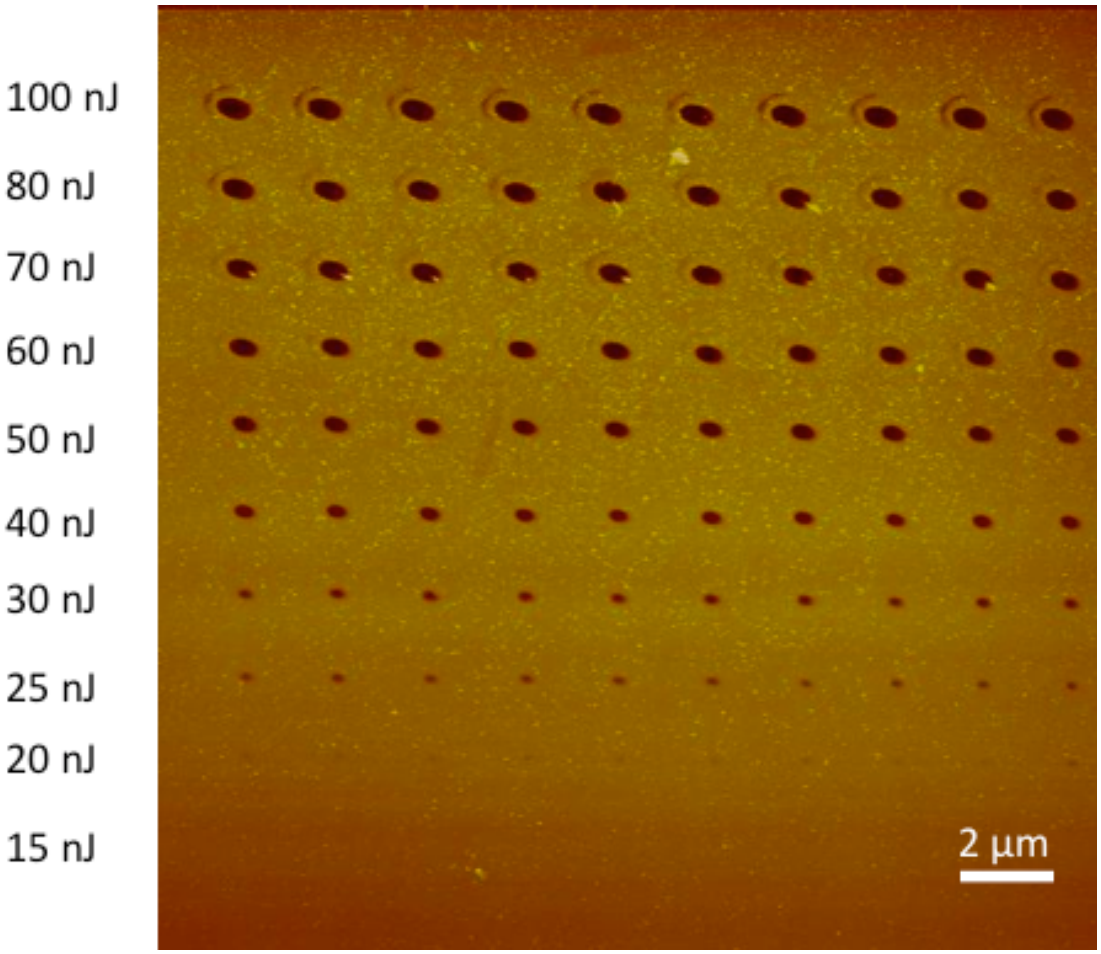

Figure 6.6. AFM images of the ablated craters by the 100x objective.

Figure 6.7. Schematic of the pattern design to control cell migration.

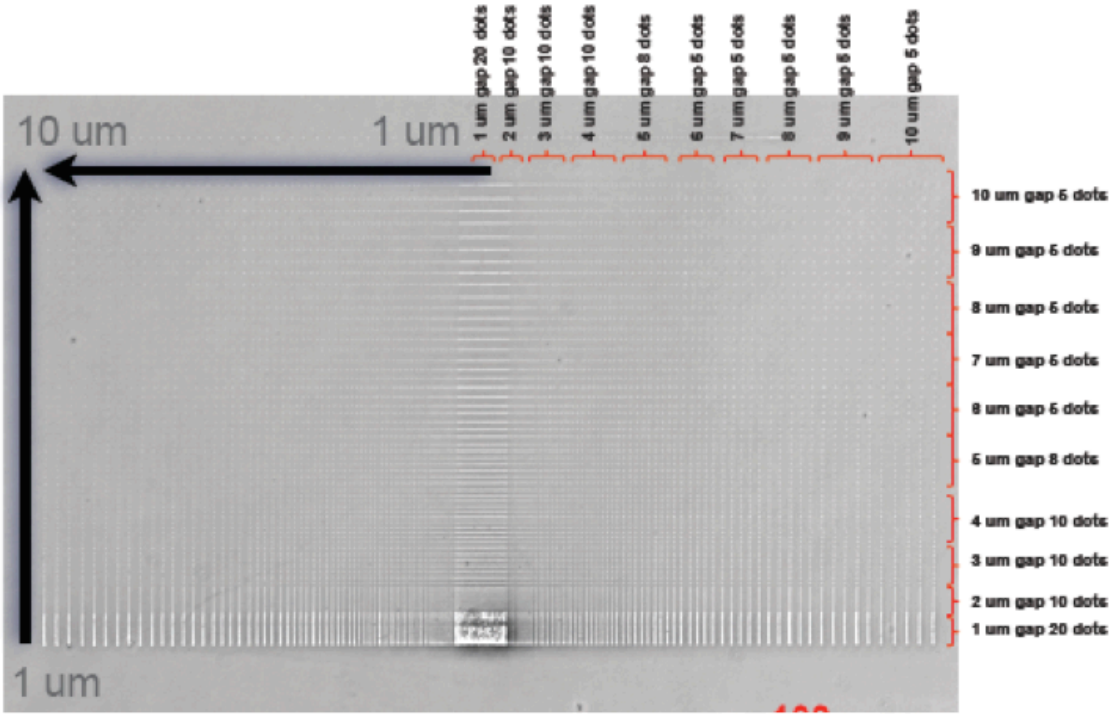

Figure 6.8. Phase-constrast image of the patterned sample showing dimensions.

6.3.1. Cell culturing and imaging

NIH3T3 cells were maintained in Dulbecco's Modified Eagle Medium (Gibco Invitrogen), 10% fetal bovine serum (FBS) (Gibco Invitrogen) and 100 units/ml penicillin (Gibco Invitrogen) in 75-cm^2 culturing flask (Corning) at 37 °C and 5% CO_2 culture incubator. Before experimentation, confluent cells were detached from the flask by 0.05% Trypsin-EDTA (Gibco Invitrogen) and seeded onto the patterned substrate in sterile polystyrene well plates with CO_2-independent media (Gibco Invitrogen), 10% FBS, 100 units/ml penicillin, and 1% GlutaMAX (Gibco Invitrogen) and placed on an inverted fluorescence microscope (IX71, Olympus) that was covered by a chamber to maintain temperature and humidity. Phase-contrast images were taken every 5 minutes with a digital CCD camera (Retiga 2000R cooled, Qimaging) for about 2-3 days.

6.3.2. Directional migration on ECM density gradient

To observe the cell migration on the chemically patterned surface, nanopits with 500 nm in diameter and 60 nm in depth were patterned exposing the quartz substrate via the 15-nm thick PEG film with damaging of 45-nm deep craters into the bottom substrate. The PEG layer has been shown to eliminate non-specific protein adsorption, allowing the cell adhesion onto the exposed patterns only. Ablated patterns of the same diameter but

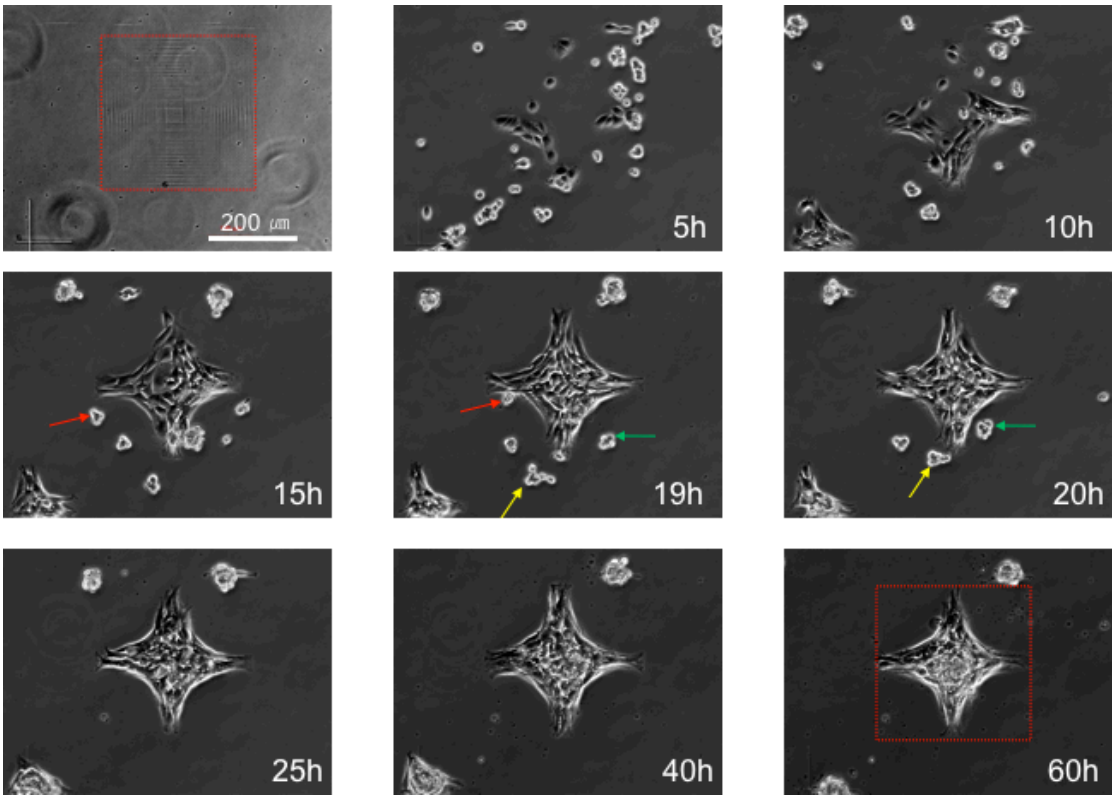

Figure 6.9. Time-lapse microscope images of NIH3T3 migration on chemically patterned surface.

different spacing can generate a gradient of cell adhesion ligand density. The time-lapse microscope images are shown in Figure 6.9. When cells settled down at the surface, they tried to form focal adhesions. The cells on the higher ligand density area could easily attach to the surface and form anchorages, while the cells on lower ligand density area could not attach easily or spread and migrate towards the higher density region. For example, cells marked by a red arrow at 15h were observed on the higher density region at 19h. About 25h after cell seeding, most cells on plane PEG film disappeared and cells only on the exposed area were observed. They formed a cluster on the high ligand density region and kept proliferating. As a result of that, increased cell density at the center was observed at 60h.

6.3.3. Cell adhesion on topographical patterns of nanopits

Prior to discussing cell migration on the topographical patterned surface, cell adhesion on the nanopit patterns is discussed in this section. It is known that the nanoscale patterns or surface roughness can reduce cell adhesion. Kunzler et al. showed different cell morphology depending on the surface roughness controlled by adjusting nanoparticle density [117]. They reported that the osteoblasts were small in size with long fiamentous extensions and did not exhibit pronounced focal adhesions on the area of high

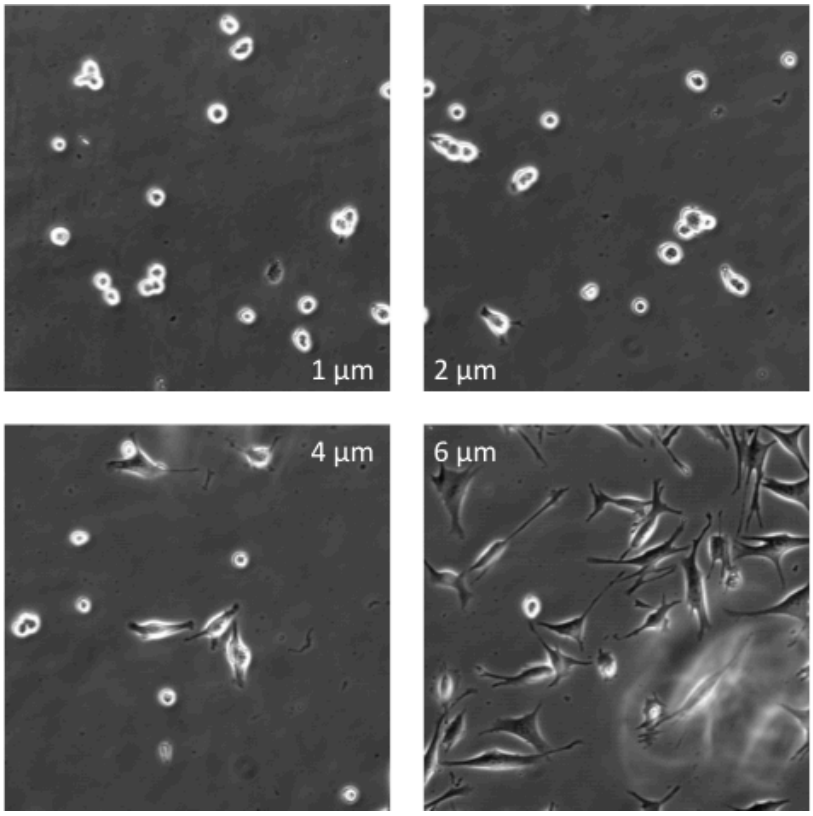

Figure 6.10. Phase-contrast images of cell morphology on isometric patterns of nanopits (600 µm in diameter and 800 µm in depth) with different crater surface density (1, 2, 4 and 6 µm).

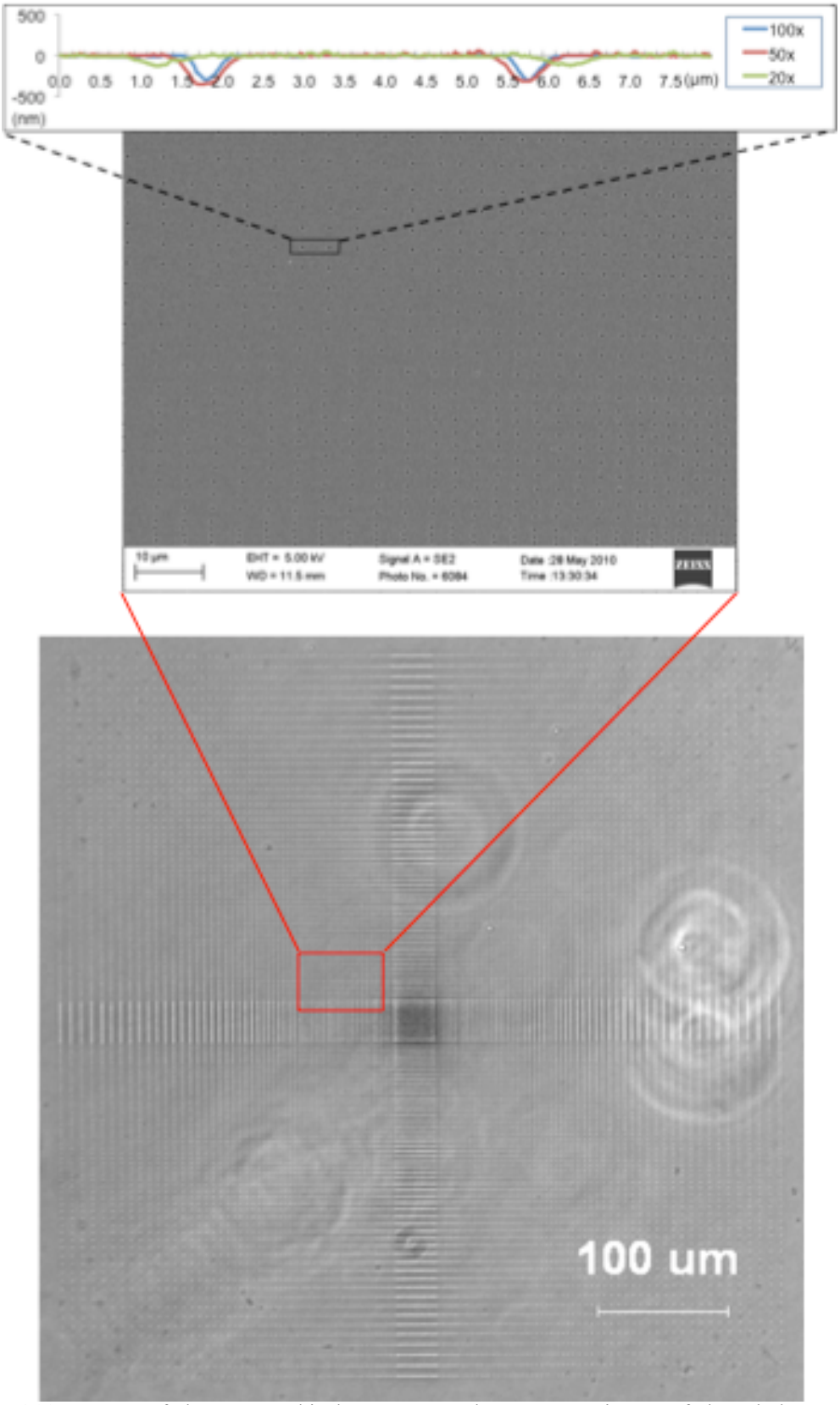

Figure 6.11. Images of the topographical patterns: a phase-contrast image of the whole patterned surface, a SEM image of the magnified image and an AFM scanned cross-sectional image for three different dimension nanopits fabricated by the 100x, 50x and 20x objective lenses.

density of nanoparticles. With decreasing particle density, cells spread more and formed an actin network with distinctive focal adhesions. In this study, fibroblasts also showed similar morphological characteristics, which is shown in Figure 6.10. The images were taken 24h after the cell seeding.

6.3.3. Directional migration on topographical gradient

For the cell migration study, six different dimension nanopit-patterns were fabricated by using 100x, 50x and 20x objective lenses summarized in table 6.1. The angle of cross-section is defined as $\tan^{-1}(2 \times \text{depth/diameter})$. Typical patterned substrate is shown in Figure 6.11. The cross section profile scanned by AFM shows different aspect ratios of three nanopit patterns (600/350 nm, 1000/350 nm, 1000/100 nm in diameter/depth) fabricated by the 100x, 50x and 20x objective lenses, respectively.

Table 6.1. Dimension of nanopits for topographical patterns

Diameter (nm)	Depth (nm)	Angle of cross-section (°)	Objective lens
1000	350	35	50x
1000	100	11.31	20x
1000	30	3.43	20x
600	350	50	100x
600	110	20.14	50x
500	45	10.2	50x

The migration of the NIH3T3 cells was observed for 2-3 days. The time-lapse microscope images of the cell migration for 25 hours are shown in Figure 12-15, for the nanopit patterns of 1000/350 nm, 1000/100 nm, 600/350 nm, and 1000/30 nm in diameter/depth. The time-lapse images of the cell migration on patterns of 600/110 nm in diameter/depth are not included because the directional migration looks similar to that on patterns of 1000/30 nm in diameter/depth. No effect of repellence and guided migration was observed for the smallest patterns of 500/45 nm in diameter/depth. Cell attachment at the center region of the patterns, i.e. high ratio of texture versus plane (A_C/A_P), was observed up to 5 hours after cell seeding, though a few cells attached for larger nanopit patterns. After 10 hours, the regions of repelling cell adhesion were clearly observed for all patterns, though a few cells still can remain at the center. After 1 day, the formed boundary lines of the repellent region does not change significantly. The Figure 6.16 shows the patterned area and the cell-adhesion repelling zone at day 1 for six different substrates summarized in Table 6.1. The area of the repelling zone changes depending on the nanopit dimensions: becoming larger for larger pits; smaller for the smaller pits. For quantitative analysis, the non-adhesion proportion was defined as (the area of repelling zone, A_N)/(the total area of patterned surface, A_T), and shown in Figure 6.17. The non-adhesion proportion decreases with decreasing depth and decreasing diameter. Interestingly, the repelling effect is higher for the patterns of the 1000/100 nm in

diameter/depth than the patterns of the 600/350 nm in diameter/depth, which means larger diameter of the nanopit is more effective than deeper patterns. When cells are placed on isometric nanopit patterns, they stay on the high crater surface density area though their morphology is totally different from that on the flat or the area of low ratio of texture versus plane. However, the cells headed towards the area of lower ratio of texture versus plane and formed the boundary line of the repelling zone when they met the gradient of ratio of texture versus plane. This constitutes evidence that the cells attempt to detect and migrate to a more proper geometric environment, via a process that may be called directional topographic guidance, as well as chemical (Chemotaxis), ECM density (Haptotaxis), surface rigidity (Durotaxis) and shear stress (Mechanotaxis). The directional topographical guiding can be explained by the curvature sensing mechanism of cells. The cellular membrane curvature is generated by a complex interaction between membrane proteins, lipid layers and physical forces from ECM [118]. One mechanism of curvature sensing (especially, concave curvature) is based on an effective energy for proteins, e.g. BAR domain, to bind lipid layers. The membrane proteins apply forces to lipid layers altering the curvature. Consequently, effective binding energy is needed for protein binding to the layer and maintaining the curvature. If the cellular membrane curvature changes by the ECM shape, the effective binding energy increases with an increasing mismatch between the membrane curvature and protein shape [118]. The other mechanism to explain geometry sensing (especially, convex curvature) is ion channel opening on the cell membrane [1]. As the cells form adhesions on the substrate with micro- or nanoscale convex curvature features, such as nanopits and grooves, the membrane channels might selectively open due to applied differential tension on bending [1]. Therefore, cells can sense their physical environment and move towards preferential geometry or surface roughness that can be used to guide directional cell migration.

The boundary line of the repelling zone looks like a quadrant. The quadrant-like borders formed because the ratios of texture versus plane are identical following the lines as shown in Figure 6.18. The dependence of the ratio of texture versus plane at the boundary of repelling zone on the nanopit dimensions is shown in Figure 6.19. The ratio of texture versus plane does not show significant difference depending on diameter of the patterns, while the ratio of texture versus plane increases with decreasing the depth of the patterns. The crater area with just ~3% of the unit plane area of the patterned surface can repel cell adhesion in the case of 350-nm deep patterns. The ratio of texture versus plane for 100-nm deep patterns is about ~5%. The 1000- and 600-nm diameter patterns show similar ratio of texture versus plane but the large difference of non-adhesion proportion, which means that the similar mechanical forces may be applied to the cells at the boundary of the repelling zone by similar pattern depth, and the larger-diameter craters may offer the larger area of the unit patterned surface. In terms of the angle of cross-section, the ratio of texture versus plane decreases with increase of the angle, as can be seen in Figure 6.20. However, the ratio of texture versus plane does not change significantly when the angle is larger than 10°, which means that the cells may not completely adhere into the nanopits but rather partially adhere to the surface.

The topographically patterned surface is very effective on guiding cell migration, fast and powerful. By combining the designed patterns for large area, cell clusters were formed at the aimed site within 24 hours (Figure 6.21).

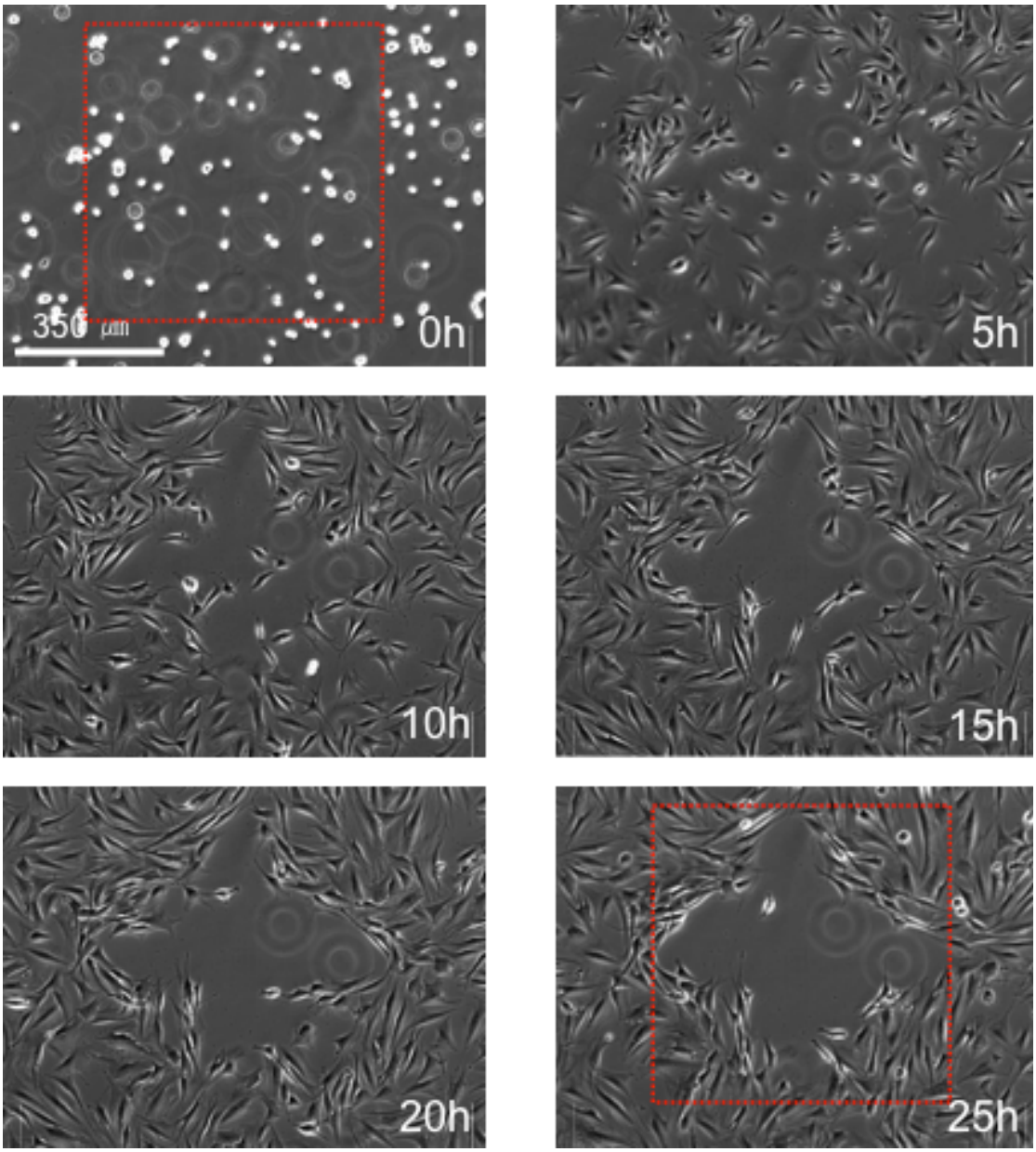

Figure 6.12. Time-lapse phase-contrast images of cell migration on nanopit patterns of 1000 nm in diameter and 350 nm in depth. The dotted line represents the patterned region.

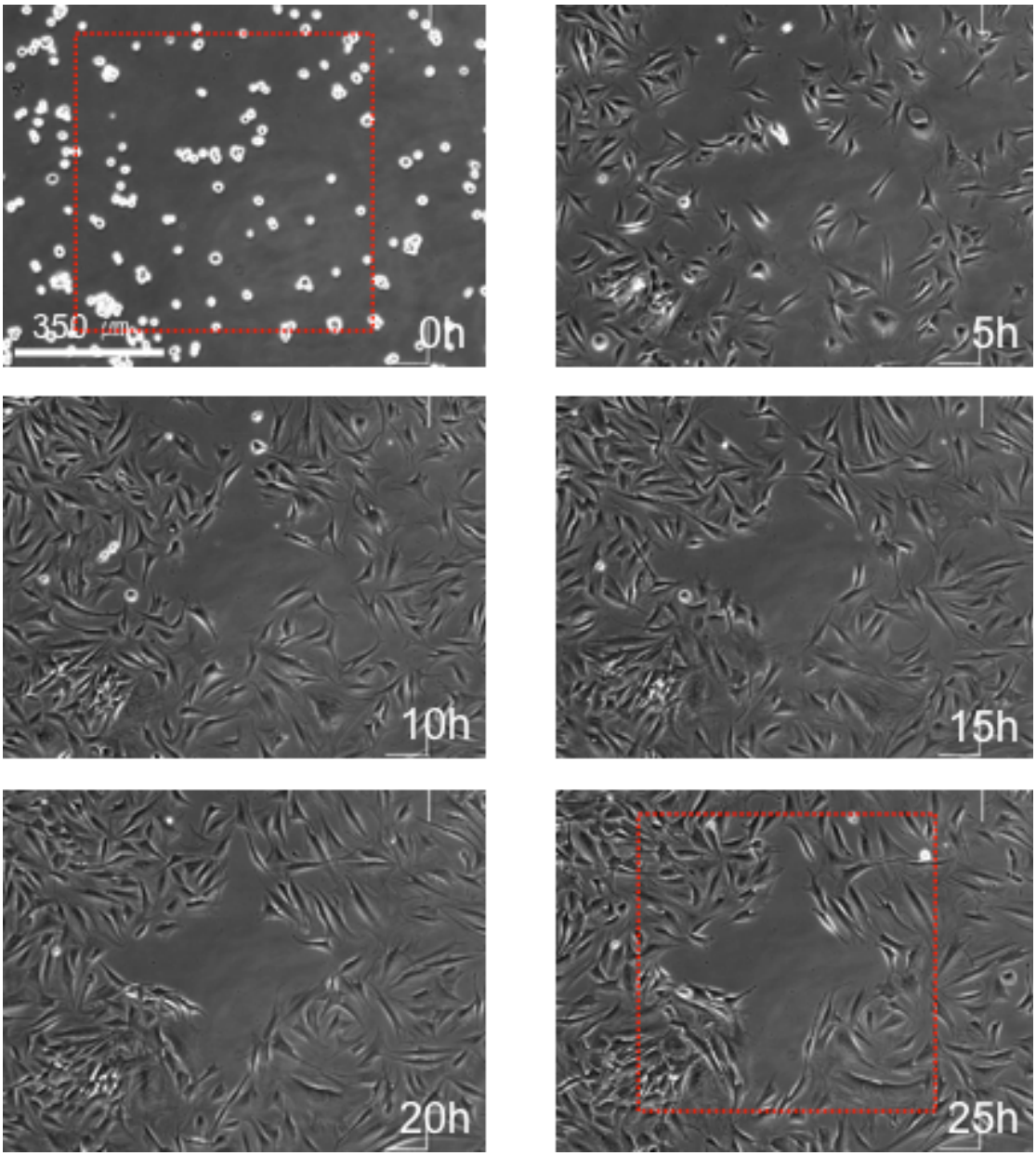

Figure 6.13. Time-lapse phase-contrast images of cell migration on nanopit patterns of 1000 nm in diameter and 100 nm in depth. The dotted line represents the patterned region.

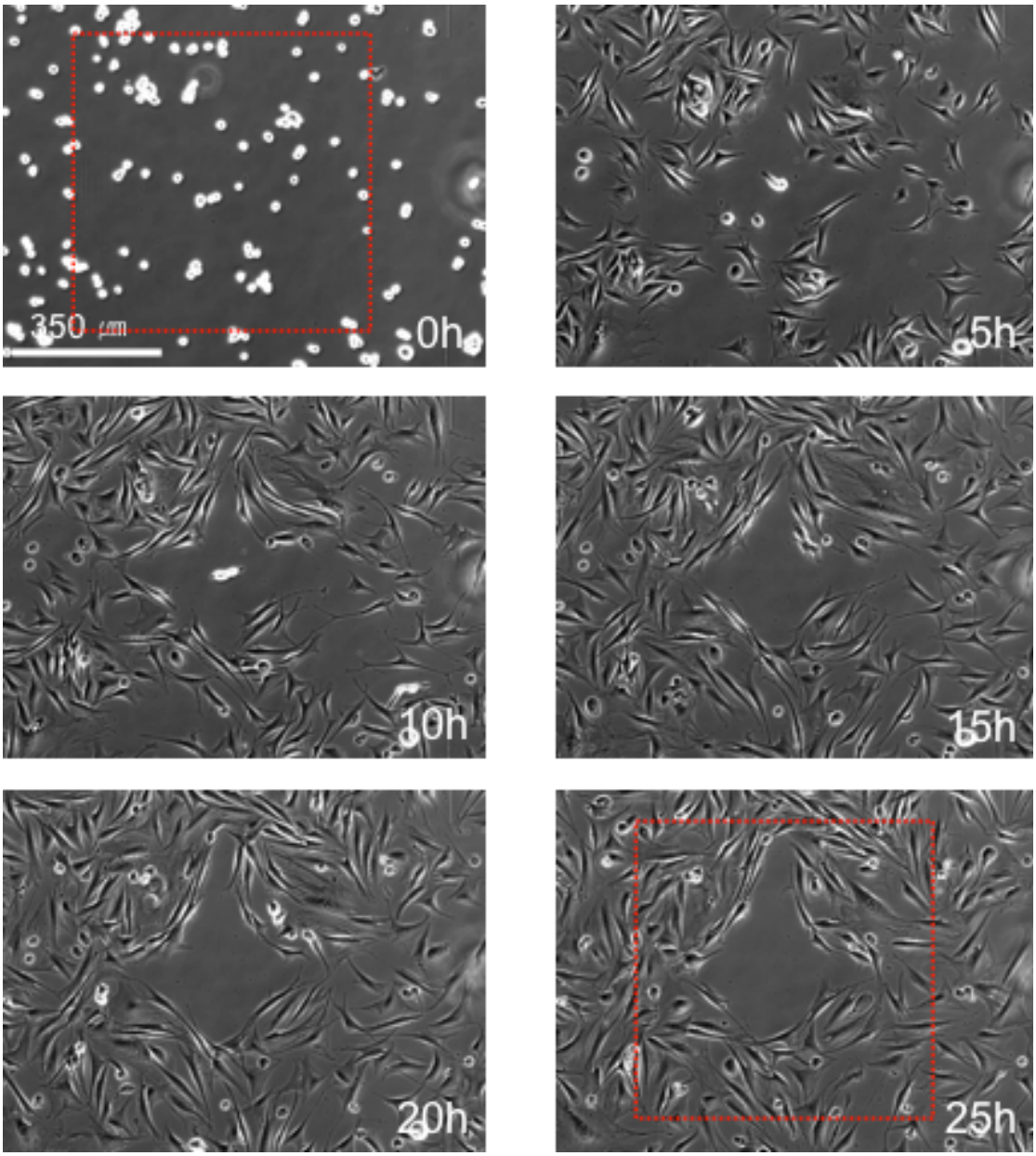

Figure 6.14. Time-lapse phase-contrast images of cell migration on nanopit patterns of 600 nm in diameter and 350 nm in depth. The dotted line represents the patterned region.

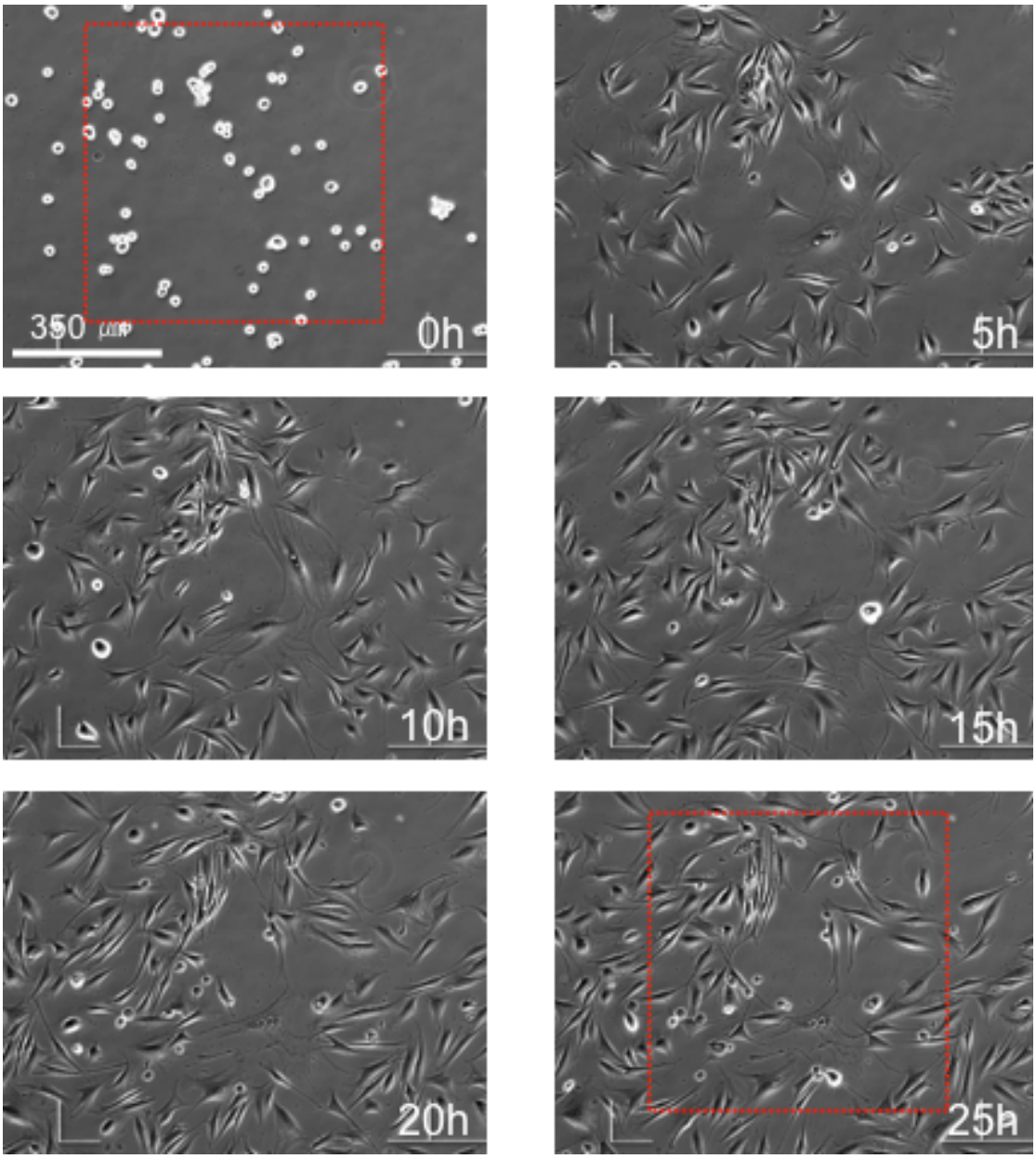

Figure 6.15. Time-lapse phase-contrast images of cell migration on nanopit patterns of 1000 nm in diameter and 30 nm in depth. The dotted line represents the patterned region.

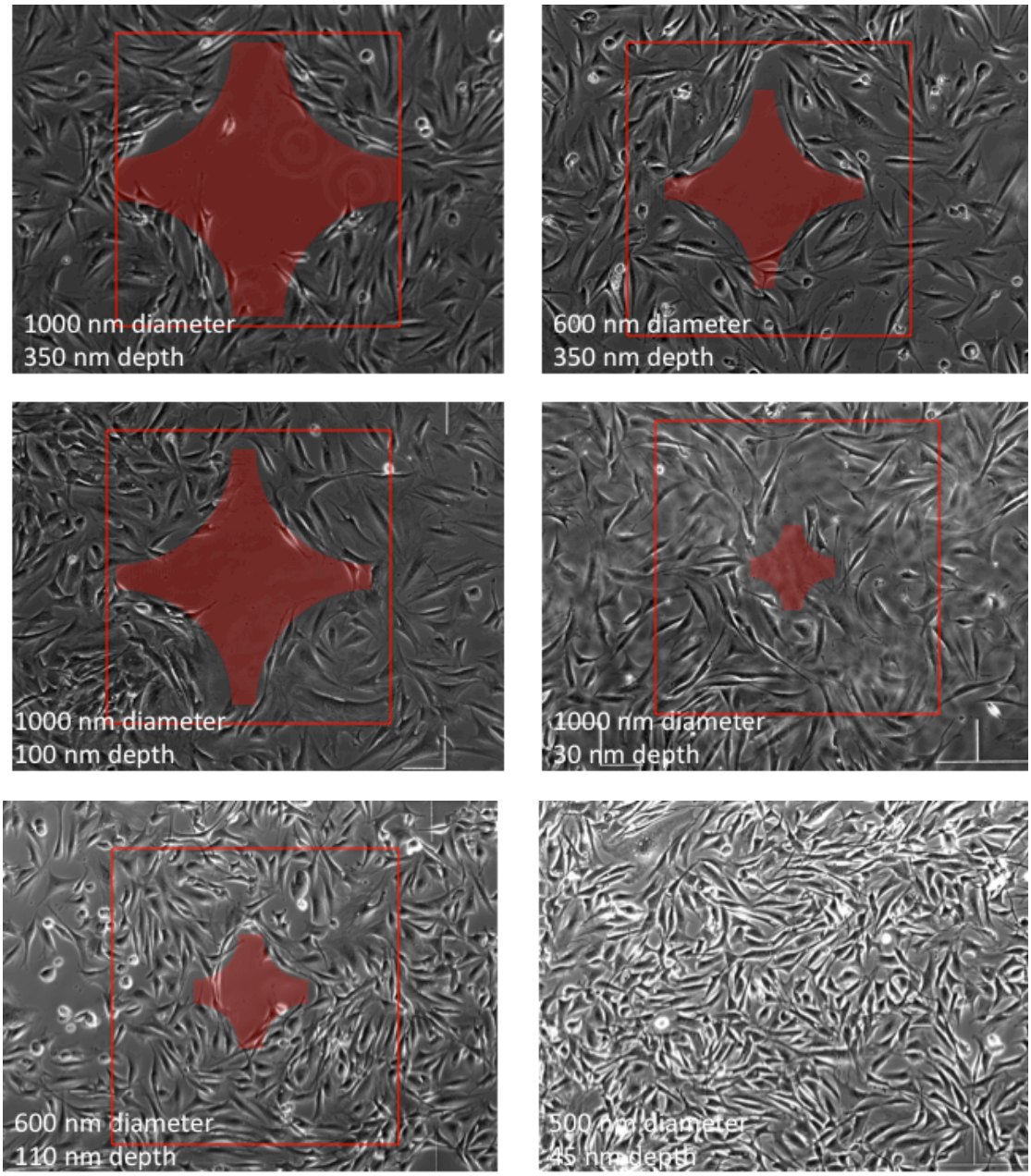

Figure 6.16. Phase-contrast images of cell migration on nanopit patterns at 25 hours after cell seeding. The squares represent the patterned region, and the cross medal shaped region at the center of the patterned area represents the cell-adhesion repelling zone.

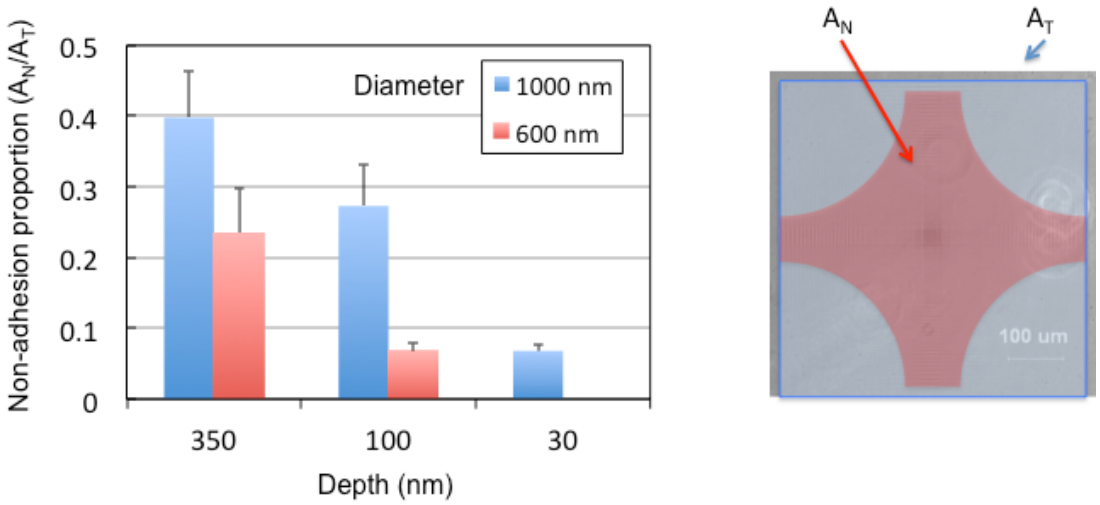

Figure 6.17. Non-adhesion proportion depending on diameter and depth of the nanopits. The depth for 600-nm-diameter crater is 110 nm instead of 100 nm.

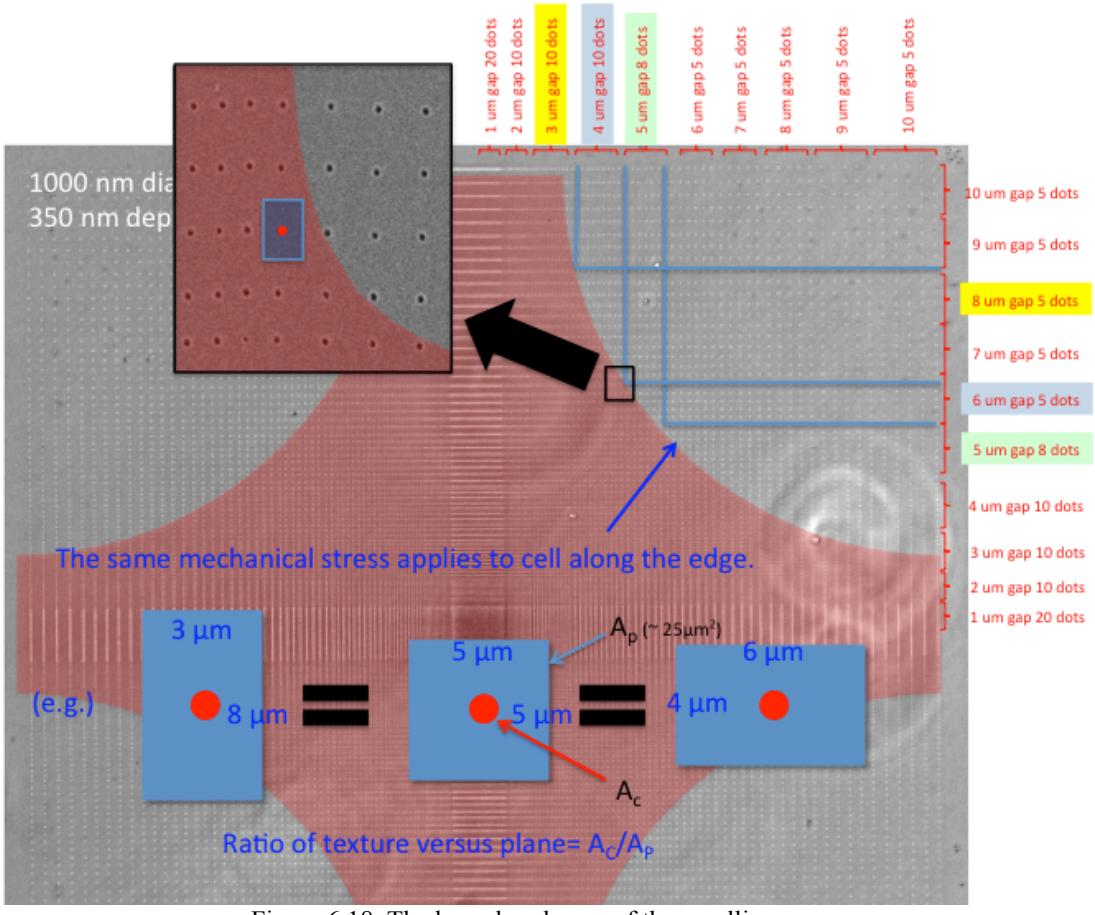

Figure 6.18. The boundary layers of the repelling zone.

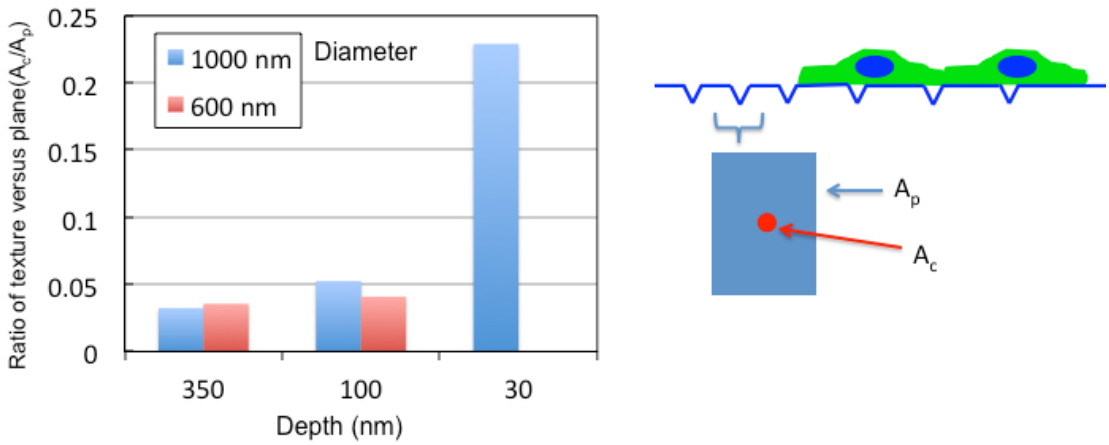

Figure 6.19. Ratio of texture versus plane at the repelling boundary depending on diameter and depth of the nanopit. The depth for 600-nm-diameter crater is 110 nm instead of 100 nm.

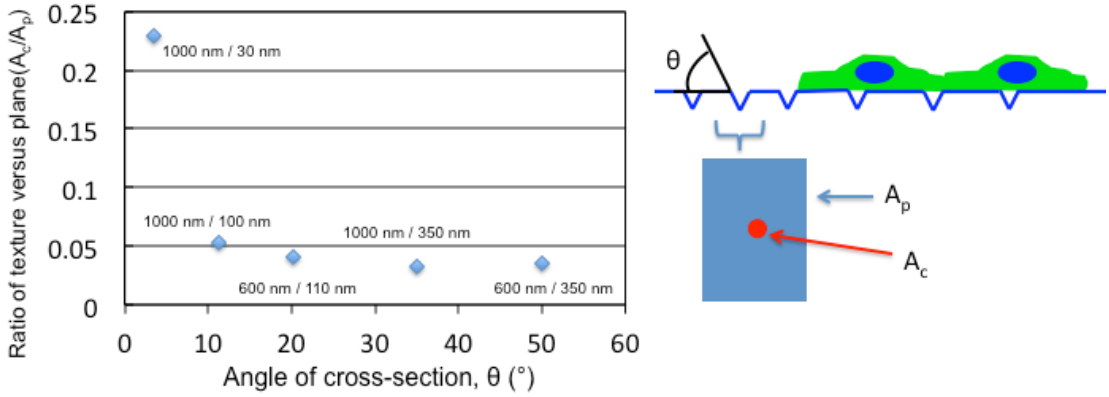

Figure 6.20. Ratio of texture versus plane at the repelling boundary depending on the angle of cross-section.

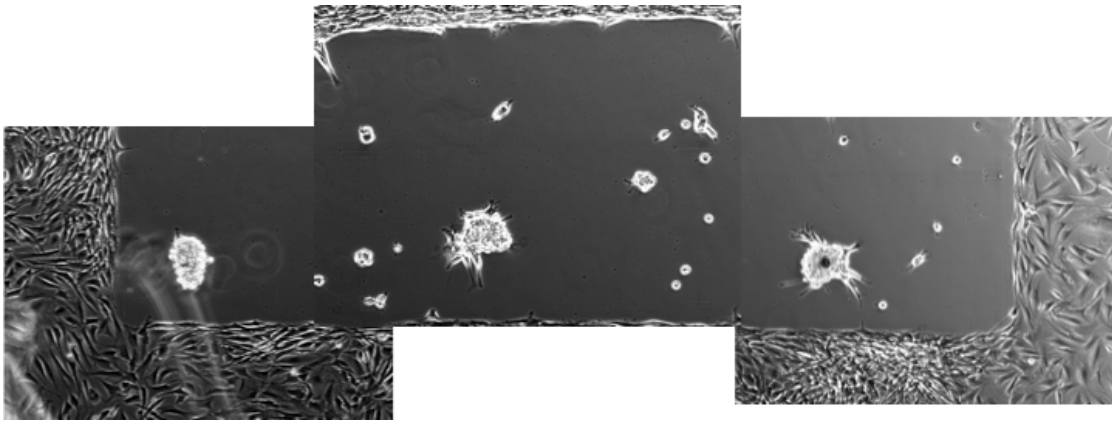

Figure 6.21. Forming cell cluster by spatial gradient of nanopit topographical patterns 24 hours after

6.4. Conclusion

Guided cell migration affected by chemically and topographically patterned surface in nanometer length scale was demonstrated. Cell adhesion ligand density and distribution can be controlled by the nanoscale chemical patterning to directly the spatial arrangement of focal adhesions. The spatial gradient density of cell adhesion molecules can regulate directional cell migration, called haptotaxis. For the chemical patterning, femtosecond laser ablation of PEG brush layers with various thicknesses was investigated by examining the profiles of single pulse craters with AFM. The ablation threshold of the thin film was not influenced by the film thickness when the ablation occurs mainly by the nonthermal process. However, the film thickness influenced the ablated crater diameters. Larger features were fabricated in thicker films with the same laser irradiated fluence due to the mechanical stress propagation. Because of the higher ablation threshold of quartz than PEG films, clear ablation pit arrays can be fabricated without damage to the substrate. Here, fabrication of ablation craters of diameter as small as ~150-nm was achieved.

As well as the chemical patterns, topographical nanopits patterns are used to direct cell migration. For the fabrication of the topographical patterns, femtosecond laser ablation lithography technique was also applied to fused quartz substrates. Varying dimensions of nanopit patterns were examined for effective cell migration and applied mechanical forces. The cells on the spacing gradient nanopit array move towards area of lower ratio of texture versus plane (lower surface area of nanopits in a unit patterned surface) described in Figure 6.22.

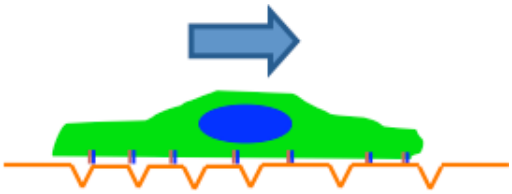

Figure 6.22. Guided cell migration by gradient of topographical patterned surface.

Chapter 7

Measurement of contractile forces generated by individual cells

In this chapter, cell contractility was examined microscopically in order to measure contractile forces generated by individual cells on self-standing fiber scaffolds that were fabricated via femtosecond laser-induced two-photon polymerization. The contractile force is generated by a locomoting cell and is needed to move the cell body forward. Contractility of cells in wound site is important to understand pathological wound healing and develop therapeutic strategies. In particular, contractile force generated by cells is a basic element for designing artificial three-dimensional cell culture scaffolds. Direct assessment of deformation of three-dimensional structured materials has been used to calculate contractile forces by averaging total forces with respect to the cell population number. However, macroscopic methods have offered only lower bounds of contractility due to experimental assumptions and the large variance of the spatial and temporal cell response. Experimental assumptions and calculation errors that arose in previous studies of macroscopic and microscopic contractile force measurements could be reduced by adopting a columnar buckling model on individual, standing fiber scaffolds. Via quantifying eccentric critical loads for the buckling of fibers with various diameters, contractile forces of single cells were calculated in the range between 30-116 nN. In the present study, a force magnitude of approximately 200 nN is suggested as upper bound of the contractile force exerted by single cells. In addition, contractile forces by multiple cells on a single fiber were calculated in the range between 241-709 nN [119].

7.1. Introduction

Tractional and contractile forces generated by fibroblastic cells play a significant role in wound contraction and closure during the healing of an open wound. After cutaneous wounding, fibroblasts migrate to the fibronectin-fibrin wound interface and fill the wound, resulting in the formation of granulation tissue [120, 121]. Tractional forces due to the migration of the fibroblasts reorganize the cells along stress lines to mechanically induce production of collagen and acquisition of proto-myofibroblast phenotype [121]. In addition, tractional forces exerted by migrating cells at the defect edge are known to initiate wound contraction [122]. These cells can be stimulated by tension and growth factors (TGF-β), to be differentiated to myofibroblasts that have α-smooth-muscle actin microfilaments and generate increased contractile forces [121]. Undifferentiated fibroblasts (fibroblasts and proto-myofibroblasts) also contribute to wound contraction, especially over the initial wound closure, although differentiated fibroblasts (myofibroblasts) play a major role in generating contractile forces in defects [121, 122].

A number of studies have been conducted by many investigators to establish the interaction between cell and extra cellular matrix (ECM) and thereby unveil the mechanism of tissue contractions. Focal adhesions (FAs) are known to be capable of providing strong cell adhesion to ECM and are regions of signal transduction regulating cell growth [34]. Mechanical tension sensed through the FAs contributes to formation of stress fibers that transmit contractile forces [34, 121]. The contractile forces of stress fibers are regulated by two kinase systems: myosin light chain kinase (MLCK) generating rapid contracting and Rho-kinase maintaining a sustained contraction [123]. Consequently, cells can generate tractional forces to the substrate during spreading and migrating [34]. Tractional forces were visualized by placing fibroblasts on thin distortable sheets of silicone rubber [124].

After the first visualization by Harris *et al*., the tractional and contractile forces have been visualized and detected by many different approaches. Flexible materials, including thin silicone rubber sheets, have been widely used in these experiments [125, 126]. The deformable substrates were combined with micropatterning and fluorescence imaging of FAs and used to measure tractional forces of myocytes and fibroblasts [127]. These methods require sophisticated computational analysis since the deformation exerted by cells tends to spread on continuous substrates. Hence, instead of uniformly flexible substrates, micromachined cantilevers were used to determine the subcellular forces generated by individual adhesive contacts by Galbraith and Sheetz [128]. Microfabricated arrays of microneedle-like posts were introduced by Tan *et al* [129], removing the complexity incurred by continuous and extensive substrates with simplifying assumptions since distinct tractional forces could be measured. Such techniques can measure tractional forces from isolated cells and subcellular forces during cell spreading and migration. However, they are potentially limited in investigating three-dimensional tissues and interaction between cells and ECM. Experiments with tailored biomimetic materials such as collagen hydrogels and scaffolds have been studied to gain further understanding [130-134]. In these studies, typically millions of cells were seeded on three-dimensional structures and contractile forces generated by the cells were

measured and monitored as a function of time during cell culture [130-132]. Contractile forces by single cells could be calculated by normalizing with respect to the total number of cells [132, 134]. However, derivation of microscopic properties from deformation of macroscopic substrates may involve complicated assumptions that render this exercise difficult since cells are not contracting in the same direction and at the same time. Recently, a single strut from three-dimensional collagen-gel was used to measure contractile forces of individual cells [135]. This novel method could estimate contractile forces of single cells more accurately than previous studies due to fewer experimental assumptions [135]. However, it is limited in controlling the diameter of the struts and producing an accurate account of the eccentricity of the cell loading applied to the struts.

To eliminate constraints encountered in previous measurements, we employed a femtosecond laser to fabricate polymer fiber scaffolds that served to measure contractile forces of individual cells. In our previous study, we developed a two-photon induced polymerization method to fabricate self-standing polymer fiber scaffolds and observed cell morphologies [76, 136]. In the present work, we further used a femtosecond laser scissor to cut fibers, leaving them with one side clamped and the other free. The applied laser power controls the fiber scaffold diameter [136] and henceforth the fiber mechanical strength. Contractile forces exerted by a single cell loaded on the fiber were calculated using buckling theory for an ideal pin-ended column. Therefore, isolated, standing fibers can yield more accurate forces over a wide range. By observing the buckling behavior of fibers during cell adhesion, spreading, and contraction, we could measure contractile forces and reasonably estimate the contractility of individual cells on three-dimensional scaffolds.

7.2. Fabrication of fiber scaffolds by two-photon polymerization

The PR used for the fiber growth was a UV curable organic-inorganic hybrid polymer (ORMOCER®, US-S4, Micro resist technology). The fabrication process is illustrated in Figure 7.1. Aligned fibers separated by different spacings were fabricated in the gap between the two pre-PR-coated glass plates. One side of each the of glass plates which had dimensions of ~3 mm in width, ~25 mm in length and ~1 mm in thickness was spin-coated with the PR, and then pre-baked at 80 °C for 2 min. The two glass plates were assembled with 0.33 mm-thick spacers (Figure 7.1(a)). The PR was then cured by UV light illumination for 30 min and subsequently hard baked at 140 °C for 1 hour.

After the hard bake, uncured PR was filled between the glass plates and fibers were fabricated by high-repetition-rate green femtosecond laser irradiation (Figure 7.1(b)). A femtosecond laser beam (pulse width: <500 fs, repetition rate: 1 MHz, wavelength: 1045 nm, typical M^2: 1.3, FCPA μJewel D-400, IMRA America, inc.) was frequency-doubled to the wavelength of ~523 nm and focused at ~500 μm below the bottom glass plate/PR interface by illuminating from the top through a 5X microscope objective (M plan apo, N.A. = 0.14, Mitutoyo). The power of the laser beam emitted downstream of the objective lens was measured by a power meter and controlled by a

half wave plate and a polarizing beam splitter, and was set at ~3 mW. The exposure duration was controlled by a mechanical shutter and set at 0.2 s. The sample was placed on a motorized X-Y stage. Fibers were fabricated at desired positions by the shutter and stages controlled by a PC. The fabrication setup is illustrated in Figure 4.2.

After the laser irradiation (Figure 7.1(c)), the samples were baked at 110 °C for 10 min, then developed with ORMODEV® (Micro resist technology) for 30 min, rinsed with iso-propanol (IPA) three times, deionized (DI) water with 60 mg/ml asolectin (BioChemika), dipped in DI water and exposed with UV lamp for 30 min to cure completely. The sample was afterward dipped in 70% ethanol to sterilize, exposed for coating to 20 μg/ml fibronectin (FN) (Sigma) in phosphate buffered saline (PBS) (Gibco Invitrogen) for 1h, and finally rinsed with PBS three times.

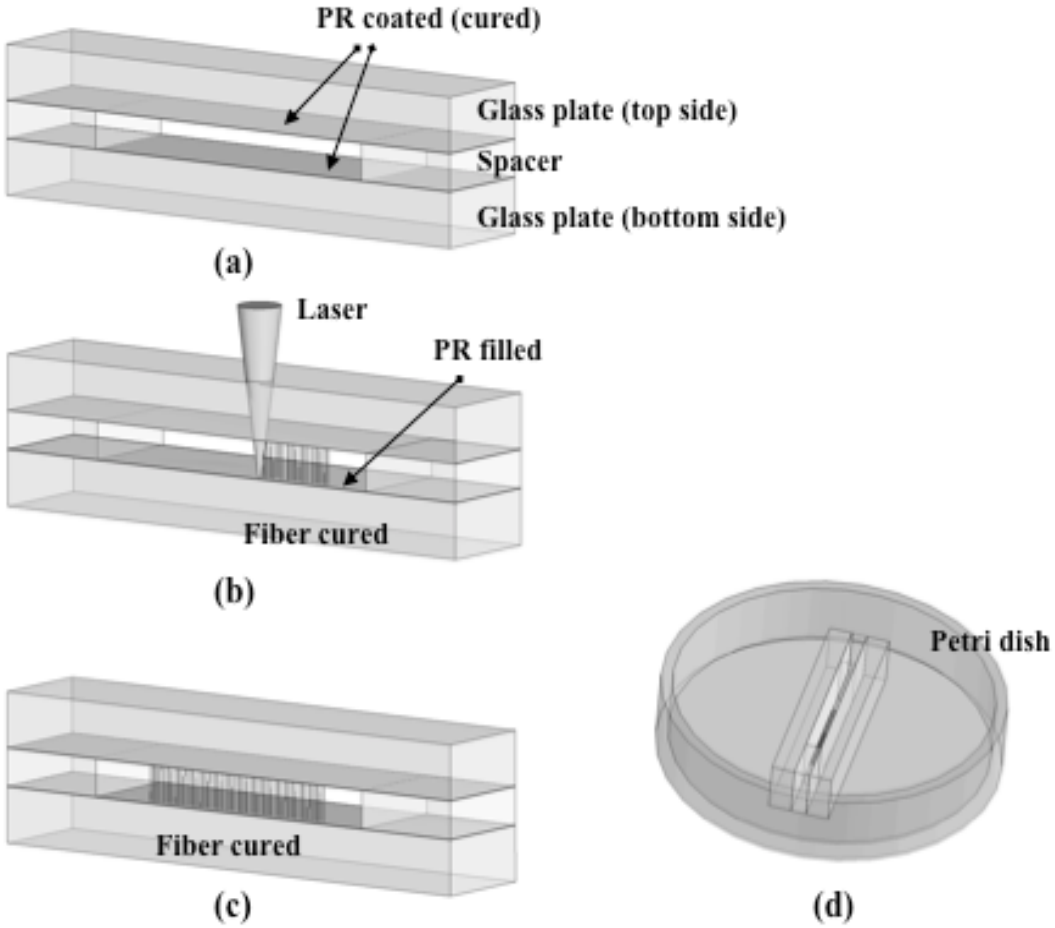

Figure 7.1. Illustration of order to produce aligned fibers between glass plates. Two glass plates are fixed with space and inner side is precoated with photopolymer (a). Photopolymer is filled between the glass plates and fibers are cured by femtosecond laser irradiation (b). Post baked and developed as a result fibers are fabricated (c). Photopolymer is cured completely by UV light irradiation, the sample is washed, sterilized FN coated, and put in Petri dish for subculturing (d).

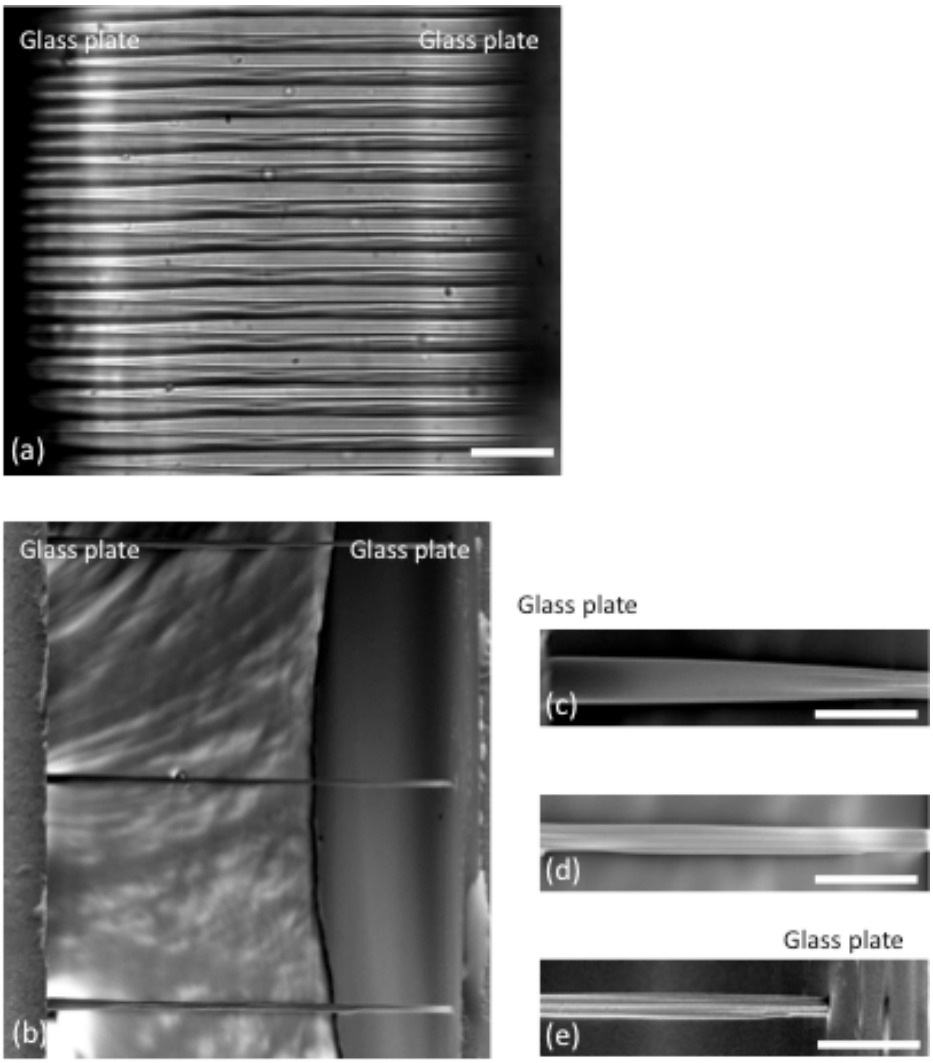

Figure 7.2. Optical and scanning electron images of fibers. (a) and (b)-(e) are optical and scanning electron images, respectively. The development and washing, the pitch of the fiber was 25 μm and the length is 0.33mm (a). Whole images of the fibers, the pitch of the fibers was 200 μm (b). Magnified image of (b) at the top glass plate (c), in the middle (d), at the bottom glass plate (e), respectively. The scale bar indicates (a) 50 μm, (b) 100 μm and (c)-(e) 20 μm.

We previously reported that fibers of ~1.8 mm length could be readily fabricated after ~1 s illumination with the ~5 mW laser power when the polymer was filled in a thick glass cuvette. The diameter of the fiber was about 10 μm in the middle and decreased toward the edges [76]. Through process optimization, fibers of 0.33 mm in length were fabricated bridging the two glass plates.

After laser irradiation, the sample was developed and then washed with IPA three times, once with surfactant (asolectin) solution and DI water. Figure 7.2(a) shows developed fibers of ~0.33 mm length and ~25 μm pitch. The fibers grew upward from the surface of the bottom glass plate. The diameter at the bottom was ~6 μm and at the top ~9 μm upon illumination over a 0.2 s exposure time with 3 mW laser power. When the sample was washed with DI water instead of the surfactant solution after IPA, fibers bundled together. In order to achieve longer aligned fiber fabrication without bundling,

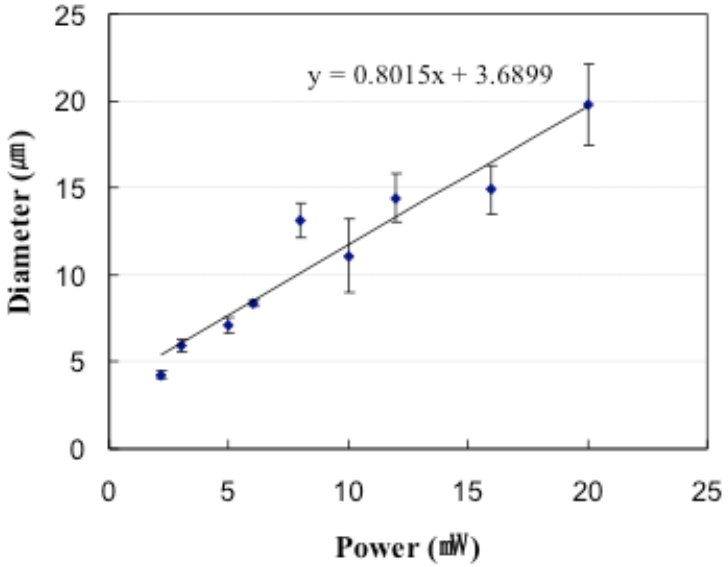

Figure 7.3. The diameter of fibers is shown for different power of incident laser. The exposure time is 200 ms.

supercritical drying technique is expected to be efficient. Details of surface morphology of the fabricated fibers by SEM are shown in Figure 7.2 (b) – (e). Interestingly, the grown columns were composed of smaller and directional fibers at the middle (Figure 7.2(d)) and bottom (Figure 7.2 (e)) part the fibers, while the fiber close to the top glass plate (Figure 7.2 (c)) was thicker and smoother. The geometry of the fabricated fibers may depend on the nonlinear propagation characteristics of the ultra-short pulsed laser beam during the resin curing as well as the evolution of the polymerization process. Further studies at a fundamental level are in progress in order to unveil the detailed mechanisms. Nevertheless, the directional sub-bundle structures are expected to affect cell behavior, possibly assisting directional migration/growth along the fiber axis. The fiber diameter can be controlled by adjusting laser power and irradiation time [76]. Figure 7.3 shows the diameter dependence on laser power irradiated through the 5X objective for a period of 200 ms. The calibration curve shows an almost linear relationship between fiber diameter and laser power. However, the standard deviation increases as the power rises because nonlinear propagation effects become more pronounced at high power.

7.3. Characterization of fiber scaffolds

Through the fabrication process mentioned above, the polymer fibers were ~200 μm in length, with one end clamped and the other free. The fiber diameter (~5-20 μm) could be controlled by adjusting laser power and irradiation time [136]. The diameters were measured from optical transmitted images taken via a 40x microscope objective

(LUCPlanFLN, N.A. = 0.6, Olympus) on an inverted microscope (IX71, Olympus) before cell culturing.

The elastic modulus (E_s) of the fiber scaffolds was measured via atomic force microscopy (AFM, XE-100, Park Systems) with a tip-less cantilever (TL-CONT-SPL, Nanosensors). The force constant of the cantilever was measured by a thermal tuning method [138] and calculated to be 0.0363 N/m using AFM software (XEI, Park Systems). A fiber with 200-µm length (l) and 20-µm diameter (D) was chosen as reference. The fiber sample was placed on a plastic dish filled with water (Figure 7.4). The fibers are of circular cross section. Therefore, the modulus was obtained from equation (1) with the cantilever displacement (d_c), the force constant of the cantilever (K_c), the relative deflection of the free end of the fiber (d_f), and moment of inertia for a cylinder [139].

$$E_s = \frac{64 \cdot K_c \cdot (d_c - d_f) \cdot l^3}{3\pi D^4 d_f} \tag{7.1}$$

The bending test was performed independently five times to yield an average value of the modulus. Fibers with 200-µm length and 20-µm diameter were tested under water (Figure 7.4) via AFM, and linear elastic behavior was observed (Figure 7.5). The 20-µm diameter fiber was chosen in order to generate similar bending displacements of the fiber, d_f, and the AFM cantilever, $d_c - d_f$, (see Equation (7.1)) since accurate

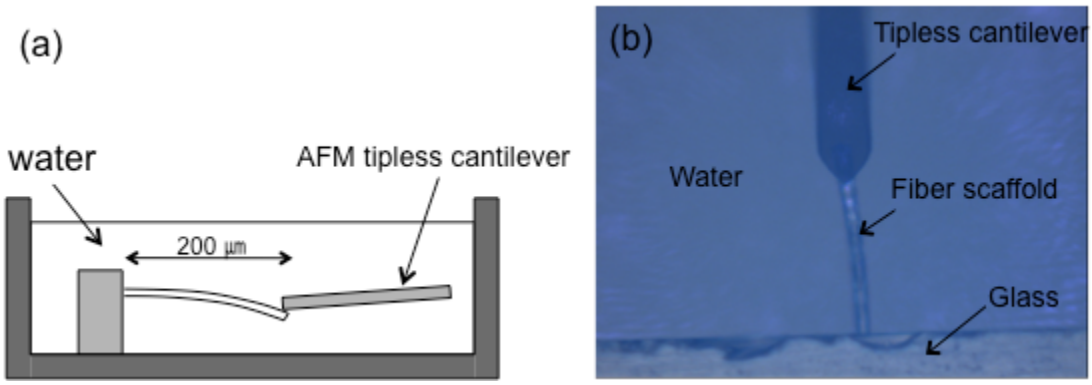

Figure 7.4. Schematic of bending test with fiber scaffolds (a) and a top view of a real optical image (b).

measurements cannot be achieved if the displacements, d_f or $d_c - d_f$, are very small. Using Equation (1), the elastic modulus of the fiber was calculated to be 6.01±0.87 MPa. The bending test was also performed on dry fibers, but the results did not exhibit significant deviation from the submerged ones.

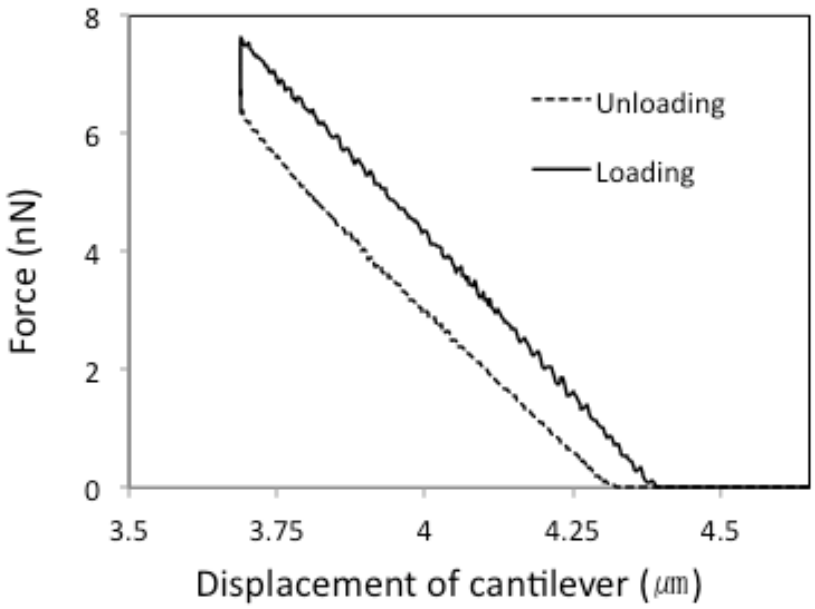

Figure 7.5. Characteristic of load-unload bending experiment performed via AFM for a single fiber.

7.4. Cell morphology on fiber scaffolds

7.4.1. Cell culture and imaging

Fibroblasts, NIH3T3, were cultured in a 75-cm^2 culturing flask (Corning) containing Dulbecco's Modified Eagle Medium (Gibco Invitrogen), 10% fetal bovine serum (FBS) (Gibco Invitrogen) and 100 units/ml penicillin (Gibco Invitrogen), maintained at 37°C and 5% CO_2 culture incubator. Before conducting the experiments, confluent cells were detached from the flask by 0.05% Trypsin-EDTA (Gibco Invitrogen) and seeded onto the fiber scaffolds which were placed in sterile polystyrene well plates and maintained in CO_2-independent media (Gibco Invitrogen), 10% FBS, 100 units/ml penicillin, and 1% GlutaMAX (Gibco Invitrogen). Cell mediated contraction was monitored via a 10× objective lens (Plan Achromat, N.A. = 0.25, Olympus) with an inverted microscope (IX71, Olympus) with temperature maintained at 37°C. Transmission images were taken every 1 minute with a digital CCD camera (Retiga 2000R cooled, Qimaging) for about 400 min (~7 h). Cell migration or bridging was monitored by the consecutive transmission images, and isolated cells were chosen to measure single cell-mediated contractile forces.

For fluorescence images, the cells on sustained fibers between two glasses (before cutting the fibers) were fixed with 3.7% formaldehyde (Fisher Scientific), and then permeabilized with 0.1% Triton X-100 (Fisher Scientific) after one day culturing. Actin cytoskeletons were stained with 330 nM alexa fluor 488 phalloidin (Invitrogen) for 40

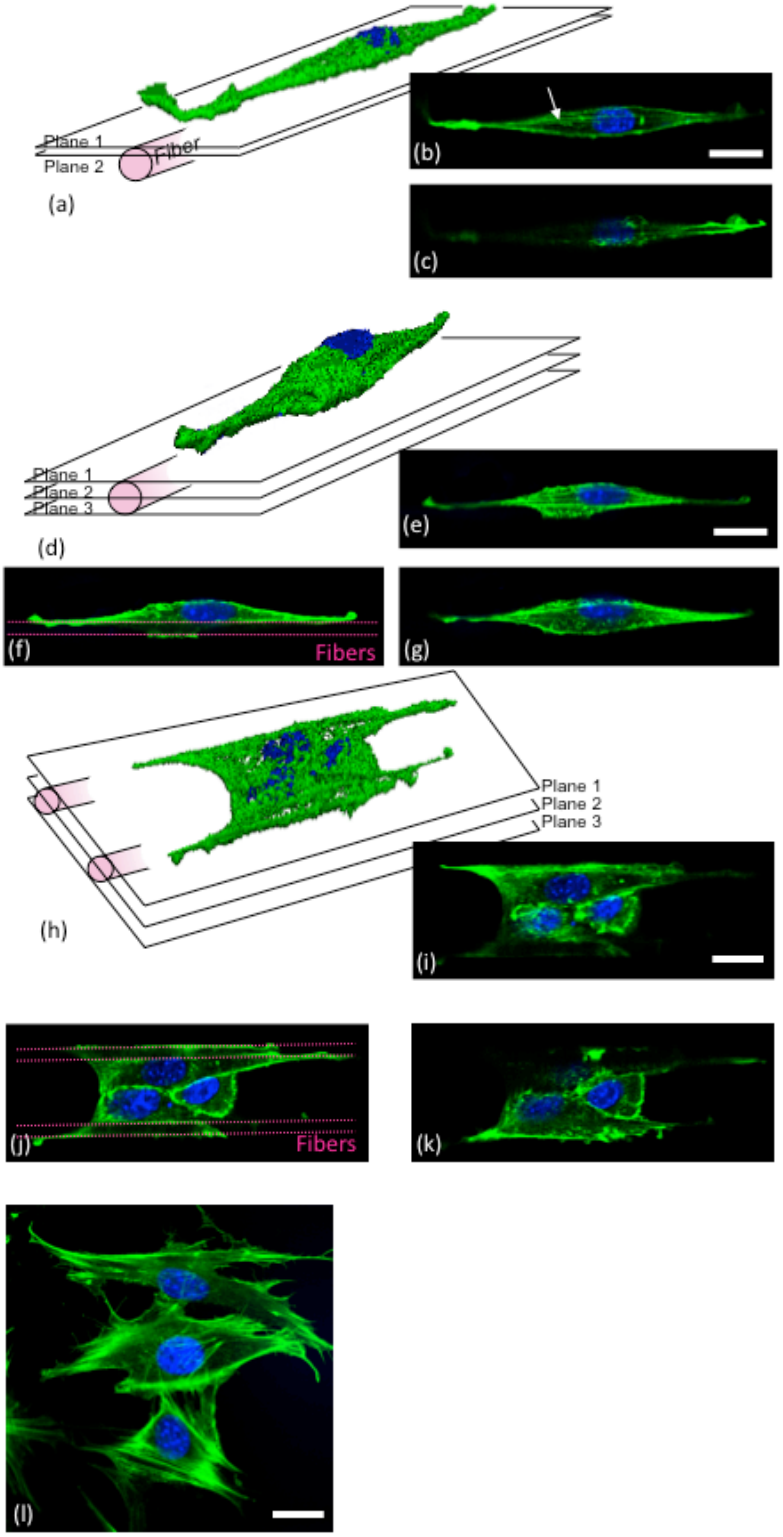

Figure 7.6. Florescent confocal images are shown of actin cytoskeletal networks (Alexa 488-phalloidin; green) and nuclei (DAPI, blue) of NIH-3T3 cells. The cells cultured for one day are shown, and locate on single fiber (a)-(c), wrap a fiber (d)-(g) and place between fibers (h)-(k). Three-dimensional images (a), (d), (h) were obtained by image processing from layer by layer images. Confocal slices are shown at different fiber positions; on the top of the fiber (plane 1; (b), (e), (i)), the middle of the fibers (plane 2; (c), (f), (j)) and the bottom of the fibers (plane 3; (g), (k)). NIH-3T3 cells cultured on flat polymer film coated surface on a cover slip for control (l). The scale bar indicates 20 μm.

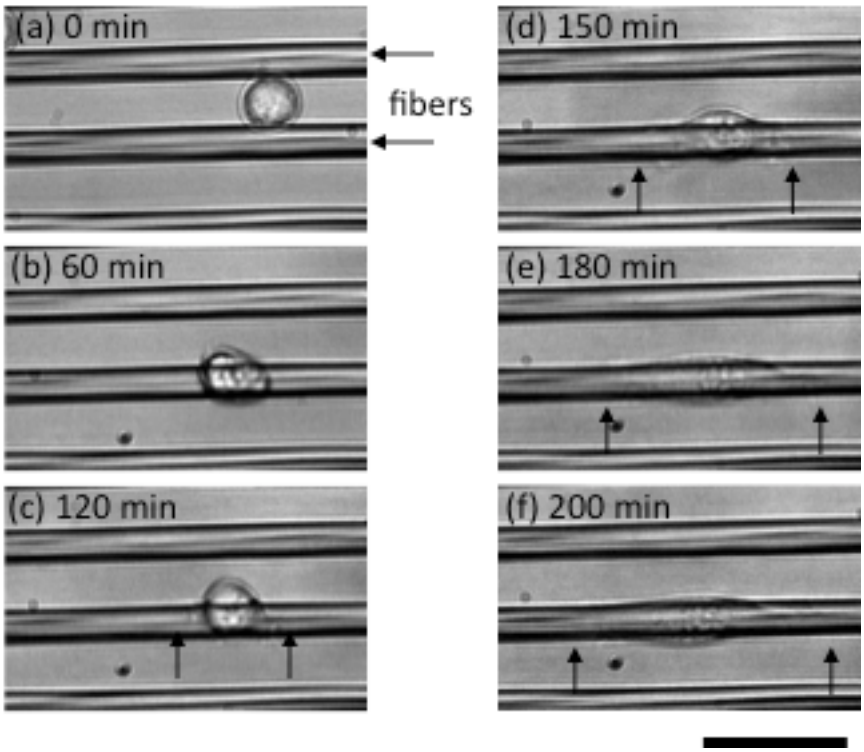

Figure 7.7. Snapshots of Transmitted images of a NIH-3T3 cell attaching process, after 0 min (a), 60 min (b), 90 min (c), 120 min (d), 150 min (e), 180 min (f) and 200 min (g). Arrows indicates the edge of the cell. The scale bar indicates 50 μm.

min, and nucleus were stained with 300 nM DAPI (Invitrogen) for 4 min. The samples were kept in PBS and the images were taken by a 510 Meta UV/VIS confocal microscope (Zeiss) with a 63× W Plan Apochromat dipping objective lens (Zeiss).

7.4.2. Cell morphology

In order to demonstrate the biocompatibility of the fabricated fibers, fibroblast cell line (NIH-3T3) was cultured on fibers coated with FN. The samples were dipped in cultural solution, and then cells were spread and attached on fibers. Figure 7.6 shows the typical morphology of actin cytoskeleton (green) and nuclei (blue) dyed NIH-3T3 cells cultured over one day. Three- dimensional images (Figure 7.6(a), (d), (h)) are obtained by a confocal microscope. Confocal slices are shown at different fiber positions: on the top of the fiber (plane 1; Figure 7.6(b), (e), (i)), the middle cross sectional plane (plane 2; Figure 7.6(c), (f), (j)), and the bottom of the fibers (plane 3; Figure 7.6(g), (k)). Three dominant morphologies were observed in the case of NIH-3T3 cells: (i) elongated on a fiber, (ii) partially wrapped around a fiber and (iii) attached on multiple fibers. A NIH-3T3 cell, located on a single fiber (Figure 7.6(a)), follows the fiber geometry forming shapes of high length / width ratio. Two actin cytoskeleton lines (arrow in Figure 7.6(b)) are on the top surface of the fiber. These lines are not observed as the slice plane shifts downward by 3 μm, indicating that the cell conforms to the fiber surface (Figure 7.6(c)).

A single NIH-3T3 cell partially wraps and is stretched along the fiber (Figure 7.6(d)-(g)). Although Figure 7.6(g) is observed through the fiber, the actin cytoskeleton can be clearly observed since the fiber material is transparent in the visible and infrared wavelength ranges [20]. Not only the cytoskeleton, but also the cell nucleus is elongated and oriented on the fiber. Dunn and Heath reported that smaller radius cylindrical substrate has more influence on elongation and orientation using glass fibers with diameters of 254 μm and 109 μm [140]. Rovensky and Samoilov also showed that elongation and orientation of the fibroblast cells on cylindrical substrata with diameters of 50 μm and 25 μm were increased after 8 or 24 hours of cultivation. At that cultivation stage, normal fibroblast cells presented straight actin filament bundles [141]. Our study shows fibroblast cells on a single fiber with smaller diameter of ~10 μm and aligned multiple fibers. Elongation and orientation of fibroblast cells appear to occur earlier on thinner than on thicker fibers. Time-lapsed optical transmission images shown in Figure 7.7 reveal the transient extension sequence of a single cell on a single fiber. At first, a cell placed between two fibers (Figure 7.7(a)) moved to attach on a single fiber (Figure 7.7(b)) over which it spread and then covered (Figure 7.7(c) – (g)). After 200 min, the cell was elongated till about 100 μm. Even though straight actin fiber bundles inhibit the cell body bending, NIH-3T3 cells partially wrap up fibers of ~9 μm in diameter.

7.5. Cell contraction on fiber scaffolds

7.5.1. Calculation of contractile forces

When a cell grows on the fiber, an axial compressive force (P) is generated by the cell contraction. If the contractile force is larger than the critical load (P_{cr}), buckling of the fiber occurs. The critical buckling load generated by an individual cell attached on the fiber as displayed schematically in Figure 7.8 was calculated by the Euler buckling load formula [142]:

$$I = \frac{\pi D^4}{64} \tag{7.2}$$

$$P_{cr} = \frac{\pi^2 E_s I}{L_{eff}^2} \tag{7.3}$$

where I signifies the moment of inertia for a cylinder, and L and D denote the length and diameter of the fiber, respectively. In this study, L_{eff} was defined as the length of a single cell on a fiber. The length of a single cell on a fiber was taken at ~100 μm, consistent with our previous work [136]. Because the cells attach and apply contractile forces on the surface of the fiber scaffolds, eccentricity should be considered when calculating the critical buckling load. Consequently, a secant formula given by equation (4) was used to calculate the contractile force [142]. The eccentric load (P_{ec}) and critical load (P_{cr}) are associated to the eccentricity (e), the distance from the neutral axis to the

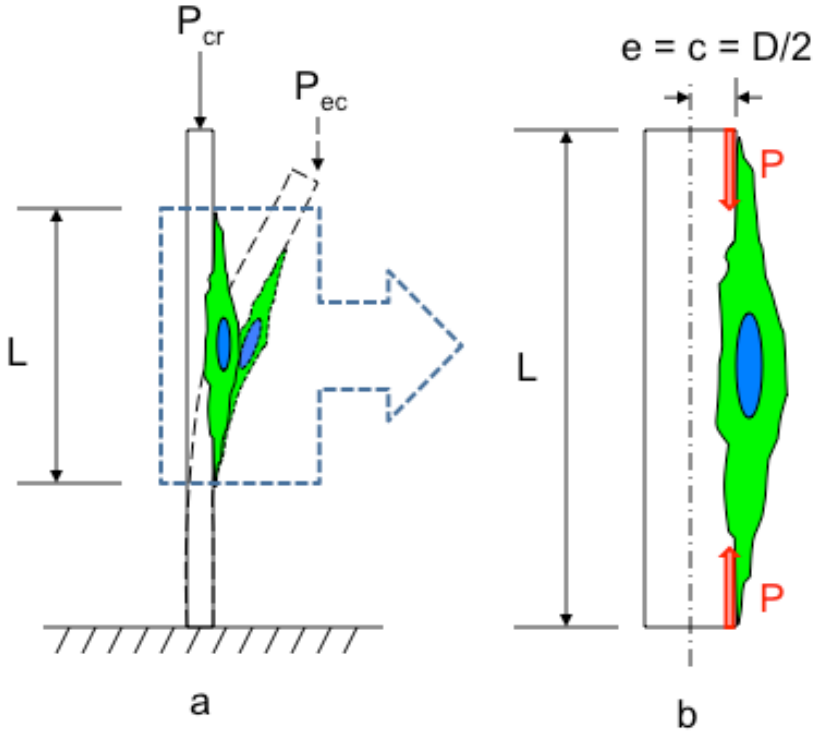

Figure 7.8. Schematic of buckling of a fiber scaffold by a contractile force generated by a single cell. Once a cell attach and spread on a fiber, the fiber started to be buckled (a). The total forces to buckle the fiber were considered to act at the end of the cell and on the surface of the fiber (b).

fiber surface (c), the cross-sectional area of the compression column (A), and the radius of gyration ($r = \sqrt{I / A}$):

$$P_{cr} = P_{ec}\left[1 + \left(\frac{e \times c}{r^2}\right)\sec\left(\frac{L_{eff}}{2r}\sqrt{\frac{P_{ec}}{AE_s}}\right)\right] \tag{7.4}$$

In this calculation, L_{eff} was also defined as 100 μm, and e and c were taken as the fiber radius. Substituting the critical load (P_{cr}) calculated from the equation (3) into Equation (4), the cell-generated contractile forces were calculated.

7.5.2. Single cell-mediated contractile forces

Single cell-produced contractile forces were obtained by calculating eccentric loads for buckling of a cylindrical column. By substituting the fiber elastic modulus into Equation (7.3), the critical loads for buckling were calculated. Thereafter, the eccentric loads were derived upon substituting the critical loads into Equation (7.4). Results for six

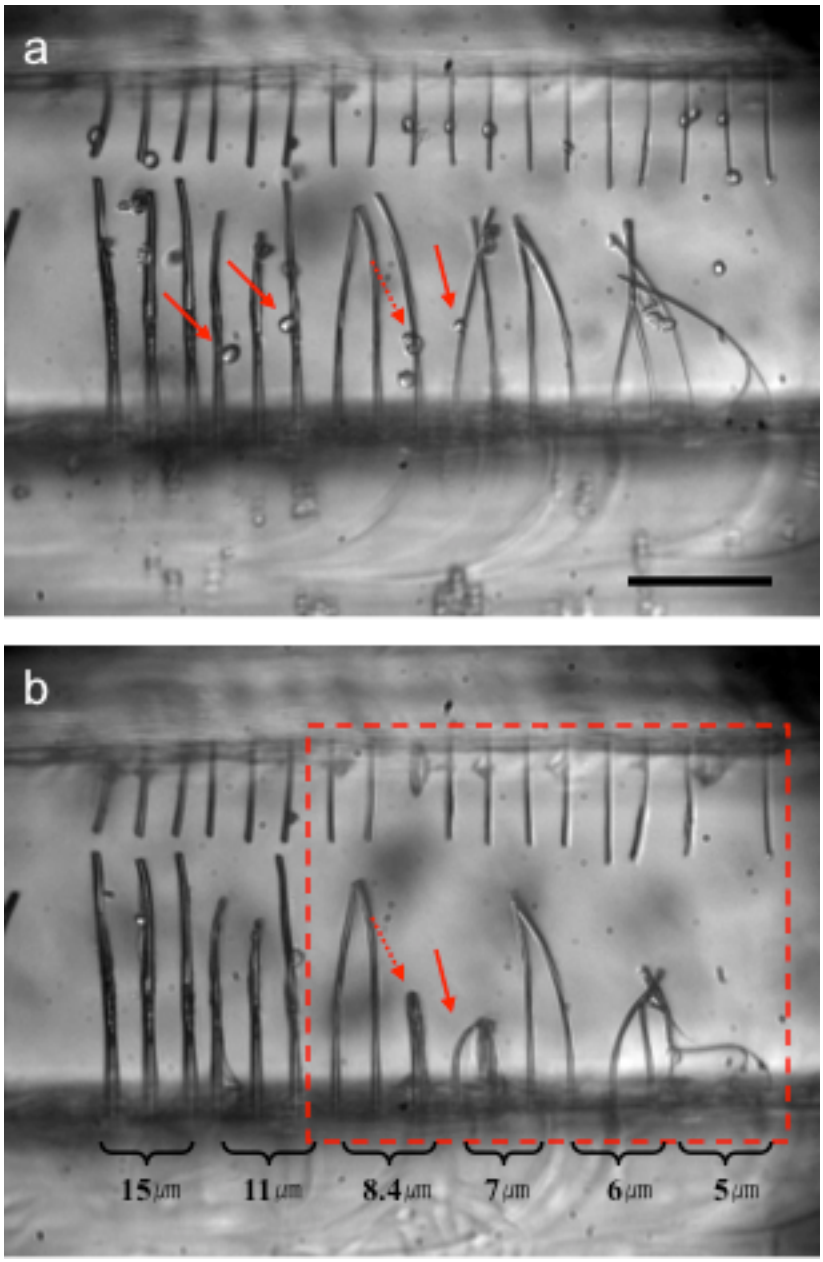

Figure 7.9. Microscope images of fiber scaffolds right after cell loading (A) and 350 min after cell loading (B). Black-line arrows indicate cells right before cell adhesion, and white-line arrows indicate cells on buckled fibers. Solid-line arrows indicate single cells, and dashed-line arrow indicated multiple cells. The dashed-line box in (B) highlights buckled fibers. Scale bars: 200 μm.

.

Table 7.1. Calculated critical loads and eccentric loads for fiber buckling depending on fiber diameters.

Diameter (μm)	P_{cr} (nN)	P_{ec} (nN)
5	181	30
6	376	63
7	697	116
8	1189	198
8.4	1445	241
11	4249	709

different diameters are shown in Table 7.1. Figure 7.9(a) shows fiber scaffolds having six different diameters right after cell loading. Some fibers were already bent due to pressure by shock wave or bubble generated during laser cutting process. The errors from the bent fibers were neglected because fiber buckling by cell-mediated forces occurred at the similar diameters of fibers through several experiments. Figure 7.9(b) was taken at an elapsed time of 350 min after cell loading. Fiber buckling was observed for the 5-, 6-, 7-, and 8.4-μm diameter fibers, although the 8.4-μm diameter fiber was buckled by multiple cells. On the basis of more than five independent experiments, we concluded that individual cells could buckle 7-μm or smaller diameter fibers, but not 8-μm or thicker fibers. This suggests that the contractile forces generated by an individual cell are in the range of 30-116 nN comprising the eccentric critical loads for 5-7-μm diameter fibers. In addition, it should be noted that an upper bound of the single cell-mediated contractile force measured in this study is ~200 nN that is the eccentric critical load for 8-μm diameter fibers. Therefore, buckling of thinner fibers occurs much faster than thicker fibers since the critical loads for buckling of thinner fibers are smaller than the maximum contractile forces of cells (Figure 7.10 and Table 1). Buckling of fibers with diameter of 5-μm started at 30 min after cell loading. In contrast, buckling could be observed at an elapsed time of 160 min for the 6- and 7-μm diameter fibers.

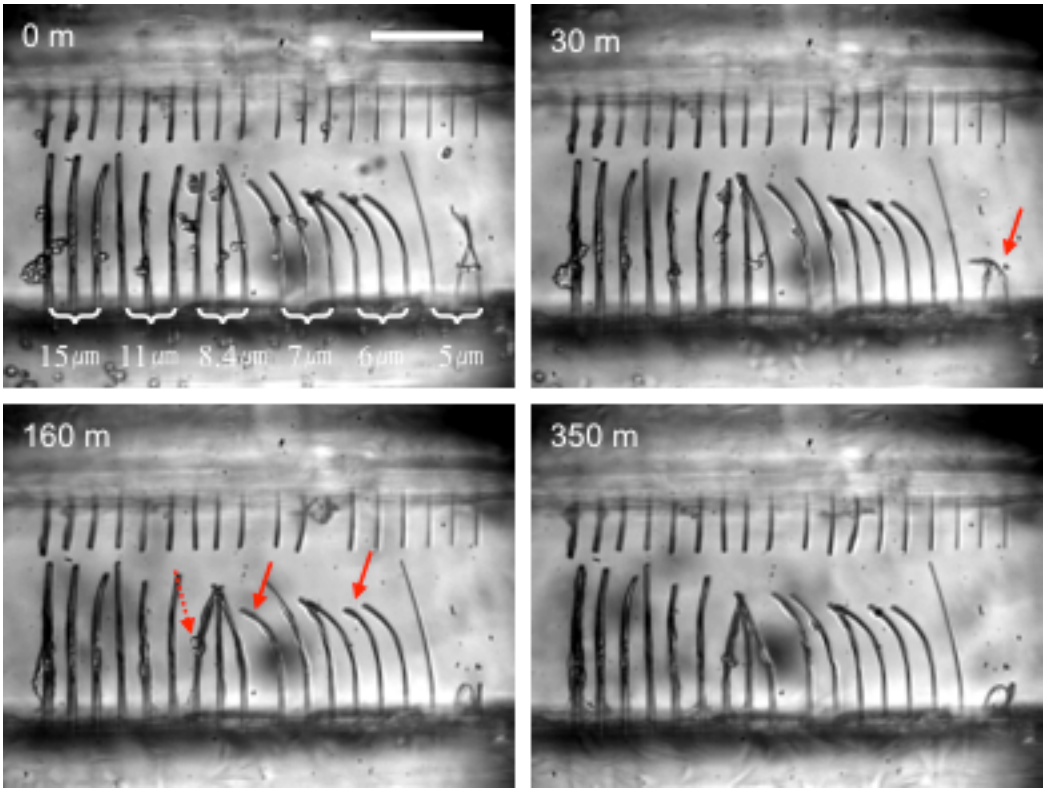

Figure 7.10. Time-lapse microscope images of fiber buckling for different size fibers. Arrows represent the beginning points of buckling, and the numbers in the top-left corner indicate the time. Black-line arrows indicate cells right before cell adhesion, and white-line arrows indicate cells on buckled fibers. Scale bars: 200 μm.

7.5.3. Multiple cell-mediated contractile forces

While individual cells could buckle fibers thinner than 8 µm, 8.4-µm diameter fibers buckled only upon loading by multiple cells. Thicker fibers with diameters of 11- and 15-µm remained straight and intact (Figures. 7.9 and 7.10). The eccentric critical loads for the 8.4-µm and 11-µm fibers are 241 and 709 nN, respectively (Table 7.1). Since multiple cells tend to accumulate in a restricted area, the respective buckling loads were not linearly proportional to their number. Furthermore, the buckling load did not exceed 709 nN, i.e. the buckling load of 11-µm diameter fiber. This suggests that the contractile forces generated by multiple cells on a single fiber lie between 241-709 nN. The thicker fibers (11 and 15 µm) were not buckled by multiple cells, but rapid buckling of thinner fibers (6 µm) by multiple cells was observed. Figure 7.11 shows time-lapse images of 6-µm diameter fiber buckling induced by single and multiple cells. The fiber buckling by multiple cells (60 min) occurred rapidly compared to individual cells (120-160 min). This result suggests that the contractile forces generated by multiple cells exceed those by single cells, although the forces do not scale linearly proportional to the number of cells.

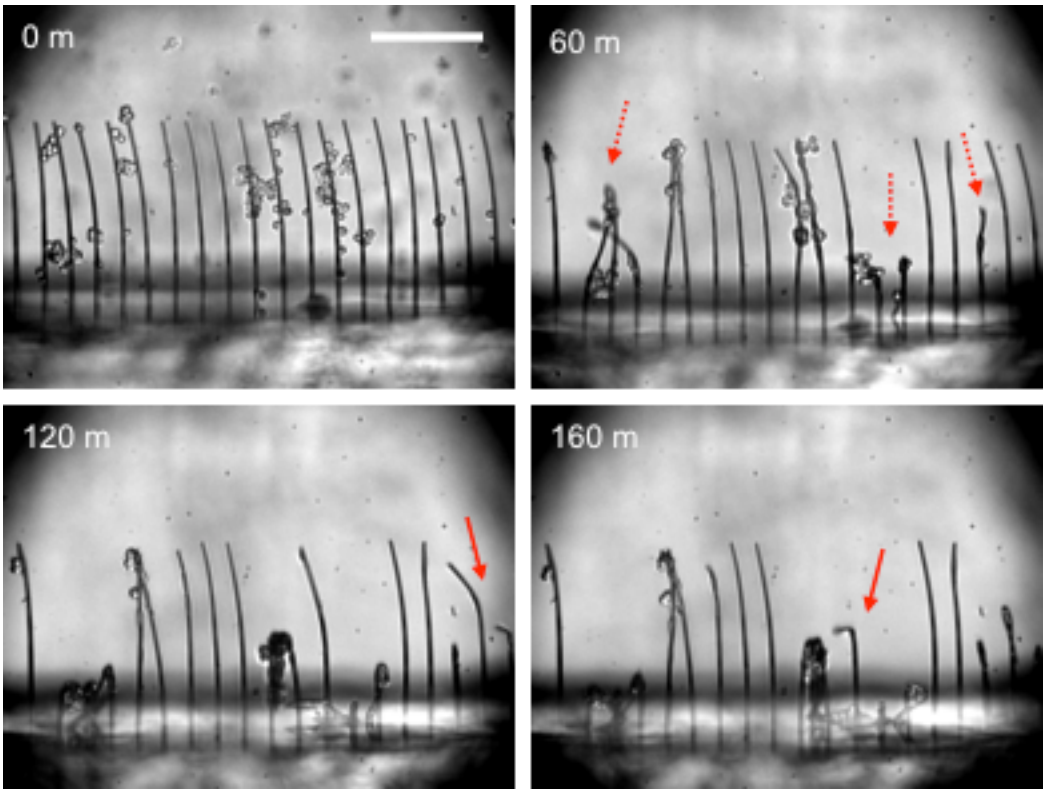

Figure 7.11. Time-lapse microscope images of fiber buckling for 6-µm fibers. Black-line arrows indicate cells right before cell adhesion, and white-line arrows indicate cells on buckled fibers. Dashed-line arrows indicate the beginning points of buckling by multiple cells, and solid line arrows indicate the beginning points of buckling by single cells. The numbers in the top-left corner indicate the time. Scale bars: 200 µm.

7.5.4. Discussion

We estimated individual cell mediated contractile forces by considering columnar buckling of cantilever fiber scaffolds. This procedure allows more accurate calculation due to reduced experimental assumptions compared to previous studies on two-dimensional continuous surfaces or pin-array detectors and three-dimensional hydrogel or scaffolds. Measurement of cell traction forces using two-dimensional flexible materials can yield the force distribution at specific focal adhesions within a single cell. However, it requires sophisticated analysis and does not reveal cell response to a fibrillar three-dimensional environment due to differences in cell morphology, cytoskeleton organization and focal adhesion strength [125, 135, 136]. Measurement of the forces on three-dimensional hydrogel scaffolds is more directly connected to in vivo cellular microenvironment and tissue engineering. However, the respective macroscopic force involves significant assumptions: (1) cell density does not change during measurement; (2) all cells contribute equally to force generation at the same time; (3) the force direction is identical; and (4) the material is isotropic. Due to these assumptions, the forces obtained on three-dimensional materials can only provide lower bounds to single cell contractile forces. Recently, a new method for measuring individual cell mediated contractile forces using a single strut of collagen-glycosaminoglycan (CG) scaffolds was reported by Harley et al. This microscopic method relaxes experimental assumptions [135], but still cannot produce accurate force measurement since it is limited to specific scaffold structure. To address these concerns, we used single-standing fiber columns with varying diameters to control mechanical properties of the fibers and measure the contractile forces exerted by individual cells. Because of the microscopic observation of the simple, columnar fiber structure, the experimental assumptions and calculation errors can be reduced. Individual fibroblasts could deform fiber scaffolds that require up to 200 nN of eccentric critical load for buckling. This value represents an upper bound of the contractile force generated by a single cell, that is lower than the upper bound force (450 nN) suggested by Harley et al [135]. Our results provide enhanced evidence in support of their measurement of contractile forces of individual cells, since they suggested an upper bound (450 nN) without measuring forces in the intermediate range between 50 nN and 450 nN.

The contractile force measurement is important since the forces generated by cells depend on cell morphology that is in turn influenced by the supporting three-dimensional material structure. It was reported that most of forces are generated by cells upon attachment and are associated with changes in cell shape [143]. In addition, increased cell spreading enhances stress fiber formation and cytoskeletal tension, while the size of focal adhesions has a positive correlation to the forces [129]. Fibroblast cellular morphology on a single fiber structure is much different from that on two-dimensional surfaces. In this regard, cells on a single fiber become elongated and are partially wrapped around the fiber with a straight cytoskeleton shape [136]. Due to the one-dimensional, elongated cell morphology in the present study, the forces exerted by the cells do not disperse but can effectively buckle the fiber columns. The fiber buckling occurred on fibers smaller than 8.4 μm in diameter. Thinner fibers were buckled earlier than thicker fibers; e.g. 5-μm diameter fibers buckled within 30 min after cell seeding, and the other fibers buckled

within 120-160 min after cell seeding. The seeded cells attach to the fiber and start spreading within 30 min. It is noted that traction force applying eccentric load during adhesion suffices for buckling the 5-μm fibers. The eccentric critical load for the 5-μm diameter fiber buckling is 30 nN (Table 1). After the cells spread completely, thicker fibers buckled by cell locomotion and contraction. Previous studies of macroscopic measurement using collagen gel or scaffolds reported that the forces generated by seeded cells tend to increase rapidly in the early phase, reaching an asymptotic limit [121, 132, 143]. In the early stage of wound healing, traction forces generated by cell locomotion are sufficient for wound closure and stimulate fibroblasts to develop stress lines via application of mechanical stress [121, 144]. This study suggests that single cell-mediated forces in the early stage are ~30-63 nN within ~30 min and the force increase up to ~116-200 nN within ~3 hours after cell seeding.

The effect of multiple cells in generating contractile forces was also investigated. Freyman et al. reported that contractile forces scaled with respect to the population of fibroblasts within a CG scaffold were linearly proportional to the number of cells and suggested that fibroblasts could exert forces independent of the presence of other cells [132]. In our study, however, the contractile force did not increase as the number of cells increased. Fibers of 8.4-μm diameter deformed, but thicker fibers did not buckle, although they were deformed by cells suspended between adjacent fibers, in which case forces normal to the fiber axis were applied. A single fiber does not offer sufficient area to accommodate adhesion of multiple cells, resulting that the cell-mediated forces do not apply on the same surface of the fibers. Consequently, contractile forces generated by multiple cells cannot induce buckling of single fibers effectively in this study.

The difference between microscopic and macroscopic measurement does not only refer to the multiple cell effect but also to the magnitude of the force generated by individual cells. Here, the fibers subjected to eccentric critical loads in the range of 30-116 nN deformed easily. Such forces are not much different than the value of 41 nN quoted by Harley et al [135]. However, forces calculated by macroscopic measurements are of the order of 1 nN, which is much smaller than our and Harley et al.'s results [132, 143]. Forces are not generated simultaneously and in the same direction as the cell density changes in macroscopic measurement tools. Therefore, it is worth noting that macroscopic measurements yield lower bounds of cell contractility, but microscopic measurement provides upper bounds for the applied forces. In particular, this study suggests that the maximum contractile force generated by individual fibroblasts is ~200 nN.

7.6. Conclusion

In this chapter, we examined cell contractility on self-standing fiber scaffolds fabricated by using femtosecond laser induced two-photon polymerization. Contractile forces generated by individual cells were calculated by using columnar buckling analysis. The simple structure of the fiber scaffolds facilitated microscopic observation of cell contraction. Experimental assumptions and calculation errors could be reduced compared to previous studies. The force magnitude obtained by this investigation offers an upper bound of contractility of individual cells that can be useful in order to design bioactive scaffolds for tissue engineering, complementing the lower bound suggested by macroscopic measurement representing multiple cells within three-dimensional structures. This method can also be used to understand contractile forces generated by various cells in more detail with respect to wound healing, and improve contractility of cells for pathological wound healing and therapeutic strategies. The fiber scaffolds and two-photon polymerization technique also can be used to fabricate precisely defined three-dimensional (3D) filamentous matrices of artificial tissue scaffolds and to study cell and 3D material interaction. Despite excellent initial progress in understanding cell behavior in 2D, there remain many deficiencies in current materials science and fabrication technologies, which cannot emulate the 3D filamentous nature of natural matrices, and ultimately real tissues. Gaining a deeper understanding of how cell fate is governed and controlled requires the development of advanced 3D materials systems that can emulate the complex properties of natural cellular microenvironments.

Chapter 8

Conclusions and outlook

Ultrashort pulse lasers have proven to be efficient tools for precise micromachining applications due to advantages such as reduced heat and shock affected zones, as well as sharp and significantly lower material modification, and ablation thresholds. In particular, the nonlinear absorption of the short pulses into dielectric materials offers a unique advantage in the fabrication of three-dimensional structures. This thesis demonstrates micro/nano and 2D/3D structures fabricated by femtosecond-laser-induced two-photon polymerization (2PP) and multiphoton laser ablation lithography methods and their application for control of cell adhesion and migration. The patterned surfaces and fibrous matrices demonstrated in this thesis can also be used for further regulation of cell fate, e.g. stem cell differentiation into specific lineage. We need a detailed understanding of the interaction mechanism of short laser pulses with dielectric materials, e.g. polymer and glass in order to use utilize them for producing biomaterials. By the same token we need to understand the interaction mechanism of cell with the engineered biomaterial surface in order to deliberately regulate the cell behavior. In this final chapter, we summarize key results of previous chapters and suggest some ideas for future investigation.

Cells migrate to fulfill their duties or survive. Therefore, we can control cell migration by regulating their environment chemically or physically. For example, a concentration gradient of chemoattractants can induce chemotaxis, a density gradient of ECM proteins can induce haptotaxis, a gradient of matrix rigidity can cause durotaxis, and a spatial gradient of topographical patterns can guide directional migration that is demonstrated in this thesis.

Microscale ridge/groove patterns and fiber scaffolds were fabricated by the 2PP and used to regulate cell migration and motility and measure contractile forces generated by the cell migration. The 2PP process can be confined to cure photopolymerizing resins only near the laser focal volume, hence enabling fabrication of arbitrary three-dimensional structures. From a fundamental research perpective it is important to unveil the interaction of cells with topographical surfaces of single steps using parallel and

orthogonal ridge patterns with varying height ranging from 200 nm to 5 μm. The threshold obstacle height for cell alignment on the parallel and orthogonal ridge patterns was found near ~1 μm.

Ridge patterns have been known to direct bidirectional cell migration along the walls and hence enhance migration speed as well as cell alignment. However, there had been no report concerning cell migration on mesh patterns with various anisotropy. We fabricated 1:1, 1:2, 1:4 aspect ratio grid patterns as well as parallel ridge patterns with 3- and 10-μm in height and three different spacing between longer side ridges, e.g. 12, 16 and 24 μm. These topographical patterns influenced cell morphology and motility multidirectionally, providing contact guidance with continual stimulation. We found that cells cultured on parallel line patterns and 1:4 grid patterns can be aligned and biased via the topography to migrate along the parallel ridges or the longer side ridges, while no alignment and directional migration on 1:1 and 1:2 grid patterns. Interestingly, the cell migration speed can be enhanced by the grid patterns since the longer side ridges play a role of contact guidance and the shorter side ridges supply anchorage points.

Microscale patterns are powerful cues to control cell behavior. However, they have limitation to independently control the size and the distribution of the cell adhesive domains and the ligand density. We fabricated nanopit patterned surfaces with spatial gradient by multiphoton laser ablation lithography to demonstrate the gradient force generated by the nanoscale chemical and topographical patterns. Femtosecond laser ablation with various objective lenses for polymer thin film with various thickness and fused quartz had been conducted to optimize the process and fabricate the desired substrate designs. Nanoscale chemical patterns can cause the density gradient of cell adhesion ligands that guide cell migration towards higher density of the ligands. Nanoscale topographical patterns can generate spatial gradients of the nanopit array that can realize force gradient generated by the nanoscale features. Higher density of the nanopits repels cell adhesion and the gradient of the nanopit spacing can direct cell migration. In this thesis, the dimensions of the nanopits were also studied.

When the cells migrate, contractile force generated by the cells is needed to move the cell body forward. Through influencing cell migration and interaction with biomaterial surfaces, the contractile force is important for the wound healing process and the artificial tissue scaffolds design. The contractile force generated by individual fibroblasts was measured by fiber scaffolds fabricated by the 2PP process. Experimental assumptions and calculation errors could be reduced by adopting a columnar buckling model on individual, standing fiber scaffolds. Via quantifying eccentric critical loads for the buckling of fibers with various diameters, a force magnitude of approximately 200 nN is suggested as upper bound of the contractile force exerted by a single cell.

Among of the multitude of cell behavior modes, adhesion, alignment, migration and contraction were examined by micro/nanoscale laser-induced patterned surface in this thesis. Further studies would be expected to control other important cell tendencies, especially control and dictate stem cell fate. We should be able to attempt to create nanoscale chemical or topographical surfaces that can define peptide ligand density and ligand distribution, as well as control the spatial arrangements of focal adhesions on nanometer length scale. These culture surfaces will have a number of conceivable applications in the fields of biotechnology, dentistry, and medicine. First, because they allow focal adhesion distribution, they are invaluable as experimental platforms for the

study of cell shape/gene expression hierarchies. Second, since these surfaces will enable fundamental control of cell differentiation and proliferation, we ultimately hope to map the nanopatterning technique we developed to the surface of biomaterials, such as dental and medical implants, in order to control cell behavior at the biomaterial interface.

Cells exhibit a number of behaviors and fates, in the case of stem cells, self-renewal and differentiation, that are interconnected, orchestrated and integrated throughout development and into adulthood within multicellular organisms. However, these behaviors and fate decisions are controlled in large part by the 3D niches surrounding cells, which are structurally complex material microenvironments that present cells with numerous chemical and physical cues in the form of soluble factors, extracellular matrix (ECM), and surrounding cells. We will also be able to use the 2PP process to create a cohort of three-dimensional filamentous matrices that regulate the structural organization of stem cells and their function. Our approach offers a number of significant advances beyond current practice including: unprecedented control of matrix fiber architecture and dimensions, and a 3D filamentous matrix with independently tunable elastic modulus and biological content.

References

[1] Vogel V, Sheetz M. Local force and geometry sensing regulate cell functions. Nature Reviews Molecular Cell Biology. 2006;7:265-75.
[2] Curtis A, Wilkinson C. Topographical control of cells. Biomaterials. 1997;18:1573-83.
[3] Clark P, Connolly P, Curtis ASG, Dow JAT, Wilkinson CDW. Topographical Control of Cell Behavior .2. Multiple Grooved Substrata. Development. 1990;108:635-44.
[4] Kaiser JP, Reinmann A, Bruinink A. The effect of topographic characteristics on cell migration velocity. Biomaterials. 2006;27:5230-41.
[5] Chen CS, Mrksich M, Huang S, Whitesides GM, Ingber DE. Geometric control of cell life and death. Science. 1997;276:1425-8.
[6] Dalby MJ, Gadegaard N, Tare R, Andar A, Riehle MO, Herzyk P, et al. The control of human mesenchymal cell differentiation using nanoscale symmetry and disorder. Nature Materials. 2007;6:997-1003.
[7] Maniotis AJ, Chen CS, Ingber DE. Demonstration of mechanical connections between integrins cytoskeletal filaments, and nucleoplasm that stabilize nuclear structure. Proceedings of the National Academy of Sciences of the United States of America. 1997;94:849-54.
[8] Bidwell JP, Vanwijnen AJ, Fey EG, Dworetzky S, Penman S, Stein JL, et al. Osteocalcin Gene Promoter-Binding Factors Are Tissue-Specific Nuclear Matrix Components. Proceedings of the National Academy of Sciences of the United States of America. 1993;90:3162-6.
[9] Wang N, Tytell JD, Ingber DE. Mechanotransduction at a distance: mechanically coupling the extracellular matrix with the nucleus. Nature Reviews Molecular Cell Biology. 2009;10:75-82.
[10] Kim DH, Wong PK, Park J, Levchenko A, Sun Y. Microengineered Platforms for Cell Mechanobiology. Annual Review of Biomedical Engineering. 2009;11:203-33.
[11] Lom B, Healy KE, Hockberger PE. A Versatile Technique for Patterning Biomolecules onto Glass Coverslips. Journal of Neuroscience Methods. 1993;50:385-97.
[12] Kumar A, Whitesides GM. Features of gold having micrometer to centimeter dimensions can be formed through a combination of stamping with an elastomeric stamp and an alkanethiol ``ink'' followed by chemical etching. Applied Physics Letters. 1993;63:2002-4.
[13] Chou SY, Krauss PR, Renstrom PJ. Imprint Lithography with 25-Nanometer Resolution. Science. 1996;272:85-7.
[14] Menon R, Patel A, Gil D, Smith HI. Maskless lithography. Materials Today. 2005;8:26-33.
[15] Piner RD, Zhu J, Xu F, Hong S, Mirkin CA. "Dip-Pen" Nanolithography. Science. 1999;283:661-3.
[16] Chimmalgi A, et al. Near-field scanning optical microscopy based nanostructuring of glass. Journal of Physics: Conference Series. 2007;59:285.
[17] Lee JW, Lan PX, Kim B, Lim G, Cho DW. 3D scaffold fabrication with PPF/DEF using micro-stereolithography. Microelectronic Engineering. 2007;84:1702-5.
[18] Yeong WY, Chua CK, Leong KF, Chandrasekaran M. Rapid prototyping in tissue engineering: challenges and potential. Trends Biotechnol. 2004;22:643-52.

[19] Doraiswamy A, Patz T, Narayan R, Chichkov B, Ovsianikov A, Houbertz R, et al. Biocompatlbility of CAD/CAM ORMOCER polymer scaffold structures. Boston, MA, United States: Materials Research Society, Warrendale, PA 15086, United States; 2005. p. 51-6.
[20] Doraiswamy A, Jin C, Narayan RJ, Mageswaran P, Mente P, Modi R, et al. Two photon induced polymerization of organic-inorganic hybrid biomaterials for microstructured medical devices. Acta Biomater. 2006;2:267-75.
[21] Kawata S, Sun HB, Tanaka T, Takada K. Finer features for functional microdevices - Micromachines can be created with higher resolution using two-photon absorption. Nature. 2001;412:697-8.
[22] Lauffenburger DA, Horwitz AF. Cell migration: a physically integrated molecular process. Cell. 1996;84:359-69.
[23] Brunette DM. The effect of surface topography on cell migration and adhesion. In: Ratner BD, editor. Surface characterization of biomaterials. Amsterdam: Elsevier Science Publishers; 1988. p. 203-17.
[24] Flemming RG, Murphy CJ, Abrams GA, Goodman SL, Nealey PF. Effects of synthetic micro- and nano-structured surfaces on cell behavior. Biomaterials. 1999;20:573-88.
[25] Lim JY, Donahue HJ. Cell sensing and response to micro- and nanostructured surfaces produced by chemical and topographic patterning. Tissue Engineering. 2007;13:1879-91.
[26] Sheetz MP, Felsenfeld DP, Galbraith CG. Cell migration: regulation of force on extracellular-matrix-integrin complexes. Trends Cell Biol. 1998;8:51-4.
[27] Park S, Wolanin PM, Yuzbashyan EA, Silberzan P, Stock JB, Austin RH. Motion to form a quorum. Science. 2003;301:188-.
[28] Discher DE, Janmey P, Wang YL. Tissue cells feel and respond to the stiffness of their substrate. Science. 2005;310:1139-43.
[29] Li S, Guan JL, Chien S. Biochemistry and biomechanics of cell motility. Annual Review of Biomedical Engineering. 2005;7:105-50.
[30] Jeon H, Lee Y, Jin S, Koo S, Lee CS, Yoo JY. Quantitative analysis of single bacterial chemotaxis using a linear concentration gradient microchannel. Biomedical Microdevices. 2009;11:1135-43.
[31] Ahmed T, Shimizu TS, Stocker R. Microfluidics for bacterial chemotaxis. Integrative Biology. 2010;2:604-29.
[32] Jeon NL, Baskaran H, Dertinger SKW, Whitesides GM, Van de Water L, Toner M. Neutrophil chemotaxis in linear and complex gradients of interleukin-8 formed in a microfabricated device. Nature Biotechnology. 2002;20:826-30.
[33] Yamada KM, Geiger B. Molecular interactions in cell adhesion complexes. Current Opinion in Cell Biology. 1997;9:76-85.
[34] Burridge K, ChrzanowskaWodnicka M. Focal adhesions, contractility, and signaling. Annu Rev Cell Dev Biol. 1996;12:463-518.
[35] Dimilla PA, Stone JA, Quinn JA, Albelda SM, Lauffenburger DA. Maximal migration of human smooth-muscle cells on fibronectin and type-IV collagen occurs at an intermediate attachment strength. J Cell Biol. 1993;122:729-37.
[36] Carter SB. Haptotaxis and Mechanism of Cell Motility. Nature. 1967;213:256-&.

[37] Engler AJ, Sen S, Sweeney HL, Discher DE. Matrix elasticity directs stem cell lineage specification. Cell. 2006;126:677-89.
[38] Lo CM, Wang HB, Dembo M, Wang YL. Cell movement is guided by the rigidity of the substrate. Biophysical Journal. 2000;79:144-52.
[39] Clark P, Connolly P, Curtis ASG, Dow JAT, Wilkinson CDW. Topographical control of cell behavior .1. simple step cues. Development. 1987;99:439-48.
[40] Meyle J, Gultig K, Brich M, Hammerle H, Nisch W. Contact guidance of fibroblasts on biomaterial surfaces. J Mater Sci-Mater Med. 1994;5:463-6.
[41] Mai JY, Sun C, Li S, Zhang X. A microfabricated platform probing cytoskeleton dynamics using multidirectional topographical cues. Biomed Microdevices. 2007;9:523-31.
[42] Kurpinski K, Chu J, Hashi C, Li S. Anisotropic mechanosensing by mesenchymal stem cells. Proceedings of the National Academy of Sciences of the United States of America. 2006;103:16095-100.
[43] Folch A, Toner M. Microengineering of cellular interactions. Annual Review of Biomedical Engineering. 2000;2:227-+.
[44] Schmidt RC, Healy KE. Controlling biological interfaces on the nanometer length scale. Journal of Biomedical Materials Research Part A. 2009;90A:1252-61.
[45] Kim DH, Lee H, Lee YK, Nam JM, Levchenko A. Biomimetic nanopatterns as enabling tools for analysis and control of live cells. Advanced Materials. 2010;22:4551-66.
[46] Lim JH, Ginger DS, Lee KB, Heo J, Nam JM, Mirkin CA. Direct-write dip-pen nanolithography of proteins on modified silicon oxide surfaces. Angewandte Chemie-International Edition. 2003;42:2309-12.
[47] Ruiz SA, Chen CS. Microcontact printing: A tool to pattern. Soft Matter. 2007;3:168-77.
[48] Grigoropoulos CP. Transport in Laser Microfabrication: Fundamentals and Applications. New York: Cambridge University Press; 2009.
[49] Keldysh LV. Ionization in Field of a Strong Electromagnetic Wave. Soviet Physics Jetp-Ussr. 1965;20:1307-&.
[50] Stuart BC, Feit MD, Herman S, Rubenchik AM, Shore BW, Perry MD. Nanosecond-to-femtosecond laser-induced breakdown in dielectrics. Phys Rev B. 1996;53:1749-61.
[51] Kelley PL. Self-Focusing of Optical Beams. Physical Review Letters. 1965;15:1005-&.
[52] Stuart BC, Feit MD, Rubenchik AM, Shore BW, Perry MD. Laser-induced damage in dielectrics with nanosecond to subpicosecond pulses. Physical Review Letters. 1995;74:2248-51.
[53] Kawata S, Sun HB, Tanaka T, Takada K. Finer features for functional microdevices - Micromachines can be created with higher resolution using two-photon absorption. Nature. 2001;412:697-8.
[54] Maruo S, Nakamura O, Kawata S. Three-dimensional microfabrication with two-photon-absorbed photopolymerization. Optics Letters. 1997;22:132-4.
[55] Cumpston BH, Ananthavel SP, Barlow S, Dyer DL, Ehrlich JE, Erskine LL, et al. Two-photon polymerization initiators for three-dimensional optical data storage and microfabrication. Nature. 1999;398:51-4.

[56] Narayan RJ, Doraiswamy A, Chrisey DB, Chichkov BN. Medical prototyping using two photon polymerization. Materials Today. 2010;13:42-8.
[57] Higgins DA, Everett TA, Xie AF, Forman SM, Ito T. High-resolution direct-write multiphoton photolithography in poly(methylmethacrylate) films. Appl Phys Lett. 2006;88:-.
[58] Ibrahim S, Higgins DA, Ito T. Direct-write multiphoton photolithography: A systematic study of the etching Behaviors in various commercial polymers. Langmuir. 2007;23:12406-12.
[59] Chichkov BN, Momma C, Nolte S, vonAlvensleben F, Tunnermann A. Femtosecond, picosecond and nanosecond laser ablation of solids. Appl Phys A. 1996;63:109-15.
[60] Korte F, Serbin J, Koch J, Egbert A, Fallnich C, Ostendorf A, et al. Towards nanostructuring with femtosecond laser pulses. Appl Phys A-Mater Sci Process. 2003;77:229-35.
[61] Hwang DJ, Grigoropoulos CP, Choi TY. Efficiency of silicon micromachining by femtosecond laser pulses in ambient air. Journal Of Applied Physics. 2006;99.
[62] Hartmann N, Franzka S, Koch J, Ostendorf A, Chichkov BN. Subwavelength patterning of alkylsiloxane monolayers via nonlinear processing with single femtosecond laser pulses. Appl Phys Lett. 2008;92:3.
[63] Hwang DJ, Choi TY, Grigoropoulos CP. Liquid-assisted femtosecond laser drilling of straight and three-dimensional microchannels in glass. Applied Physics a-Materials Science & Processing. 2004;79:605-12.
[64] Kim M, Hwang DJ, Jeon H, Hiromatsu K, Grigoropoulos CP. Single cell detection using a glass-based optofluidic device fabricated by femtosecond laser pulses. Lab on a Chip. 2009;9:311-8.
[65] Jeon H, Hidai H, Hwang DJ, Grigoropoulos CP. Fabrication of arbitrary polymer patterns for cell study by two-photon polymerization process. Journal of Biomedical Materials Research Part A. 2010;93A:56-66.
[66] Revzin A, Sekine K, Sin A, Tompkins RG, Toner M. Development of a microfabricated cytometry platform for characterization and sorting of individual leukocytes. Lab on a Chip. 2005;5:30-7.
[67] Dusseiller MR, Smith ML, Vogel V, Textor M. Microfabricated three-dimensional environments for single cell studies Biointerphases. 2006;1:1-4.
[68] Ochsner M, Dusseiller MR, Grandin HM, Luna-Morris S, Textor M, Vogel V, et al. Micro-well arrays for 3D shape control and high resolution analysis of single cells. Lab on a Chip. 2007;7:1074-7.
[69] Di Carlo D, Lee LP. Dynamic single-cell analysis for quantitative biology. Anal Chem. 2006;78:7918-25.
[70] Rettig JR, Folch A. Large-scale single-cell trapping and imaging using microwell arrays. Anal Chem. 2005;77:5628-34.
[71] Ball MD, Prendergast U, O'Connell C, Sherlock R. Comparison of cell interactions with laser machined micron- and nanoscale features in polymer. Experimental and Molecular Pathology. 2007;82:130-4.
[72] Yoshinari M, Matsuzaka K, Inoue T, Oda Y, Shimono M. Effects of multigrooved surfaces on fibroblast behavior. Journal of Biomedical Materials Research Part A. 2003;65A:359-68.

[73] Rebollar E, Frischauf I, Olbrich M, Peterbauer T, Hering S, Preiner J, et al. Proliferation of aligned mammalian cells on laser-nanostructured polystyrene. Biomaterials. 2008;29:1796-806.
[74] Meyle J, Gultig K, Nisch W. Variation in contact guidance by human-cells on a microstructured surface. Journal of Biomedical Materials Research. 1995;29:81-8.
[75] Diehl KA, Foley JD, Nealey PF, Murphy CJ. Nanoscale topography modulates corneal epithelial cell migration. Journal of Biomedical Materials Research Part A. 2005;75A:603-11.
[76] Hidai H, Hwang DJ, Grigoropoulos CP. Self-grown fiber fabrication by two-photon photopolymerization. Appl Phys A-Mater Sci Process. 2008;93:443-5.
[77] Teh WH, Durig U, Salis G, Harbers R, Drechsler U, Mahrt RF, et al. SU-8 for real three-dimensional subdiffraction-limit two-photon microfabrication. Appl Phys Lett. 2004;84:4095-7.
[78] Frisken SJ. Light-induced optical waveguide uptapers. Optics Letters. 1993;18:1035-7.
[79] Kagami M, Yamashita T, Ito H. Light-induced self-written three-dimensional optical waveguide. Appl Phys Lett. 2001;79:1079-81.
[80] Shoji S, Kawata S. Optically-induced growth of fiber patterns into a photopolymerizable resin. Appl Phys Lett. 1999;75:737-9.
[81] Kewitsch AS, Yariv A. Self-focusing and self-trapping of optical beams upon photopolymerization. Optics Letters. 1996;21:24-6.
[82] Shoji S, Kawata S, Sukhorukov AA, Kivshar YS. Self-written waveguides in photopolymerizable resins. Optics Letters. 2002;27:185-7.
[83] Chen M, Patra PK, Warner SB, Bhowmick S. Role of fiber diameter in adhesion and proliferation of NIH 3T3 fibroblast on electrospun polycaprolactone scaffolds. Tissue Engineering. 2007;13:579-87.
[84] denBraber ET, deRuijter JE, Ginsel LA, vonRecum AF, Jansen JA. Quantitative analysis of fibroblast morphology on microgrooved surfaces with various groove and ridge dimensions. Biomaterials. 1996;17:2037-44.
[85] Ji Y, Ghosh K, Shu XZ, Li BQ, Sokolov JC, Prestwich GD, et al. Electrospun three-dimensional hyaluronic acid nanofibrous scaffolds. Biomaterials. 2006;27:3782-92.
[86] Haas KH. Hybrid inorganic-organic polymers based on organically modified Si-alkoxides. Adv Eng Mater. 2000;2:571-82.
[87] Schlie S, Ngezahayo A, Ovsianikov A, Fabian T, Kolb HA, Haferkamp H, et al. Three-dimensional cell growth on structures fabricated from ORMOCER (R) by two-photon polymerization technique. Journal of Biomaterials Applications. 2007;22:275-87.
[88] Houbertz R, Declerck P, Passinger S, Ovsianikov A, Serbin J, Chichkov BN. Investigations on the generation of photonic crystals using two-photon polymerization (2PP) of inorganic - organic hybrid polymers with ultra-short laser pulses. Physica Status Solidi a-Applications and Materials Science. 2007;204:3662-75.
[89] Gumpenberger T, Heitz J, Bauerle D, Kahr H, Graz I, Romanin C, et al. Adhesion and proliferation of human endothelial cells on photochemically modified polytetrafluoroethylene. Biomaterials. 2003;24:5139-44.
[90] Sun HB, Tanaka T, Kawata S. Three-dimensional focal spots related to two-photon excitation. Appl Phys Lett. 2002;80:3673-5.

[91] Jeon H, Hidai H, Hwang DJ, Healy KE, Grigoropoulos CP. The effect of micronscale anisotropic cross patterns on fibroblast migration. Biomaterials. 2010;31:4286-95.
[92] Thomas CH, Collier JH, Sfeir CS, Healy KE. Engineering gene expression and protein synthesis by modulation of nuclear shape. Proc Natl Acad Sci U S A. 2002;99:1972-7.
[93] Nelson CM, Jean RP, Tan JL, Liu WF, Sniadecki NJ, Spector AA, et al. Emergent patterns of growth controlled by multicellular form and mechanics. Proc Natl Acad Sci U S A. 2005;102:11594-9.
[94] Lee KY, Alsberg E, Hsiong S, Comisar W, Linderman J, Ziff R, et al. Nanoscale adhesion ligand organization regulates osteoblast proliferation and differentiation. Nano Lett. 2004;4:1501-6.
[95] Arnold M, Cavalcanti-Adam EA, Glass R, Blummel J, Eck W, Kantlehner M, et al. Activation of integrin function by nanopatterned adhesive interfaces. ChemPhysChem. 2004;5:383-8.
[96] Brunette DM, Hamilton DW, Chehroudi B. Comparative response of epithelial cells and osteoblasts to microfabricated tapered pit topographies in vitro and in vivo. Biomaterials. 2007;28:2281-93.
[97] Lim JY, Hansen JC, Siedlecki CA, Runt J, Donahue HJ. Human foetal osteoblastic cell response to polymer-demixed nanotopographic interfaces. J R Soc Interface. 2005;2:97-108.
[98] Yim EKF, Reano RM, Pang SW, Yee AF, Chen CS, Leong KW. Nanopattern-induced changes in morphology and motility of smooth muscle cells. Biomaterials. 2005;26:5405-13.
[99] Kim DH, Seo CH, Han K, Kwon KW, Levchenko A, Suh KY. Guided cell migration on microtextured substrates with variable local density and anisotropy. Adv Funct Mater. 2009;19:1579-86.
[100] Shreiber DI, Barocas VH, Tranquillo RT. Temporal variations in cell migration and traction during fibroblast-mediated gel compaction. Biophys J. 2003;84:4102-14.
[101] Dickinson RB, Tranquillo RT. Optimal estimation of cell movement indexes from the statistical analysis of cell tracking data. Aiche J. 1993;39:1995-2010.
[102] Tan J, Saltzman WM. Topographical control of human neutrophil motility on micropatterned materials with various surface chemistry. Biomaterials. 2002;23:3215-25.
[103] Stokes CL, Lauffenburger DA, Williams SK. Migration of individual microvessel endothelial cells stochastic model and parameter measurement. J Cell Sci. 1991;99:419-30.
[104] Li S, Bhatia S, Hu YL, Shin YT, Li YS, Usami S, et al. Effects of morphological patterning on endothelial cell migration. Biorheology. 2001;38:101-8.
[105] Palecek SP, Horwitz AF, Lauffenburger DA. Kinetic model for integrin-mediated adhesion release during cell migration. Ann Biomed Eng. 1999;27:219-35.
[106] Stevens MM, George JH. Exploring and engineering the cell surface interface. Science. 2005;310:1135-8.
[107] Bettinger CJ, Langer R, Borenstein JT. Engineering Substrate Topography at the Micro- and Nanoscale to Control Cell Function. Angewandte Chemie-International Edition. 2009;48:5406-15.

[108] Biggs MJP, Richards RG, Gadegaard N, Wilkinson CDW, Dalby MJ. The effects of nanoscale pits on primary human osteoblast adhesion formation and cellular spreading. Journal of Materials Science-Materials in Medicine. 2007;18:399-404.
[109] Chou LS, Firth JD, Uitto VJ, Brunette DM. Substratum Surface-Topography Alters Cell-Shape and Regulates Fibronectin Messenger-Rna Level, Messenger-Rna Stability, Secretion and Assembly in Human Fibroblasts. Journal of Cell Science. 1995;108:1563-73.
[110] Lee KB, Park SJ, Mirkin CA, Smith JC, Mrksich M. Protein nanoarrays generated by dip-pen nanolithography. Science. 2002;295:1702-5.
[111] Hwang DJ, Grigoropoulos CP, Choi TY. Efficiency of silicon micromachining by femtosecond laser pulses in ambient air. J Appl Phys. 2006;99:-.
[112] Ma HW, Li DJ, Sheng X, Zhao B, Chilkoti A. Protein-resistant polymer coatings on silicon oxide by surface-initiated atom transfer radical polymerization. Langmuir. 2006;22:3751-6.
[113] Liu JM. Simple Technique for Measurements of Pulsed Gaussian-Beam Spot Sizes. Optics Letters. 1982;7:196-8.
[114] Ben-Yakar A, Byer RL. Femtosecond laser ablation properties of borosilicate glass. J Appl Phys. 2004;96:5316-23.
[115] Sanner N, Uteza O, Bussiere B, Coustillier G, Leray A, Itina T, et al. Measurement of femtosecond laser-induced damage and ablation thresholds in dielectrics. Appl Phys A-Mater Sci Process. 2009;94:889-97.
[116] Fardel R, Nagel M, Lippert T, Nuesch F, Wokaun A, Luk'yanchuk BS. Influence of thermal diffusion on the laser ablation of thin polymer films. Appl Phys A-Mater Sci Process. 2008;90:661-7.
[117] Kunzler TP, Huwiler C, Drobek T, Voros J, Spencer ND. Systematic study of osteoblast response to nanotopography by means of nanoparticle-density gradients. Biomaterials. 2007;28:5000-6.
[118] Zimmerberg J, Kozlov MM. How proteins produce cellular membrane curvature. Nature Reviews Molecular Cell Biology. 2006;7:9-19.
[119] Jeon H, Kim E, Grigoropoulos CP. Measurement of contractile forces generated by individual fibroblasts on self-standing fiber scaffolds. Biomedical Microdevices. 2011;13:107-15.
[120] Grinnell F. Fibroblasts, myofibroblasts, and wound contraction. J Cell Biol. 1994;124:401-4.
[121] Tomasek JJ, Gabbiani G, Hinz B, Chaponnier C, Brown RA. Myofibroblasts and mechano-regulation of connective tissue remodelling. Nat Rev Mol Cell Biol. 2002;3:349-63.
[122] Yannas IV. Tissue and organ regeneration in adults. New York: Springer; 2001.
[123] Katoh K, Kano Y, Amano M, Onishi H, Kaibuchi K, Fujiwara K. Rho-kinase-mediated contraction of isolated stress fibers. J Cell Biol. 2001;153:569-83.
[124] Harris AK, Stopak D, Wild P. Fibroblast traction as a mechanism for collagen morphogenesis. Nature. 1981;290:249-51.
[125] Beningo KA, Wang YL. Flexible substrata for the detection of cellular traction forces. Trends Cell Biol. 2002;12:79-84.
[126] Addae-Mensah KA, Wikswo JP. Measurement techniques for cellular biomechanics in vitro. Exp Biol Med. 2008;233:792-809.

[127] Balaban NQ, Schwarz US, Riveline D, Goichberg P, Tzur G, Sabanay I, et al. Force and focal adhesion assembly: a close relationship studied using elastic micropatterned substrates. Nat Cell Biol. 2001;3:466-72.
[128] Galbraith CG, Sheetz MP. A micromachined device provides a new bend on fibroblast traction forces. Proc Natl Acad Sci U S A. 1997;94:9114-8.
[129] Tan JL, Tien J, Pirone DM, Gray DS, Bhadriraju K, Chen CS. Cells lying on a bed of microneedles: an approach to isolate mechanical force. Proc Natl Acad Sci U S A. 2003;100:1484-9.
[130] Kolodney MS, Wysolmerski RB. Isometric contraction by fibroblasts and endothelial cells in tissue culture : a quantitative study. J Cell Biol. 1992;117:73-82.
[131] Delvoye P, Wiliquet P, Leveque JL, Nusgens BV, Lapiere CM. Measurement of mechanical forces generated by skin fibroblasts embedded in a 3-dimensional collagen gel. J Invest Dermatol. 1991;97:898-902.
[132] Freyman TM, Yannas IV, Yokoo R, Gibson LJ. Fibroblast contraction of a collagen-GAG matrix. Biomaterials. 2001;22:2883-91.
[133] Grinnell F. Fibroblast-collagen-matrix contraction: growth-factor signalling and mechanical loading. Trends Cell Biol. 2000;10:362-5.
[134] Zahalak GI, Wagenseil JE, Wakatsuki T, Elson EL. A cell-based constitutive relation for bio-artificial tissues. Biophys J. 2000;79:2369-81.
[135] Harley BA, Freyman TM, Wong MQ, Gibson LJ. A new technique for calculating individual dermal fibroblast contractile forces generated within collagen-GAG scaffolds. Biophys J. 2007;93:2911-22.
[136] Hidai H, Jeon H, Hwang DJ, Grigoropoulos CP. Self-standing aligned fiber scaffold fabrication by two photon photopolymerization. Biomed Microdevices. 2009;11:643-52.
[137] Doraiswamy A, Patz T, Narayan R, Chichkov B, Ovsianikov A, Houbertz R, et al. Biocompatibility of CAD/CAM ORMOCER polymer scaffold structures. Boston, MA, United States: Materials Research Society, Warrendale, PA 15086, United States; 2005. p. 51-6.
[138] Hutter JL, Bechhoefer J. Calibration of atomic-force microscope tips. Rev Sci Instrum. 1993;64:1868-73.
[139] Harley BA, Leung JH, Silva E, Gibson LJ. Mechanical characterization of collagen-glycosaminoglycan scaffolds. Acta Biomater. 2007;3:463-74.
[140] Dunn GA, Heath JP. New Hypothesis of Contact Guidance in Tissue-Cells. Experimental Cell Research. 1976;101:1-14.
[141] Rovensky YA, Samoilov VI. Morphogenetic Response of Cultured Normal and Transformed Fibroblasts, and Epitheliocytes, to a Cylindrical Substratum Surface - Possible Role for the Actin Filament Bundle Pattern. Journal of Cell Science. 1994;107:1255-63.
[142] Craig RR, Jr. Mechanics of materials: John Wiley & Sons, Inc.; 1996.
[143] Eastwood M, Porter R, Khan U, McGrouther G, Brown R. Quantitative analysis of collagen gel contractile forces generated by dermal fibroblasts and the relationship to cell morphology. J Cell Physiol. 1996;166:33-42.
[144] Ehrlich HP, Rajaratnam JBM. Cell locomotion forces versus cell contraction forces for collagen lattice contraction : an in vitro model of wound contraction. Tissue Cell. 1990;22:407-17.